Study of Spin Dynamics in Chiral & Two-dimensional Magnets

Safe-Ur-Rahman Khan

A dissertation submitted in partial fulfillment

of the requirements for the degree of

Doctor of Philosophy

of

University College London.

Department of Electronic and Electrical Engineering

University College London

May 20, 2020

I, Safe-Ur-Rahman Khan, confirm that the work presented in this thesis is my own. Where information has been derived from other sources, I confirm that this has been indicated in the work.

Abstract

This thesis explores the spin dynamics in three magnetic systems comprising of a chiral magnet and the bulk van der Waals (vdWs) layered magnets by mainly utilising the novel experimental technique of ferromagnetic resonance (FMR) spectroscopy. The non-centrosymmetric chiral ferrimagnet, Cu_2OSeO_3, has recently seen a great deal of interest from the spintronics community, as it has been shown to host various different magnetic spin textures and it was the first insulating system to show the presence of the skyrmion lattice. Over the last couple of years, the research field of layered vdWs materials has grown rapidly since the discovery of intrinsic magnetic order in the two-dimensional (2D) limit, i.e. down to the atomically thin monolayer limit, prohibited otherwise due to thermal fluctuations at low dimensionality.

In the first part of this thesis, the interaction of microwave cavity photons with magnons (a quanta of spin excitations in magnetically ordered systems) in different magnetic phases of Cu_2OSeO_3 is probed. A strong-coupling regime is realised in the field-polarised phase, creating a hybridised state of cavity-magnon-polariton. In the conical and helical phases, dispersive coupling and Purcell-effect regime is seen, respectively. In the skyrmion phase, an onset of anti-crossing feature is observed between photons and the counter-clockwise gyration mode, whereas high-order excitation mode are believed to be seen for the breathing resonance mode.

The spin dynamics of layered $Cr_2Ge_2Te_6$ bulk single crystal is investigated in the second study. The magnetisation dynamics experiment confirmed the presence of out-of-plane magnetic anisotropy, where the scaling of the uniaxial anisotropy constant and saturation magnetisation showed a deviation from the Callen-Callen

power law. The obtained spectroscopic g-factor exhibits anisotropic behaviour and a value higher than 2, suggesting the presence of orbital moment. The temperature dependence of the orbital moment is obtained via the X-ray magnetic circular dichroism (XMCD) experiment, which qualitatively compliments the results observed in the magnetic resonance experiments. Finally, the domain-mode resonance features are observed confirming the presence of multidomain structures in the system.

In the final study, sodium (Na) ions are intercalated in the vdWs gaps of $Cr_2Ge_2Te_6$ creating the $Na_{0.3}$-$Cr_2Ge_2Te_6$ samples. The intercalated samples show an enhancement in the ferromagnetic Curie temperature, where the FMR signal remains up to the temperature of 240 K. A change in the magnetic anisotropy is found compared to the unintercalated sample, and magnetic easy axis seems to lie along the in-plane orientation, whereas it is in the out-of-plane direction for $Cr_2Ge_2Te_6$.

Impact Statement

The results presented in this thesis contribute to the fundamental understanding of spin dynamics in a non-centrosymmetric chiral magnet and in layered van der Waals (vdWs) system, and hence advance the field of spintronics. In the case of the chiral magnet (Cu_2OSeO_3), strong light-matter coupling is realised for the field-polarised phase, and for the very first time, interaction of cavity photons with magnons in exotic spin-textures is probed, one of which is the topologically protected skyrmion state. The coherent coupling phenomena basically allows the energy to be efficiently exchanged between two excited states (in this case photons and magnons), and therefore, it has potential to be used in developing long-lifetime multimode quantum memories. The measurements performed in the skyrmion state have prompted the use of microwave resonators at low frequency (around 1 GHz) as the excitation modes of skymions lie at such low frequencies.

Since the discovery of presence of intrinsic magnetic order in layered vdWs systems, $Cr_2Ge_2Te_6$ and other materials in the family of two-dimensional magnets were mainly studied by magneto-optical and magneto-transport techniques. The spin dynamics study in $Cr_2Ge_2Te_6$ is among the first few reported work of such systems probed by the ferromagnetic resonance spectroscopy. Intercalation of atoms in layered transition metal dichalcogenides is a well-known concept in order to modify the properties of those systems. In this thesis, the effects of intercalation of alkali metal (Na) ions in the vdWs gaps of $Cr_2Ge_2Te_6$ are reported for the first time. This intercalation shows to enhance the ferromagnetic Curie temperature from 65 K (in $Cr_2Ge_2Te_6$) to 240 K in $Na_{0.3}$-$Cr_2Ge_2Te_6$ system. These layered magnets are expected to play a pivotal role in spintronics and more broadly in condensed matter

physics field, and hence, having presence of magnetic order at room-temperature can help the chances of their integration into new spintronic devices.

Acknowledgements

بِسْمِ ٱللَّهِ ٱلرَّحْمَٰنِ ٱلرَّحِيمِ

(In the name of Allah (God), the Most Gracious, the Most Merciful)

Alhamdulillah, I thank God for all the blessings, and giving me the opportunity to carry out the work presented here.

I would sincerely like to thank my supervisor Dr Hidekazu Kurebayashi for all his help. The constant encouragement and support over the past four years has made this an enjoyable and worthwhile experience. All his invaluable advice in terms of research and, in general, has been of exceptional help. He has proved to be a great mentor. His guidance and supervision has been essential during this work.

I would also like to take this opportunity to thank Professor Robert J Hicken and Professor Steven Bramwell - my viva examiners, for their very helpful comments and suggestions. Thank you for letting my viva be an enjoyable moment in the virtual environment.

There is a big list of people without whom this work would not have been possible. Starting from the very first day of PhD, I would like to thank Tim, Kostas, Kazu, Leonid, Christoph, Daan and Kashim (a special mention for making the intercalated samples) for training me and guiding me in the lab. I would also like to thank all the group members especially Aakanksha and Oscar for assisting me during the experiments. I am grateful to John Langdon (EEE workshop) for making all the varied range of sample holders for my experiments on a short notice.

I thank the external collaborators, Dr Seki (University of Tokyo) and Ivan (National University of Singapore) for providing the samples used in thesis. I am grateful to Jon Breeze (Imperial) for helping me with designing the skyrmion experiment

and consequently with the analysis, and I am glad that I can call him a friend now. Another person to mention here is Larissa, who helped with acquiring the in-house beam time at Diamond Light Source facility and supported me with the analysis of XMCD data.

Now, a big thanks to my all friends. First and foremost, Dr Daniel Gradeci, who has always encouraged me to do well and has been a big support throughout the PhD, and for some reason keeps calling me naive all the time. The short lunch, coffee and chess breaks with Daniel and Laurie were very important for surviving and staying sane during the Phd. I am grateful to Laurie for his help in making the small magnet. Also, I would also like to thank other members of the LCN crew: Maeve, Maxi, Troy and Jonathan. A special mention goes to Hakim for all the footy and other enlightened chats being the first thing in the morning upon entering LCN.

Finally, I would like to thank my parents for all their love and inspiration throughout my life, and for their constant prayers and support. This work would not have been possible without the family support system at home, and for that I appreciate and thank my parents, my nan and my siblings. Lastly, a mention to the four little ninjas (Aayma, Hamza, Asbah and Abeeha) in the house who keep it buzzing most of the time.

Contents

List of Figures

List of Tables

List of Abbreviations

2D	Two-dimensional
AMR	Anisotropic Magnetoresistance
CCW	Counter-Clockwise
CGT	$Cr_2Ge_2Te_6$
CMP	Cavity-Magnon-Polariton
CPW	Co-planar Waveguide
DFT	Density Functional Theory
FMR	Ferromagnetic Resonance
IP	In-plane
LLG	Landua-Lifshitz and Gilbert
MCA	Magneto-crystalline Anisotropy
MR	Magnetoresistance
OOP	Out-of-plane
RWA	Rotating Wave Approximation
SO	Spin-Orbit
STO	Strontium Titanate
SQUID	Superconducting Quantum Interference Device
XANES	X-ray Absorption Near-Edge Spectroscopy
XAS	X-ray Absorption Spectroscopy
XMCD	X-ray Magnetic Circular Dichroism
vdW	van der Waals
VNA	Vector Network Analyser
YIG	Yttrium Iron Garnet

Chapter 1

Introduction

Spintronics, i.e. the use of the spin degree of freedom of electrons to create new electronic devices and functionalities [1], has evolved to one of the most pursued research fields in condensed matter physics. The nature of spintronic devices is based on a spin control of electronics or an electrical and optical control of spins, and hence, it is described as an emerging research field of electronics. Spin transport electronics, or spintronics, can nowadays be found in many electronic devices. In particular, spintronics has found its way in data storage and manipulation devices such as the read/write of a hard-disk, magneto-resistive random-access memory (M-RAM) and spin-transfer torque random-access memory (STT-RAM) [2, 3]. The wish to increase the speed and storage capacity, and to decrease the power consumption has lead to constant discoveries of new spintronic phenomena like the spin transfer torque [4], spin-orbit torques [5] ('Spin-Orbitronics'), the spin Hall effect [6], the spin Seeback effect [7] and plasmonic spintronics [8].

Nowadays, the research drive to combine the fields of quantum information and spintronic technologies is quite evident. On the quantum information front, the light-matter interactions offer a strong avenue to access and control quantum states, and in parallel, new insights into manipulation of spin-photon system benefits the development of spintronic technologies [9]. Achieving a hybridised state between excitations in a ferromagnet and cavity photons has pushed the era of light-matter exploration closer to bringing fruitful results in combining the fields of quantum information and spintronics, i.e. 'cavity spintronics' [10]. The foundation of cavity

spintronics is based on a quasi-particle; the cavity-magnon-polariton (CMP). This quasi-particle is observed when the spin-wave excitations of the ferromagnet, i.e. magnons, and cavity photons enter into a strong coupling regime, such that the energy (information) is exchanged between the magnon and photon systems before it is lost to damping. The large number of spins in ferromagnetic materials make them ideal systems to study the coherent coupling as the coupling strength between a photon and an ensemble of N-particles scales with the square-root of N, as $g_N = g_0\sqrt{N}$ [11]. So far, the majority of the work for investigating the coupling of magnons and photons has mainly utilised the ferrimagnetic yttrium iron garnet (YIG) sample [11] only possessing a field-polarised phase due to the isotropic $(\mathbf{S}_i \cdot \mathbf{S}_j)-$like Heisenberg exchange interaction between the neighbouring spin, $\mathbf{S}_i$ and $\mathbf{S}_j$.

In solids, it is believed that the net effect of spinorbit coupling is related to the breaking of crystal inversion symmetry, where in the case of the zinc-blende structure there exists a bulk inversion asymmetry (BIA) which results in Dresselhaus spin-orbit coupling and the structural inversion asymmetry (SIA) results in the Rashba spin-orbit coupling due to deformation or an asymmetric electric potential [12]. In chiral magnets, the lack of the inversion symmetry introduces the relativistic spin-orbit ($\mathbf{S}_i \times \mathbf{S}_j-$like) Dzyalonshinskii-Moriya Interaction (DMI). DMI, antisymmetric in nature, competes with the collinear exchange interaction and stabilises the system into non-collinear spin textures [13]. These non-collinear spin textures include helical and conical (spiral spin structures) phases, and a topologically protected 'vortex-like' skyrmion spin structures also exists just below the magnetic phase transition (in a narrow temperature window below the Curie temperature) [14].

Another emerging field of research is the two-dimensional (2D) crystals, where the family of these materials has been growing at a rapid pace since the discovery of graphene nano-sheets [15]. The reason behind the interest in 2D materials is that more often than not, a mono-layer of these crystals possess properties which are significantly different from their three-dimensional (3D) parent compound, one such example is that graphene is a zero-gap semi-conductor, whereas graphite is a semi-

metal [16]. Only until recently, this family was missing one important member, i.e. layered van der Waals (vdWs) 2D-magnets, materials having intrinsic magnetic order in the 2D-limit. The long-range magnetic order in the 2D limit at finite temperatures is prohibited due to the thermal fluctuations destroying the magnetic order according to the Mermin-Wagner theorem, but the presence of magnetic anisotropy counter-acts the thermal fluctuations and allows the system to have a magnetic order [16]. The few prominent 2D-magnets are $Cr_2Ge_2Te_6$, CrI_3 and Fe_3GeTe_2, where most of these systems have been extensively studied by magneto-optical and magneto-transport techniques [17]. One slight draw-back of these 2D-magnets is that the Curie temperature (T_c) for the magnetic order lies towards the low temperature region, where cryogenic facilities are required to probe their properties [17]. But, recent studies of gate-tunable room temperature ferromagnetism in layered 2D Fe_3GeTe_2 [18], significant enhancement of T_c in gated-$Cr_2Ge_2Te_6$ sample [19] and the discovery of near room temperature ferromagnetism in the cleavable Fe_5GeTe_2 [20] have highlighted the significance that these layered vdWs systems can have for spintronics devices with room temperature applications.

In 1946, J. H. E. Griffiths and E. K. Zavoiskii independently reported on anomalous Larmor frequencies [21, 22], observed in magnetic spectroscopy experiments in the microwave frequency range, a novel experimental method was born, today known as ferromagnetic resonance (FMR). This spectroscopy technique allows a variety of investigations on ferromagnetic materials, such as probing the spin dynamics, magnetic anisotropies, spectroscopic g-factor, magnetoelastic and relaxation processes [23].

In this study, mainly utilising the technique of spin dynamics (FMR) spectroscopy, investigation of the interaction of spin excitations (in different magnetic phases) and cavity photons is carried out in a chiral magnet (Cu_2OSeO_3). Magnetisation dynamics of a layered vdWs bulk magnet ($Cr_2Ge_2Te_6$) are presented. Finally, the bulk $Cr_2Ge_2Te_6$ is doped via the chemical intercalation of sodium (Na)-atoms in the vdWs gap ($Na_{0.3}$-$Cr_2Ge_2Te_6$), and an enhancement of the ferromagnetic (T_c) ordering temperature is observed.

Thesis Outline

A brief overview of physics topics explored in this thesis and the mathematical analysis performed for the experimental chapters later is given in chapter 2. Chapter 3 highlights the experimental techniques used to obtain the experimental data in this thesis.

In chapter 4, the experimental results of cavity photons interaction with magnons in different magnetic phases of the chiral magnet, Cu_2OSeO_3 , are presented. Strong coupling between the photons and magnons in the field-polarised phase is achieved. In the non-collinear helical phase a Purcell-effect regime is detected between photons and high-order helimagnons. In the conical phase, dispersive coupling feature is seen which is used to map-out the magnetic phase diagram. In the skyrmion phase, an onset of anti-crossing feature is seen between photons and the Counter-Clockwise resonance mode, and high-order excitation modes are thought to be observed for the breathing resonance mode.

The spin dynamics study of the bulk single crystal of $Cr_2Ge_2Te_6$ is discussed in chapter 5 probed by the FMR technique. A uniaxial magnetic anisotropy is found with magnetic easy axis along the out-of-plane orientation. The scaling of the normalised magneto-crystalline anisotropy constant and saturation magnetisation shows a deviation from the theoretically predicted Callen-Callen power law. The spectroscopic g-factor is obtained which shows an anisotropic response, i.e. crystallographic dependence, as a function of temperature, $g-$values of higher than 2 are observed suggesting the presence of orbital moment. This is further investigated by the X-ray magnetic circular dichroism (XMCD) technique, and a sizeable anisotropic orbital moment is found. The domain-mode resonance features are observed in the FMR spectra along the in-plane orientation qualitatively confirming presence of multi-domain structures in the system.

In chapter 6, the experimental results of the enhancement of ferromagnetic transition temperature and the change in magnetic anisotropy are presented for the case of alkali metal ($Na_{0.3}$) ions intercalated CGT ($Na_{0.3}-$CGT). The magnetic properties are probed by the magneto-transport and FMR spectroscopy techniques.

The sample investigated by the magneto-transport measurement shows a magnetoresistance (MR) signal up to 195 K, whereas the sample used for the FMR experiment reveals a FMR signal up to the temperature of 240 K. In both the transport and magnetic resonance measurements, the magnetic anisotropy is found to be changed compared with unintercalated CGT sample, and the magnetic easy-axis is found to lie along the in-plane (ab-plane) orientation whereas it is along the out-of-plane (c-axis) orientation in the case of CGT.

Chapter 2

Theoretical Background

This chapter highlights the main topics of physics explored in this thesis for the reader and also the mathematical equations are presented which are used in the later experimental chapters (i.e. chapters 4, 5, and 6) for the analysis.

2.1 Ferromagnetism

The phenomenon in which specific solids present a spontaneous magnetisation with parallel alignment of spins, even in the absence of an external magnetic field, is referred to as ferromagnetism. The behaviour of the coupling of magnetic moments with each other, leading to reciprocal parallel alignment, is commonly referred to as collective magnetism. The appearance of ferromagnetic order happens only below a critical temperature, the Curie temperature, which is characteristic for a given material, and the material attains paramagnetic state above the Curie temperature [24].

The magnetisation, or saturation magnetisation **M**, in a solid of volume V is given by:

$$\mathbf{M} = \frac{1}{V}\int_{V} \boldsymbol{\mu} dV \quad , \quad M_s = |\mathbf{M}| \tag{2.1}$$

where $\boldsymbol{\mu}$ is the total magnetic moment of each electron. $\boldsymbol{\mu}$ is directly related to the total angular momentum **J** by:

$$\boldsymbol{\mu} = -g\frac{\mu_B}{\hbar}\mathbf{J} \tag{2.2}$$

where g is the Landé - factor and $\mu_B = e\hbar/(2m_e)$ is the Bohr magneton (with elementary charge e, reduced Planck constant $\hbar$, electron mass m_e) [25].

Ferromagnetic order originates due to the short-range quantum mechanical exchange interaction following from the Pauli exclusion principle for fermions [26]. In addition, there is also a long-range (weak) interaction arising due to the dipolar field of each magnetic moment, which does not provide a decisive contribution to collective magnetism, but is the origin of shape anisotropy, important for consideration when characterising magnetic materials.

Another kind of magnetism, important to highlight for this thesis, is the ferrimagnetism. A material which microscopically is antiferromagnetic like, but in which the magnetisations (spins) of the two sublattices are not the same in magnitude characterises as a ferrimagnet [27]. The two sublattices no more compensate each other as in the case of an antiferromagnet, hence, a spontaneous magnetisation appears below the ordering temperature T_c in a ferrimagnet, where the macroscopic properties in this temperature range are close to that of a ferromagnet [28].

2.2 Magnetic Interaction Energies

The following section provides an introduction to the main interaction energies in a magnetic system, which has different contributions, namely exchange energy (E_ex), Zeeman energy (E_Zeeman), dipolar energy (E_dip), and magnetocrystalline anisotropy energy (E_Anis):

$$E = E_\mathrm{ex} + E_\mathrm{Zeeman} + E_\mathrm{dip} + E_\mathrm{Anis} \tag{2.3}$$

Exchange Energy

The exchange interaction, fundamental force responsible for the long range magnetic ordering, is a quantum mechanical effect determined by the Pauli exclusion principle and the electrostatic Coulomb interaction. The exchange energy, in the

Heisenberg Hamiltonian form, is given by [29]:

$$E_{\text{ex}} = \frac{1}{2}\sum_{i<j} J_{ij}\mathbf{S}_i \cdot \mathbf{S}_j \tag{2.4}$$

J_{ij} is the exchange integral, which represents the energy difference between singlet (anti-parallel) and triplet (parallel) states for the nearest neighbour spins $\mathbf{S}_i$ and $\mathbf{S}_j$. A positive exchange integral, $J_{ij} > 0$, favours parallel alignment of neighbouring spins, resulting in ferromagnetic order. Antiferromagnetic ordering, on the other hand, has a negative exchange integral, favouring anti-parallel alignment of spins. The exchange energy given by the above equation is isotropic, resulting in no preferential orientation of the magnetisation with respect to the crystal axis.

The exchange integral, shown by Eq. 2.4, gives rise to the direct exchange interaction between electrons from two-neighbouring spins. The Heitler-London model of the hydrogen molecule [24] is often used to describe the concept of direct exchange interaction. In brief, the two hydrogen electrons exist in states which are represented by the spatial coordinates and spin states in this model. The product of the spatial wavefunctions and spin wavefunctions of the individual electrons make up the total eigenfunction of the two-electron system. The total wavefunction should be anti-symmetric with respect to exchange in order to satisfy the Pauli exclusion principle [29], so a sign reversal of the wavefunction must take place upon the exchange of the electrons. This can be achieved in two ways: where either the spatial part is symmetric and spin part is antisymmetric (*singlet state*) or the spatial part in antisymmetric and the spin part is symmetric (*triplet state*). J_{ij} is negative in the case of H_2 molecule, and hence there is no net magnetic moment as the spins are anti-parallel.

Other type of exchange interactions also exist in magnetic materials. An indirect exchange interaction between magnetic ions in metals can be mediated by the conduction electrons [30]. This exchange interaction is identified as indirect because a localised moment spin-polarises the conduction electrons, which in turn couple to a neighbouring localised magnetic moment at a distance r away. Therefore, the exchange interaction is indirect as it does not involve direct coupling be-

tween magnetic moments, and it is known as RKKY (Ruderman-Kittel-Kasuya-Yosida) interaction. Another type of indirect exchange interaction is found in ionic solids, for example oxides, known as the super-exchange interaction [31]. It is an indirect exchange interaction as a non-magnetic ion placed between the non-neighbouring magnetic ions mediates this coupling.

There is also another important exchange interaction, anti-symmetric exchange interaction, known as the Dzyaloshinskii-Moriya (DM) interaction [32]. The DM interaction makes a contribution to the total exchange interaction in certain magnetic materials between two neighbouring spins represented by $\mathbf{S}_i$ and $\mathbf{S}_j$, and it is represented by a vector $\mathbf{D}_{ij}$ and the Hamiltonian is proportional to the product of the two spins given by [32]:

$$\mathbf{H}_{\mathrm{DM}} = \mathbf{D}_{ij} \cdot (\mathbf{S}_i \times \mathbf{S}_j). \tag{2.5}$$

The DM interaction is found in crystals which lack the inversion symmetry (for example the B20 chiral magnets). The effect of the DM interaction is that it competes with the ferromagnetic Heisenberg exchange interaction which produces parallel alignment of spins, causing a coherent canting of spins, and hence introducing chirality in magnetic configuration [33].

Zeeman Energy

The Zeeman energy is the interaction between the magnetisation, $\mathbf{M}$, in a magnetic system and any external magnetic field, $\mathbf{H}_{\mathrm{ext}}$, and it exerts a torque on the magnetic moment which minimises the energy when aligned parallel to the applied field. The Zeeman energy is defined by:

$$E_{\mathrm{Zeeman}} = -\mu_0 \mathbf{M} \cdot \mathbf{H}_{\mathrm{ext}} \tag{2.6}$$

where μ_0 is the vacuum permeability. An external magnetic field makes it possible to manipulate the magnetic state through the Zeeman interaction. This allows for an external switching mechanism, which is of great importance for applications in magnetic storage devices [34].

Demagnetisation Energy

The long-range magnetic dipole interaction is the origin of the shape anisotropy. Magnetic poles appear on the surface of a uniformly magnetised sample giving rise to a demagnetising field, H_d.The corresponding energy is given as [35]:

$$E_{\text{dip}} = -\frac{1}{2}\mu_0 \int_V \mathbf{M}(\mathbf{r}) \cdot \mathbf{H}_d(\mathbf{r}) d\mathbf{r} \tag{2.7}$$

The order of magnitude of the dipole-dipole interaction is very small compared to the exchange energy discussed above, however, due to its long-rang nature, it is of great importance for domain structure and shape anisotropy. The magnetic moments, in many cases (e.g. in cubic crystals), are compensated inside a solid due to the domain formation and do not contribute to the dipolar energy, but uncompensated moments at the sample surface do exist and they generate a dipolar field. This dipolar field is referred to as the stray field outside and demagnetising field inside the sample. In a homogeneously magnetised ellipsoid the demagnetisation field can be written in the following form [36]:

$$\mathbf{H}_{\text{d}} = -\bar{\bar{\mathbf{N}}}\mathbf{M} \tag{2.8}$$

where $\bar{\bar{\mathbf{N}}}$ is the demagnetising tensor, a tensor of the second order and whose trace equals 1. This tensor is diagonal in the principal axes system of the ellipsoid:

$$\bar{\bar{\mathbf{N}}} = \begin{bmatrix} N_{xx} & 0 & 0 \\ 0 & N_{yy} & 0 \\ 0 & 0 & N_{zz} \end{bmatrix}, \qquad N_{xx} + N_{yy} + N_{zz} = 1. \tag{2.9}$$

The following table shows the diagonal tensor elements for the case of sphere, cylinder and film in (x,y)-plane.

	N_{xx}	N_{yy}	N_{zz}
Sphere	1/3	1/3	1/3
Cylinder —— $\mathbf{e}_z$	1/2	1/2	0
Film in (x,y)-plane	0	0	1

Table 2.1: Diagonal elements of the demagnetising tensor for different geometries in principal axis coordinate system [36].

2.3 Magnetocrystalline Anisotropy Energy

The magnetocrystalline anisotropy (MCA), caused by the spin-orbit interaction, is an intrinsic property of a magnetic material which is defined by its crystalline structure. The spin-orbit interaction, in a semiclassical picture, couples the spin, **S**, and orbital, **L**, angular momentum by [37]:

$$E_{SO} = \xi(r)\mathbf{S}\cdot\mathbf{L} \tag{2.10}$$

where $\xi(r)$ is the spin-orbit (SO) coupling constant. The overlap of the atomic wave functions is anisotropic in a crystalline magnetic metal due to the strong localisation of the d-electrons, since it depends on the crystallographic direction. A rotation of the spins causes a change in the overlap of the orbitals, due to the SO interaction, which leads to an increase of the total energy, meaning that the SO energy is crystallographic directions dependent and, hence, the symmetry of the MCA follows the symmetry of the electronic structure and, thus the symmetry of the crystal lattice. In a phenomenological model, the MCA is described by the expansion of the free energy density, g_{MCA}, into a series of the component α_i of the unit vector pointing into the direction of the magnetisation [38]:

$$g_{MCA} = \sum_i b_i\alpha_i + \sum_{i,j} b_{ij}\alpha_i\alpha_j + \sum_{i,j,k} b_{ijk}\alpha_i\alpha_j\alpha_k + \ldots \ . \tag{2.11}$$

The magnetocrystalline energy, for cubic crystals, can be expressed in terms of the direction cosines $(\alpha_x, \alpha_y, \alpha_z)$ of the magnetisation vector with respect to the edges of the crystal cube. The MCA is invariant under inversion of the magnetisation, $g_{MCA}(\mathbf{M}) = g_{MCA}(-\mathbf{M})$, and hence, the magnetocrystalline energy of a cubic crystal is given as:

$$g_{MCA}^{(cub)} = K_{c1}(\alpha_x^2\alpha_y^2 + \alpha_y^2\alpha_z^2 + \alpha_x^2\alpha_z^2) + K_{c2}(\alpha_x^2\alpha_y^2\alpha_z^2) + ... \tag{2.12}$$

where K_{c1} and K_{c2} are the cubic anisotropy constants which depend on the given material and are determined experimentally. The anisotropy constants do not have any direct physical meaning, but the strengths and signs give information about the crystallographic direction for which the anisotropy energy is minimal.

The magnetocrystalline anisotropy for hexagonal and tetragonal crystals, which show a uniaxial anisotropy is expressed as [38]:

$$g_{MCA}^{(uni)} = K_{u1}(\sin^2\theta) + K_{u2}(\sin^4\theta) \tag{2.13}$$

θ is the angle between the magnetisation direction and the anisotropy axis, and here, a large positive K_{u1} describes an easy axis and, in general, K_{u2} is small in comparison to K_{u1}. The energy difference between magnetic easy and hard axis is very small as compared to the isotropic, direct exchange interaction and ranges between μeV and meV (exchange interaction 0.01 - 0.1 eV). The description of the magneto-elastic anisotropy, similar to that of the MCA, originates from the distortion of ferromagnetic material. The inversion of this effect, where changing the direction of magnetisation causes the deformation of the material, is called magnetostriction [39].

2.4 Magnetisation Dynamics

2.4.1 Landau-Lifshitz and Gilbert Equation

The Landau-Lifshitz and Gilbert equation describes the behaviour of the magnetisation in an external field, which is the equation of motion in magnetisation dynamics and describes the precessional motion of a magnetic moment $\boldsymbol{\mu}$ around an effective field $\mathbf{H}_{\text{eff}}$ [40].

A magnetic moment $\boldsymbol{\mu}$ in an effective field $\mathbf{H}_{\text{eff}}$, following the semi-classical treatment, will be exposed to a torque:

$$\boldsymbol{\tau} = \mu_0(\boldsymbol{\mu} \times \mathbf{H}_{\text{eff}}) \ . \tag{2.14}$$

The angular momentum $\mathbf{J}$ and $\boldsymbol{\mu}$ are connected via the relation:

$$\boldsymbol{\mu} = -\frac{g\mu_B}{\hbar}\mathbf{J} = -\gamma\mathbf{J} \tag{2.15}$$

where $\gamma = g\mu_B/\hbar$ is the gyromagnetic ratio. The torque is defined as the rate of change of angular momentum from Newton's classical equation $\boldsymbol{\tau} = d\mathbf{J}/dt$, and hence, Eq. 2.15 can be expressed as:

$$\frac{d\mathbf{J}}{dt} = -\frac{1}{\gamma}\frac{d\boldsymbol{\mu}}{dt} = \mu_0(\boldsymbol{\mu} \times \mathbf{H}_{\text{eff}}) \ . \tag{2.16}$$

In terms of the macroscopic magnetisation $\mathbf{M} = \boldsymbol{\mu}/V$, where V is the total volume, the equation above results in the Landau-Lifshitz equation (LL equation) [41]:

$$\frac{d\mathbf{M}}{dt} = -\gamma\mu_0(\mathbf{M} \times \mathbf{H}_{\text{eff}}) \ , \tag{2.17}$$

which describes the precession of $\mathbf{M}$ around the axis defined by the effective field $\mathbf{H}_{\text{eff}}$ (Fig. 2.1 (a)).

The LL equation does not account for damping in the system, and therefore, the equation describes an unphysical condition where the magnetisation would precess infinitely long once its direction deviates from the equilibrium direction. As like many other physical systems, in reality, the precession is damped. In general, the intrinsic magnetic damping is mainly caused by the transfer of energy and (angular) momentum from the spin system to the phonon system via the spin-orbit coupling or within the spin system by the excitation of spin waves [42], as well as by electron scattering [43].

A way to consider the damping for the equation of motion was suggested by Gilbert [40] by adding a phenomenological torque (an Ohm-like dissipation term, depending on the time evolution of the magnetisation) to the LL equation, which has a vector component along the radial direction of the precession, and hence, this

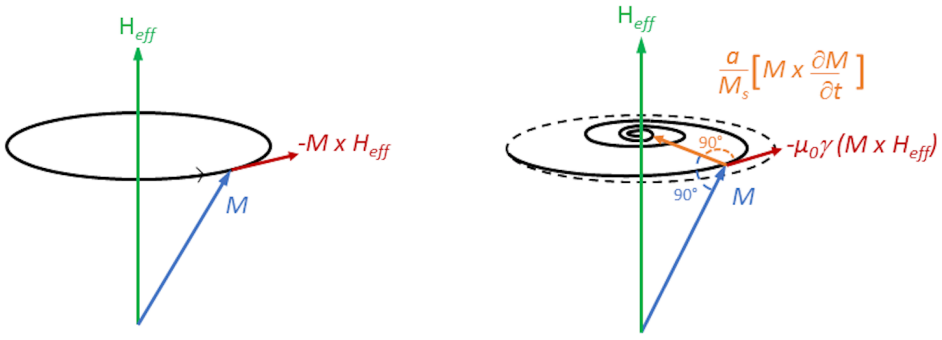

(a) **(b)**

Figure 2.1: Schematic of magnetisation dynamics. (**a**) The magnetisation vector **M** (blue) precesses counter-clockwise around the effective field $\mathbf{H}_{\text{eff}}$ (green) following the LL equation (i.e. no damping in the system, black trace, described by Eq. 2.17). (**b**), Adding the phenomenological damping term (orange vector), described in the LLG equation (Eq. 2.18), causes the magnetic motion to relax towards the direction of $\mathbf{H}_{\text{eff}}$.

damping torque drags the magnetisation into the direction of the equilibrium direction. Therefore, the Landau-Lifshitz and Gilbert equation (LLG equation) gives a more realistic equation of motion, expressed as:

$$\frac{d\mathbf{M}}{dt} = -\gamma\mu_0(\mathbf{M}\times\mathbf{H}_{\text{eff}}) + \frac{\alpha}{M_S}(\mathbf{M}\times\frac{d\mathbf{M}}{dt}) \ , \tag{2.18}$$

where α is the dimensionless Gilbert damping parameter, (in principle) a material parameter of magnetic solids, which is a measure of the overall different viscous physical processes. The first term on the right-hand side of the above equation describes the Larmor-precession of the magnetisation in an effective magnetic field, while the second term represents the damping and produces gradual alignment of the magnetisation in the direction of the magnetic field. In Fig. 2.1 (b), the realistic, damped precessional movement of the magnetisation around the axis defined by the effective magnetic field, and the interplay between the different torque terms are illustrated.

In the LLG equation, the effective field, $\mathbf{H}_{\text{eff}}$, is the sum of all internal fields, some of which are discussed above in the Eq. (2.3), as well as the static and dynamic external fields.

$$\mathbf{H}_{\text{eff}} = \mathbf{H}_{\text{ex}} + \mathbf{H}_{\text{Anis}} + \mathbf{H}_{\text{demag}} + \mathbf{H}_{\text{ext}} + \mathbf{h}_{\text{rf}}(t) + \ldots \ , \tag{2.19}$$

where $\mathbf{H}_{\text{ex}}$ and $\mathbf{H}_{Anis}$ are the exchange field and the anisotropy field, and $\mathbf{H}_{\text{demag}}$ denotes the demagnetising field. Two important components are the externally applied static field $\mathbf{H}_{\text{ext}}$ and the dynamic external field $\mathbf{h}_{\text{rf}}(t)$. Further field-like contribution can be included as well, depending on the system under study.

2.4.2 Ferromagnetic Resonance

The application of an external time dependent field ($\mathbf{h}_{\text{rf}}$ in Eq. 2.19) with frequency ω can compensate the damping of the magnetisation in a magnetic system. The precession angle between the magnetisation $\mathbf{M}$ and $\mathbf{H}_{\text{eff}}$ is kept constant by the oscillation of this dynamic field in a plane perpendicular to the effective field. In resonance, this leads to uniform precession of the magnetisation i.e. all the spins precess in phase, which is referred to as ferromagnetic resonance (FMR) [44, 45].

The static and dynamic properties of a magnetic system can be obtained from the FMR spectra. The resonance field in the spectra can provide information about the magnetic properties such as the g-factor, saturation magnetisation and magnetic anisotropies in the system, and from the FMR linewidth, the magnetic inhomogeneity and the damping parameter for the magnetisation precession can be obtained.

The total magnetic moment can be considered as one macrospin $\mathbf{M}$ in a ferromagnet, which precesses around the local static field $\mathbf{H}$ at the Larmor frequency $\omega_L = \gamma\mathbf{H}$. The macrospin $\mathbf{M}$ behaves in the same way as the single ion in static magnetic field, when irridiated with a rf magnetic field, but the FMR condition is given by the Smit-Beljars-Suhl equation [46, 47]:

$$\left(\frac{\omega}{\gamma}\right)^2 = \frac{1}{M_s \sin(\theta_M)}\left[\frac{\partial^2 F}{\partial \theta_M^2}\frac{\partial^2 F}{\partial \phi_M^2} - \left(\frac{\partial^2 F}{\partial \theta_M \partial \phi_M}\right)\right] \tag{2.20}$$

where the angles $\theta_{H/M}$ and $\phi_{H/M}$ are the polar and azimuthal angles of $\mathbf{H}$ and $\mathbf{M}$ with respect to the z- and x-axis, respectively, the coordinate system can be seen in Fig 2.2. The total energy per unit volume of the magnetisation, F, for the case of a thin film is given by (excluding exchange energy):

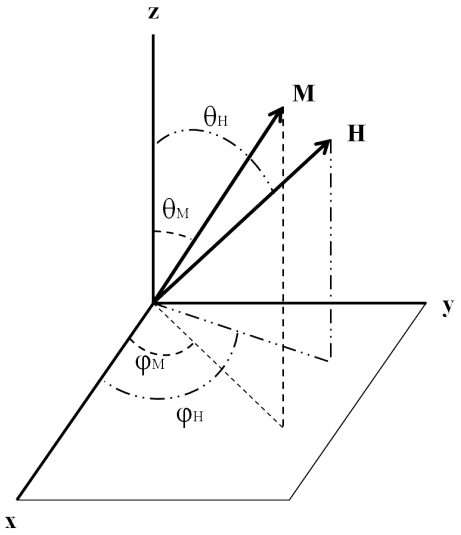

Figure 2.2: The coordinate system for a thin film which lies in the xy-plane and the magnetisation **M** of the film points in the **M**-direction. The applied DC magnetic field points in the **H**-direction.

$$F = -\mu_0 \mathbf{M}.\mathbf{H} + \mu_0(\mathbf{M}.\mathbf{n})^2 - K(\mathbf{M}.\frac{\mathbf{u}}{M_s})^2. \tag{2.21}$$

The first term in the equation above is the Zeeman energy, the second term is the demagnetisation energy and the third term is the uniaxial anisotropy term, with K, the magnetic anisotropy constant, M_s, the saturation magnetisation, and n and u are the unit vectors normal to the surface of the sample and orientated along the easy axis of the sample, respectively. **H** and **M** can then be written as

$$\mathbf{H} = H[\sin(\theta_H)\cos(\phi_H), \sin(\theta_H)\sin(\phi_H), \cos(\theta_H)] \tag{2.22}$$

$$\mathbf{M} = M_s[\sin(\theta_M)\cos(\phi_M), \sin(\theta_M)\sin(\phi_M), \cos(\theta_M)]. \tag{2.23}$$

Substituting the expression for F (Eq. 2.21) into Eq. 2.20 and solving for the perpendicular anisotropy case ($\mathbf{n} = \mathbf{u} = [001]$, i.e. easy axis out of plane of the thin film and along the z-axis), the FMR condition then becomes

$$\begin{aligned}\left(\frac{\omega}{\gamma}\right)^2 &= [H_\mathrm{r}\cos(\theta_\mathrm{H} - \theta_\mathrm{M}) - 4\pi M_\mathrm{eff}\cos^2(\theta_\mathrm{M})] \\ &\quad \times [H_\mathrm{r}\cos(\theta_\mathrm{H} - \theta_\mathrm{M}) - 4\pi M_\mathrm{eff}\cos(2\theta_\mathrm{M})]\end{aligned} \tag{2.24}$$

where $4\pi M_{eff} = 4\pi M_s - H_\perp$ is the effective demagnetisation field and $H_\perp = 2K/M_s$ the perpendicular anisotropy field. On resonance, the values for θ_M and ϕ_M can be determined by the condition $\partial F/\partial\theta_M = 0$ and $\partial F/\partial\phi_M = 0$; θ_M on resonance is then given by

$$\sin(2\theta_M) = \frac{2H_r}{4\pi M_s - H_\perp}\sin(\theta_M - \theta_H) \tag{2.25}$$

The resonance condition for the in-plane and out-of-plane configurations can then be determined by setting $\theta_M = \theta_H$, and the following expressions come out for the two cases:

$$\omega = \gamma(H_r - 4\pi M_{eff}) \qquad \text{out-of-plane} \tag{2.26}$$

$$\omega = \gamma\sqrt{H_r(H_r + 4\pi M_{eff})} \qquad \text{in-plane} \tag{2.27}$$

The measured linewidth ΔH from the resonance absorption peak in the FMR spectra consist of two contributions, an extrinsic contribution $\Delta H(0)$ and an intrinsic contribution, where the intrinsic contribution is proportional to the damping parameter α [48], and it is given by

$$\Delta H = \frac{4\pi\alpha f}{\gamma} + \Delta H(0) \tag{2.28}$$

The linewidth is linearly dependent on the excitation frequency and the slope from the linear fit of the above equation gives value of α, where the linewidth is defined as the full-width-half-maximum (FWHM) of the FMR absorption peak. The extrinsic contribution to the linewidth is a result of inhomogeneities, like impurities or defects in the crystalline structure.

The line-shape of the ferromagnetic resonance peak can be derived from the magnetic susceptibility, χ, and the full derivation can be seen elsewhere in Ref. [49]. The real and imaginary parts of the susceptibility as a function of the externally applied magnetic field read as [49, 50]

$$\mathrm{Re}[\chi] = \chi' = A\frac{H_0 - H_r}{(H_r - H_0)^2 + (\frac{\Delta H}{2})^2}, \tag{2.29}$$

$$\mathrm{Im}[\chi] = \chi'' = A\frac{(\frac{\Delta H}{2})}{(H_r - H_0)^2 + (\frac{\Delta H}{2})^2}. \tag{2.30}$$

where A is an amplitude pre-factor. The real part (χ') describes the dispersion and the imaginary part (χ'') describes the absorption of FMR, and the two equations mathematically represent the anti-symmetric and symmetric Lorentzian functions, respectively. Hence, the FMR spectra can be fitted with a Lorentzian function in order to the obtain the resonance position (peak-position) and the linewidth.

2.5 Cavity Photons − Magnons Interaction

The interaction of photons in a cavity with the spin-wave excitations, i.e. magnons, of a ferromagnet can be intuitively understood from that of a hybridised system consisting of two-resonant harmonic oscillators [51]. The hybridised state of cavity photons and magnons is referred to as the 'cavity-magnon-polariton' (CMP) [51]. Reviewing the quantum approach in combination with the input-output formalism, the Hamiltonian ($H = H_{photon} + H_{spin} + H_{coupling}$) describing the interaction is given by the Jaynes-Cummings model [52] for an ensemble of N_s spins coupled to a single mode of a resonant cavity, ω_c. Considering the lowest excitation FMR (uniform) mode, ω_m, the Hamiltonian of the spin-photon interaction can be written as

$$H = \hbar\omega_c a^\dagger a + \hbar\omega_r b^\dagger b + \hbar g(a + a^\dagger)(m + m^\dagger), \tag{2.31}$$

where $a^\dagger(a)$ and $m^\dagger(m)$ are the creation (annihilation) operators for the photon and magnon, respectively, and g is the coupling strength. The above Hamiltonian can be simplified in the rotating-wave approximation (RWA) as

$$H = \hbar\omega_c a^\dagger a + \hbar\omega_r m^\dagger m + \hbar g(am^\dagger + a^\dagger m), \tag{2.32}$$

where this Hamiltonian governs the basic physics of the hybridised system of CMP. In order to experimentally realise a hybridised system of photons and

magnons, utilising the above described Jaynes-Cummings Hamiltonian, the cavity photons must be coupled to the microwave feed-lines from a source to the cavity. This is summarised by the input-output formalism with great detail in the literature [52, 53] for a two-port system (Fig. 2.3).

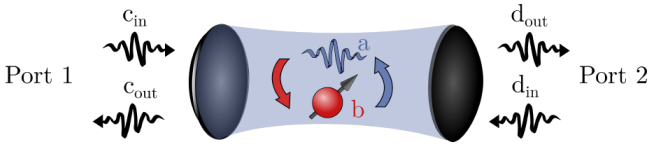

Figure 2.3: In the input-output formalism the photons at port 1 and 2 are coupled to the cavity photons, which enables the calculation of the cavity transmission (reflection) properties. The figure is taken from Ref. [53]

The transmission, S_{21}, and the reflection, S_{11} are determined by the following equations [53]:

$$S_{21} = \left.\frac{d_{\text{out}}}{c_{\text{in}}}\right|_{d_{\text{in}}=0} \tag{2.33}$$

$$S_{11} = \left.\frac{c_{\text{out}}}{c_{\text{in}}}\right|_{d_{\text{in}}=0} \tag{2.34}$$

where the output photons at port 2 are measured when there is input at port 1 and but no input to port 2 for S_{21}, and the output photons at port 1 are measured when there is input at port 1 and but no input to port 2 for S_{11}. The reflection and transmission spectra in full are given by

$$S_{11} = \left[-1 + \frac{\kappa_1^{(c)}}{i(\omega_c - \omega) + \frac{\kappa_1+\kappa_1^{(c)}}{2} + \frac{g^2}{i(\omega_m-\omega)+\frac{\beta_m}{2}}}\right] \tag{2.35}$$

$$S_{21} = \frac{\sqrt{2\kappa_1\kappa_2}}{i(\omega-\omega_c) - (\kappa_c+\kappa_1+\kappa_2) + \frac{g}{i(\omega-\omega_m)-\beta_m}} \tag{2.36}$$

where κ's in the above equation describe the internal and external loss rates of the cavity, and β_m is the loss-rate for the magnons. Equations 2.35 and 2.36 are used for analysis in chapter 4, sections 4.3 and 4.4, respectively.

The analysis for the experiment done with the Bruker cavity in chapter 4, section 4.2, require the modification of the reflection spectra, S_{11}, in Eq. 2.35, as two cavity resonant modes are found both of which interact with the magnons in the field-polarised phase of Cu_2OSeO_3 sample. The general form of the interaction Hamiltonian can be extended to describe cavity photon-magnon system that has multiple cavity modes [54]. The interaction of the two cavity modes and a magnon mode (illustrated in Fig. 2.4) is described by the following Hamiltonian in the rotating wave approximation (RWA) as [55]

$$\begin{aligned} H_0/\hbar = \omega_1 a_1^\dagger a_1 + \omega_2 a_2^\dagger a_2 + \omega_m m^\dagger m \\ + g_1(a_1^\dagger m + a_1 m^\dagger) + g_2(a_2^\dagger m + a_2 m^\dagger), \end{aligned} \tag{2.37}$$

where $a_1^\dagger$ (a_1) is the creation (annihilation) operator for microwave cavity photons at frequency ω_1, $a_2^\dagger$ (a_2) is the creation (annihilation) operator for microwave cavity photons at frequency ω_2, $m^\dagger$ (m) is the creation (annihilation) operator for magnons at frequency ω_m, and g_1 (g_2) is the coupling strength between the magnon mode and the first (second) cavity mode. Again, utlising the input-output formalism theory [56, 57], one can write the following Heisenberg-Langevin equations:

$$\dot{a}_1(t) = -\frac{i}{\hbar}[a_1(t), H_{\mathrm{SYS}}] - \frac{\kappa_1^{(\mathrm{cpl})}}{2} a_1(t) - \frac{\sqrt{\kappa_1^{(\mathrm{cpl})}\kappa_2^{(\mathrm{cpl})}}}{2} a_2(t) + \sqrt{\kappa_1^{(\mathrm{cpl})}}\, a^{(\mathrm{in})}(t), \tag{2.38}$$

$$\dot{a}_2(t) = -\frac{i}{\hbar}[a_2(t), H_{\mathrm{SYS}}] - \frac{\kappa_2^{(\mathrm{cpl})}}{2} a_2(t) - \frac{\sqrt{\kappa_1^{(\mathrm{cpl})}\kappa_2^{(\mathrm{cpl})}}}{2} a_1(t) + \sqrt{\kappa_2^{(\mathrm{cpl})}}\, a^{(\mathrm{in})}(t), \tag{2.39}$$

$$\dot{m}(t) = -\frac{i}{\hbar}[m(t), H_{\mathrm{SYS}}], \tag{2.40}$$

$$a_{in}(t) + a_{out}(t) = \sqrt{\kappa_1^{(\mathrm{cpl})}}\, a_1(t) + \sqrt{\kappa_2^{(\mathrm{cpl})}}\, a_2(t), \tag{2.41}$$

where a_{in} and a_{out} are the external input and output fields, $\kappa_1^{(\mathrm{cpl})}$ and $\kappa_1^{(\mathrm{cpl})}$ are coupling constants between cavity fields and the external fields. The Hamiltonian $H_{\mathrm{SYS}} = H_0 + H_{\mathrm{B}}$ describes the cavity modes and the magnon mode, where the Hamiltonian, H_0, is given by Eq. 2.37, and H_{B} describes the dissipation inside the cavity due to the interaction with a heat bath.

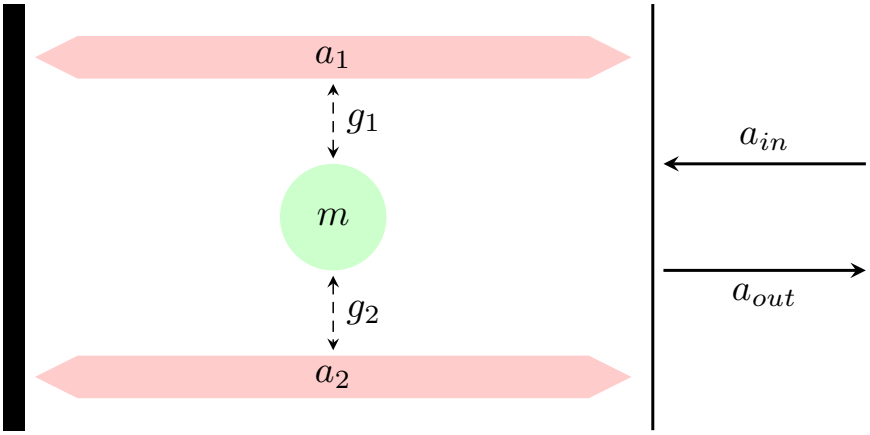

Figure 2.4: A schematic representation of the two cavity fields, the magnon mode, and the input and output fields for a single-sided cavity. The figure is taken from reference [55].

By assuming that solutions should be in the form of $a_1(t) = a_1 e^{-i\omega t}$, $a_2(t) = a_2 e^{-i\omega t}$, etc., one can obtain the following equations:

$$(-i\omega)a_1 = \left(-i\omega_1 - \frac{\kappa_1}{2}\right)a_1 - ig_1 m - \frac{\kappa_1^{(\mathrm{cpl})}}{2}a_1 - \frac{\sqrt{\kappa_1^{(\mathrm{cpl})}\kappa_2^{(\mathrm{cpl})}}}{2}a_2 + \sqrt{\kappa_1^{(\mathrm{cpl})}}a^{(\mathrm{in})}, \tag{2.42}$$

$$(-i\omega)a_2 = \left(-i\omega_2 - \frac{\kappa_2}{2}\right)a_2 - ig_2 m - \frac{\kappa_2^{(\mathrm{cpl})}}{2}a_2 - \frac{\sqrt{\kappa_1^{(\mathrm{cpl})}\kappa_2^{(\mathrm{cpl})}}}{2}a_1 + \sqrt{\kappa_2^{(\mathrm{cpl})}}a^{(\mathrm{in})}, \tag{2.43}$$

$$(-i\omega)m = -ig_1 a_1 - ig_2 a_2 + \left(-i\omega_m - \frac{\gamma_m}{2}\right)m, \tag{2.44}$$

$$a_{in} + a_{out} = \sqrt{\kappa_1^{(\mathrm{cpl})}} a_1 + \sqrt{\kappa_2^{(\mathrm{cpl})}} a_2. \tag{2.45}$$

where ω_1, ω_2, and ω_m are resonant frequencies of the cavity modes and the magnon mode, respectively, κ_1 and κ_2 are dissipation rates of the cavity modes, and γ_m is the dissipation rate of the magnon mode. By solving those equations, the following expression for S_{11} is found [55] as:

$$S_{11} = \frac{a_{out}}{a_{in}} = -1 + \frac{\kappa_1^{(\mathrm{cpl})} F_2 + \kappa_2^{(\mathrm{cpl})} F_1 - 2\sqrt{\kappa_1^{(\mathrm{cpl})} \kappa_2^{(\mathrm{cpl})}} F_3}{F_1 F_2 - F_3^2}, \tag{2.46}$$

where the following notations are used:

$$F_1 = i(\omega_1 - \omega) + \frac{\kappa_1 + \kappa_1^{(\mathrm{cpl})}}{2} + \frac{g_1^2}{i(\omega_m - \omega) + \frac{\gamma_m}{2}}, \tag{2.47}$$

$$F_2 = i(\omega_2 - \omega) + \frac{\kappa_2 + \kappa_2^{(\mathrm{cpl})}}{2} + \frac{g_2^2}{i(\omega_m - \omega) + \frac{\gamma_m}{2}}, \tag{2.48}$$

$$F_3 = \frac{\sqrt{\kappa_1^{(\mathrm{cpl})} \kappa_2^{(\mathrm{cpl})}}}{2} + \frac{g_1 g_2}{i(\omega_m - \omega) + \frac{\gamma_m}{2}}. \tag{2.49}$$

2.6 X-ray Magnetic Circular Dichorism

In order to probe the electronic structure and local environment of crystalline and amorphous materials, the X-ray absorption spectroscopy (XAS) has proven to be an extremely powerful tool, where extensive literature on this work can be found in references [58, 59, 60]. The absorption coefficient, μ(E), of the sample under investigation is measured in a XAS experiment as a function of the incident photon energy, E, in proximity of an absorption edge of one of the chemical species in the sample. X-ray absorption near-edge spectroscopy (XANES) represents the region in the vicinity of before and after the absorption edge (a few tens of eV) which is the key interest of this thesis in chapter 5 for investigating the presence of orbital moment in $Cr_2Ge_2Te_6$ single crystal.

X-ray magnetic circular dichroism (XMCD) technique is based on the differ-

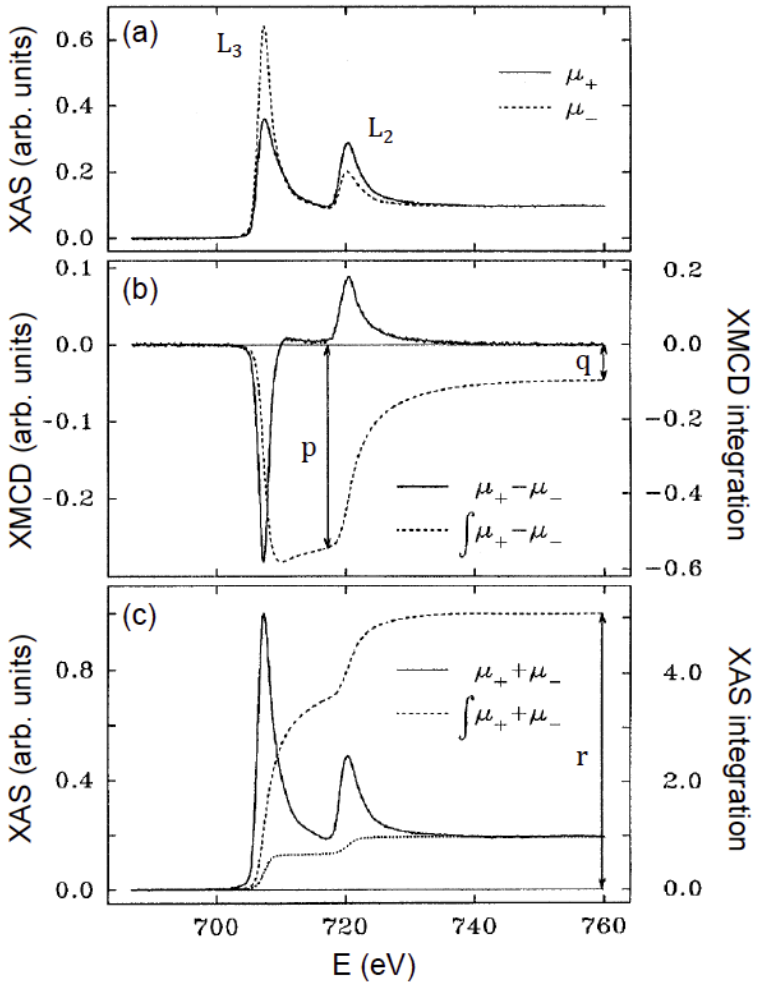

Figure 2.5: XAS and XMCD spectra of iron (Fe) for illustrating the well-known sum-rule analysis technique by Chen et al and the figure is adapted from Ref. [61]. (a) $L_{2,3}$ absorption spectra of Fe measured for opposite directions of an applied magnetic field. (b) The XMCD signal (solid) line and the corresponding integrated signal (dashed) line derived from the absorption spectra shown in (a), where p and q highlight the integrated signal at the L_3 and L_2 post-edge, respectively. (c) Sum of the absorption spectra shown in (a) (solid line) and the corresponding integrated signal after subtraction of two-step-like function (dotted line) for edge-jump removal, and r highlights the total integrated signal across $L_{2,3}$ edges.

ence in X-ray absorption of right and left-handed circularly polarised light depending on the presence of net magnetisation in the material under study [62, 63, 64]. In a XMCD study, generally, the magnetic sample is field-polarised by applying external magnetic field and the absorption coefficient is measured close to an absorption edge for different relative orientations of the magnetisation and the angular

momentum of the incident photons. The is achieved by either reversing the magnetic field direction or the helicity of the incident photons. Then, the difference, i.e. the XMCD signal, is sensitive to the component of the magnetisation along the photon angular moment [64]. The success of the XMCD as a standard technique for probing magnetic properties of samples was due to the introduction of the well-known $sum-rules$ [65, 66], as it directly relates the integral of dichroic signal over the relevant absorption edges to the orbital (μ_L) [65] and spin (μ_S) [66] magnetic moment of the absorbing atoms. The sum-rules, following Chen et al. [61] method, are written as:

$$\begin{aligned} \mu_L \ [\mu_B/\text{atom}] &= -\frac{4q}{3r}(10-n_d) \\ \mu_S \ [\mu_B/\text{atom}] &\approx -\frac{6p-4q}{r}(10-n_d) \end{aligned} \tag{2.50}$$

where n_d is the 3_d electron occupation number and the integrals p, q and r are given by

$$\begin{aligned} p &= \int_{L_3} (\mu^+ - \mu^-) \ dE \\ q &= \int_{L_3+L_2} (\mu^+ - \mu^-) \ dE \\ r &= \int_{L_3+L_2} (\mu^+ + \mu^-) \ dE \end{aligned} \tag{2.51}$$

where $\mu^+(E)$ [$\mu^-(E)$] correspond to the spectrum measured for parallel [anti-parallel] orientation of magnetisation and photon angular momentum, such that $\mu^+(E) - \mu^-(E)$ is the XMCD signal, and E is the energy of the incident x-ray photons. Fig. 2.5 shows the application of the sum-rules on Fe sample as an example [61], and similar analysis are adopted to analyse the XMCD spectra obtained for the $Cr_2Ge_2Te_6$ sample and the temperature dependence of the orbital moment is extracted for different crystallographic directions.

2.7 Magneto-Transport

In samples with presence of net magnetisation, the spin-orbit coupling term allows the interaction between the spin-$\frac{1}{2}$ charge carriers and magnetisation [67]. The in-

ternal magnetisation and the externally applied magnetic field can then play a role in the electrical transport in magnetic materials. Hence, the magneto-transport effects are experimentally significant for probing the magnetisation direction and strength.

The changes in electrical resistance in ferromagnetic materials associated with the direction of magnetisation relative to the applied current is known as anisotropic magnetoresistance (AMR). The effect discovered by William Thomson [68], where he observed an increase the longitudinal resistance of iron and nickel with a magnetic field applied longitudinally, and a decrease with a field applied transversely. The longitudinal resistivity [69] is given by

$$\rho_{xx} = \rho_{\perp} + (\rho_{||} - \rho_{\perp}) \cos^2 \theta, \tag{2.52}$$

where θ is the angle between the magnetisation and current, and the corresponding term in the transverse resistivity [70] is given by

$$\rho_{xy} = -(\rho_{||} - \rho_{\perp}) \cos \theta \sin \theta, \tag{2.53}$$

and is known as the planar Hall effect. The ratio of the change in resistivity ($\Delta\rho$) to transverse resistivity is defined as the AMR, given as

$$\text{AMR} = \frac{\Delta\rho}{\rho_{\perp}} \, . \tag{2.54}$$

The microscopic origin of AMR is explained by the presence of spin-orbit interaction as proposed by Smit [71]. The difference in resistivity for the relative orientations of the applied current direction and magnetisation is caused by the number of scattering events, where the number of available sites for scattering is different between parallel and perpendicular orientations. The longitudinal resistance change as a function of externally applied magnetic field is measured to probe the magnetic state of sodium (Na) intercalated $Cr_2Ge_2Te_6$ sample in chapter 6.

Chapter 3

Experimental Techniques

The main experimental techniques used in this thesis are presented in this chapter. These include the cavity photons interaction with the magnons in Cu_2OSeO_3 sample by means of Bruker MD5 cavity, STO and helical resonators used in chapter 4. The co-planar waveguide (CPW)-FMR technique is discussed which is used to study magnetisation dynamics in chapters 5 and 6. The I-10 beam-line at the Diamond Light Source facility is briefly mentioned which is used for the XMCD work in chapter 5. The magneto-transport measurement technique is also discussed which is used in chapter 6.

3.1 Cavity – FMR

Three different resonant microwave cavities are used to study the spin dynamics in Cu_2OSeO_3, (i) a commercial Bruker MD5 microwave cavity to investigate the interaction of cavity photons with magnons in the field-polarised, helical and conical magnetic phases of Cu_2OSeO_3, (ii) STO resonator for the interaction with the counter-clockwise (CCW) skyrmion phase and helical resonator for breathing-mode skyrmion phase.

3.1.1 Bruker MD5 Cavity

The schematic of the experimental setup used to probe microwave X-band spectroscopy in chapter 4 in order to study the dynamics in the field-polarised, helical and conical magnetic phases is shown in Fig. 3.1. A commercial Bruker MD5 microwave cavity, where the single crystal sample of Cu_2OSeO_3 is placed in the sap-

phire dielectric ring resonator mounted inside a metallised enclosure. The cavity is then placed in a helium-flow cryostat, which resides between the poles of an electromagnet. The external magnetic field from the electromagnet is perpendicular to the microwave magnetic field in the Bruker cavity. A coupling loop antenna is used to resonate the microwave cavity. The signal from the Vector Network Analyser (VNA) is guided via the microwave coaxial cables to the antenna. The microwave reflection S parameter $|S_{11}|$ is measured as a function of external magnetic field and microwave probe frequency.

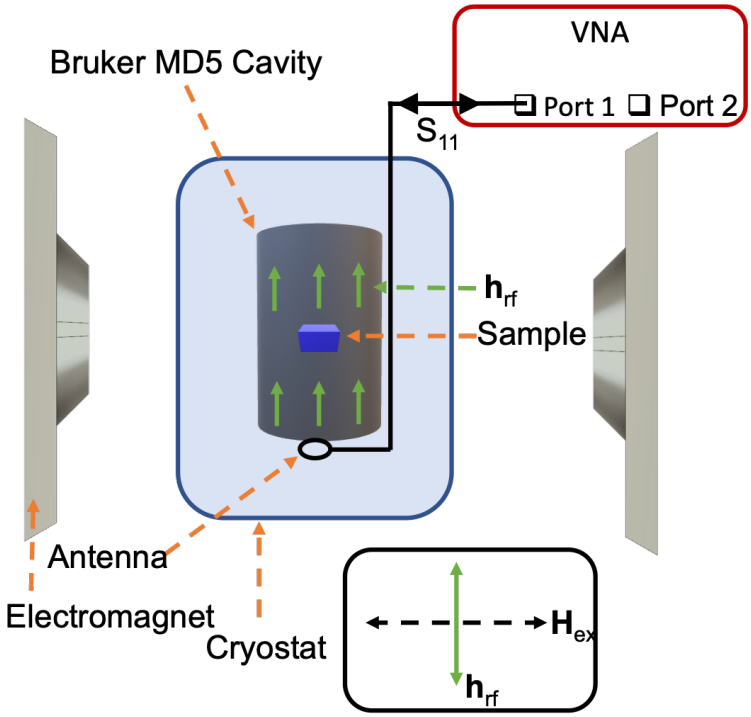

Figure 3.1: Schematic view of the experimental setup used with the Bruker cavity.

The cavity supported two microwave modes [72], the primary mode $TE_{01\delta}$ with the resonance frequency of about $\omega_1/2\pi \approx 9.74$ GHz and the hybrid-mode $HE_{11\delta}$ with resonance frequency of $\omega_2/2\pi \approx 9.24$ GHz. The $TE_{01\delta}$ mode is the transverse electric mode which has no axial electric field component and hybrid $HE_{11\delta}$ mode have both axial electric and magnetic field components [73]. The quality factor Q_1 of the primary-mode resonance in the cavity is tuned by adjusting the position of a coupling loop antenna. A slightly under-coupled cavity with $Q_1 = 5 \times 10^3$ is used in the experiment. The quality factor of the hybrid-mode resonance

ia found to be independent of the coupling loop antenna, and is about $Q_2 \approx 100$.

Numerical simulations of the sapphire dielectric ring resonator cavity are carried out by using CST Microwave Studio software [1] and can be seen in Fig. 3.2. The sample is modelled as a dielectric sphere with the radius $r = 2$ mm, the relative magnetic permeability $\mu_r = 1$, and the relative electrical permittivity $\varepsilon_r \approx 12.5$ [74]. The simulation results confirmed that the cavity supports two microwave modes: a primary $TE_{01\delta}$ mode with the resonance frequency of about $\omega_1/2\pi \approx 9.8$ GHz (Fig. 3.2 (a-b)) and a hybrid $HE_{11\delta}$ mode with the resonance frequency of about $\omega_2/2\pi \approx 9.56$ GHz (Fig. 3.2 (c-d)). The microwave magnetic field of the primary mode is parallel to the axis of the dielectric resonator, and magnetic energy density W_m is concentrated inside the cavity bore (Fig.3.2 (a)). The effective magnetic mode volume for the primary cavity resonance can be estimated as [75, 76, 77]

$$V_1 = \frac{\int (\frac{1}{2}\varepsilon_0\varepsilon_r E^2 + \frac{1}{2}\mu_0\mu_r H^2)dV}{\mu_0\mu_r H^2_{max}} = \frac{\int (W_e + W_m)dV}{2W_{m,max}}, \tag{3.1}$$

where ε_0 is the vacuum permittivity, $\varepsilon_r = \varepsilon_r(x,y,z)$ is the relative electrical permittivity at a given point, $E = E(x,y,z)$ is the microwave electric field, μ_0 is the vacuum permeability, $\mu_r = \mu_r(x,y,z)$ is the relative permeability, $H = H(x,y,z)$ is the microwave magnetic field, H_{max} is the maximum value of the microwave magnetic field, W_e and W_m are microwave electrical and magnetic energy densities, and the integration is taken over the total volume of the system. A value of, $V_1 \approx 230\,\text{mm}^3$, is obtained for the primary mode resonance from the numerical simulations.

An overlap coefficient η_1 is calculated in order to take account of a slight non-uniformity of the distribution of the microwave magnetic field across the sample and it is required for calculating the coupling strength between the cavity photons and magnons in Cu_2OSeO_3 in Chapter 4 [76, 77]:

$$\eta_1 = \sqrt{\frac{\int_{V_s} \mu_0\mu H^2 dV}{\mu_0\mu H^2_{max} V_s}} = \sqrt{\frac{\int_{V_s} W_m dV}{W_{m,max} V_s}}, \tag{3.2}$$

where $V_s = \frac{4}{3}\pi r^3$ is the volume of the sample used in the numerical model, and the

[1] This was done with the help of Dr. L. V. Abdubrakhimov.

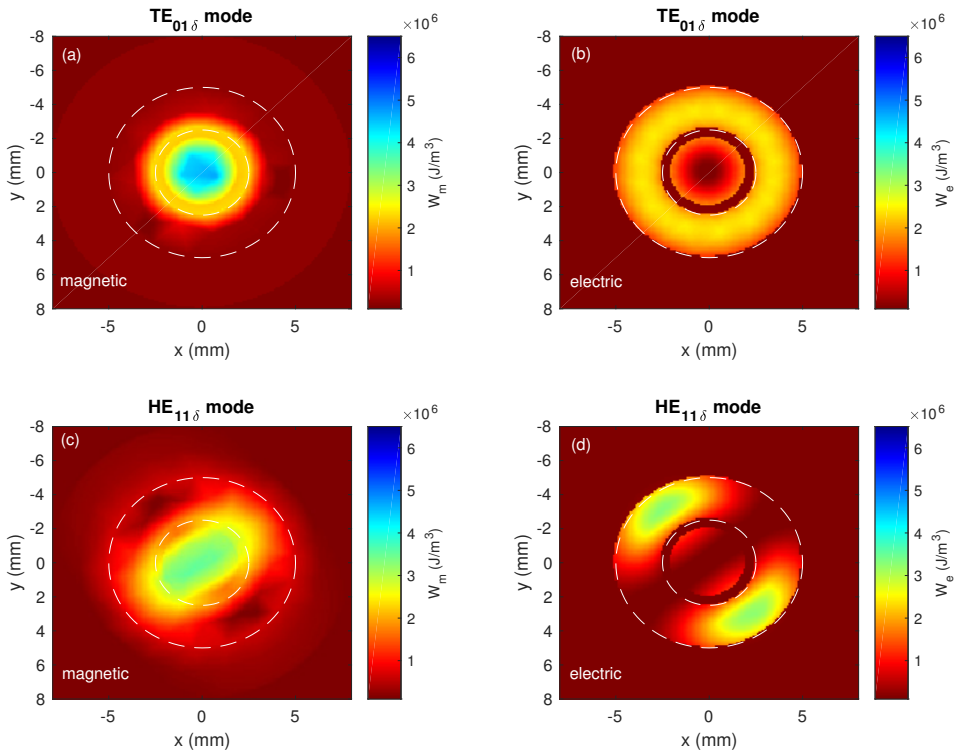

Figure 3.2: Numerical simulation results of the dielectric resonator cavity. The distribution of magnetic (W_m) and electric (W_e energy densities for the primary cavity mode (a-b) and the hybrid cavity mode (c-d) are shown in the center horizontal plane, which is perpendicular to the primary axis of the dielectric ring resonator. The dashed white lines show the contour of the dielectric ring resonator.

integration is taken over the sample volume. The overlap coefficient is numerically estimated as $\eta_1 \approx 0.85$ for the primary mode of the cavity.

The hybrid $HE_{11\delta}$ mode is found to be a double-degenerate axially-asymmetric mode. The magnetic component lied in the plane perpendicular to the axis of the dielectric resonator at the site of the sample. Two mutually perpendicular orientations of microwave magnetic field (two polarizations) are possible, as the $HE_{11\delta}$ mode is degenerate. The distributions of microwave magnetic and electric energy densities for one of two possible polarisations are shown in Fig. 3.2 (c-d)). Only one polarisation of the $HE_{11\delta}$ mode is taken into account in calculating the coupling strength between the photons and magnons in Chapter 4. The microwave magnetic field (for the one polarization) at the site of the sample is perpendicular

to the external dc magnetic field and the hybrid mode with another polarization did not interact with the ferrimagnetic mode. The effective magnetic mode volume for $HE_{11\delta}$ (one polarisation) is estimated as $V_2 \approx 290\,\mathrm{mm}^3$, and the overlap coefficient was $\eta_2 \approx 0.83$.

3.1.2 STO & Helical Resonators

The dielectric strontium titanate (STO) and helical (helically wrapped copper wire) resonators are used to study the interaction of microwave photons with the counter-clockwise (CCW) and breathing skyrmion phases, respectively, in Cu_2OSeO_3 sample. The Bruker cavity discussed in the previous section is not used as the primary cavity mode resonance frequency is much greater than what is needed to excite the skyrmion resonance.

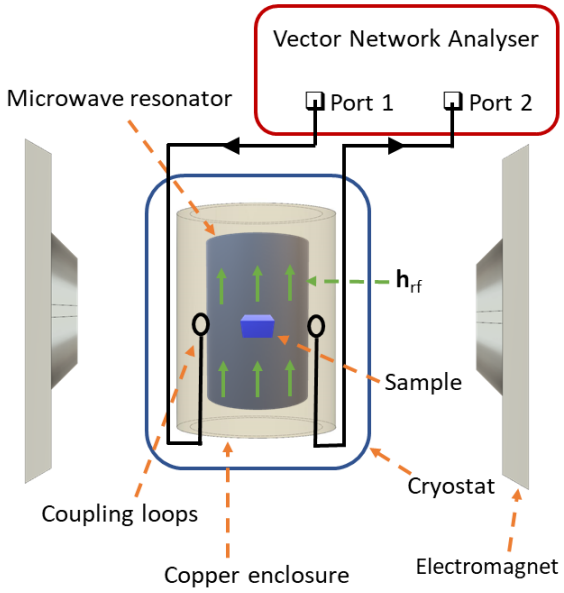

Figure 3.3: Schematic view of the experimental setup used with the STO and helical resonators. The resonators are held in the helium-4 cryostat, and the cryostat sat in between the poles of the electromagnet. The coupling to excite the resonance in the resonators is achieved by connecting two microwave lines from the VNA to the coupling loops in the copper cavity.

The experimental setup of the cavity resonance experiment with both the STO and helical resonators is shown in Fig. 3.3. The resonators (including the sample) are held in a copper cavity inside of helium-4 cryostat system, which is placed in

between the poles of the electromagnet. Adjustable antennae loops are placed into the sides of the copper cavity (i.e. next to the STO and helical resonators) in order to couple the microwave energy into the resonators. Two coaxial cables are used to guide the microwave signal from the two-ports of the VNA to the coupling loops.

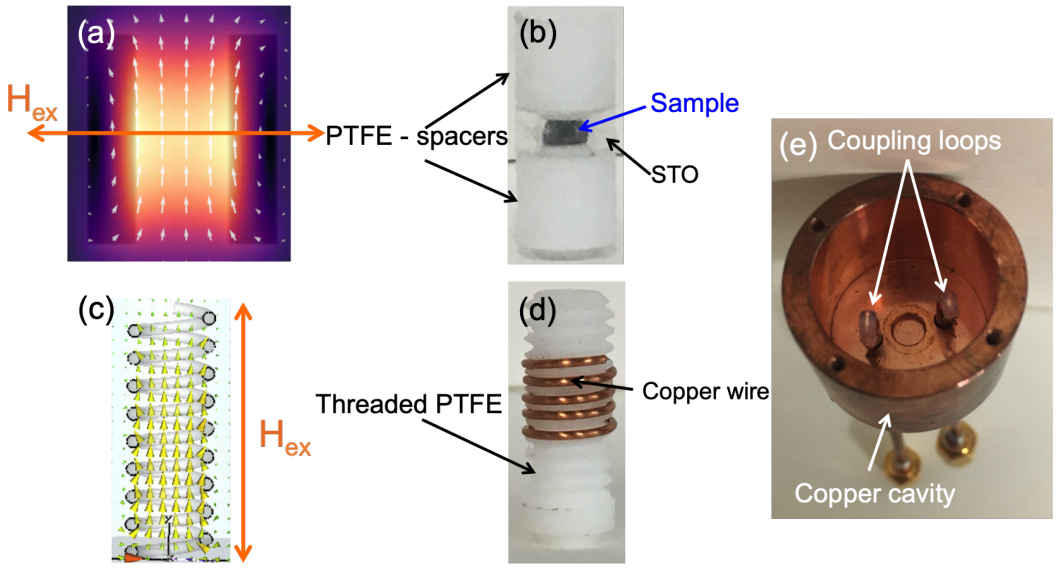

Figure 3.4: (a) Show the orientation of the magnetic field vectors (white lines) inside the STO resonator being perpendicular to the external magnetic field. (b) The Cu_2OSeO_3 sample placed inside the transparent STO resonator held by the PTFE spacers. (c) Shows the microwave magnetic field (yellow arrows) being parallel to the external magnetic field in the helical resonator. (d) The helical resonator is realised by the winding the copper wire on a threaded PTFE and sample was placed inside of the PTFE. (e) The copper cavity where both the STO and helical resonators are held with the help of PTFE.

The STO resonator consists of a hollow cylinder with height ≈ 2.8 mm, outer diameter ≈ 6.3 mm and inner diameter ≈ 3.0 mm (Fig. 3.4 (a) and (b)). This is held inside a copper cavity with diameter ≈ 19.0 mm and height 14.0 mm by PTFE spacers. At 57.5 K, the relative electric permittivity is estimated to be $\varepsilon_r \approx 3410$ [73]. The excitation of the fundamental mode in the STO resonator is via a pair of coupling loops [78], oriented such that they are normal to the axial (microwave) magnetic field component h_z. The fundamental, $TE_{01\delta}$, mode for the STO is found to be resonant at $\omega_c/2\pi \approx 0.97$ GHz, and the excited magnetic field orientation is perpendicular to the external magnetic field, i.e. the condition required to excite the CCW skyrmion mode. The helical resonator [79] is realised by winding the copper

wire (wire diameter ≈ 0.5 mm) on a screw-like threaded PTFE sample holder, with the height ≈ 5 mm, coil diameter ≈ 5 mm and 5 number of turns. The fundamental mode for the helical resonator is found to be resonant at $\omega_c/2\pi \approx 1.42$ GHz, and it lies in the correct frequency window for exciting the breathing skyrmion mode. The helical resonator is placed in the cryostat in such a way that the excited magnetic field orientation is parallel to the external magnetic field (Fig. 3.4 (c) and (d)). Another essential for parameter for evaluating the quality of resonators is the quality factor (q-factor), where the loaded q-factor i.e. where it includes the coupling to the input and output ports is defined as $Q_L = \omega_0/\Delta\omega$ (ω_0 is the resonant frequency and $\Delta\omega$ is full-width-half-maximum describing the loss-rate) [73]. The q-factors are experimentally found to be, $Q_{\text{STO}} = 1 \times 10^3$ and $Q_{\text{helical}} = 300$, for the STO and helical resonators, respectively.

As mentioned earlier for the case of Bruker cavity in the previous section, measurements are performed using the vector network analyser (VNA), where the resonances are probed in reflection (Bruker MD5 cavity) and transmission (STO and helical resonators) mode and the one or two-ports are used to couple the resonators to the microwave lines leading to the VNA, respectively. The transmission and reflection of power in two-port network device (VNA) is described by the scattering or *S*-parameter [73].

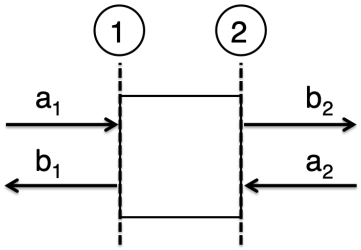

Figure 3.5: Incident, transmitted and reflected power upon and from a two-port device. Figure is adapted from Ref. [73].

Figure 3.5 shows the relationship between the reflected, transmitted and incident power in a two-port (i.e. VNA) device, and the related *S*-parameter matrix [80] is given by

$$\begin{pmatrix} b_1 \\ b_2 \end{pmatrix} = \begin{pmatrix} S_{11} & S_{12} \\ S_{21} & S_{22} \end{pmatrix} \begin{pmatrix} a_1 \\ a_2 \end{pmatrix} \tag{3.3}$$

where the forward scattering parameter S_{21} for example is defined as the ratio of incoming power to outgoing power if the power is incident upon port-one ($a_1 \neq 0$) and the second-port if terminated by a load equal to the system impedance (so power incident on port-two is zero, $a_2 = 0$), and it is given by

$$S_{21} = \frac{b_2}{a_1}. \tag{3.4}$$

3.2 CPW − FMR

The broadband ferromagnetic resonance (FMR) experiment is performed using the setup illustrated in Fig. 3.7, where a co-planar waveguide (CPW) is used that created microwave magnetic fields of variable frequencies. The dynamic magnetic field (rf-field) created by the CPW exerts a torque on the magnetisation, which leads to its precession. The frequency and amplitude of the precession is determined by the frequency and amplitude of the applied microwave field, as well as by the resonance condition of the sample.

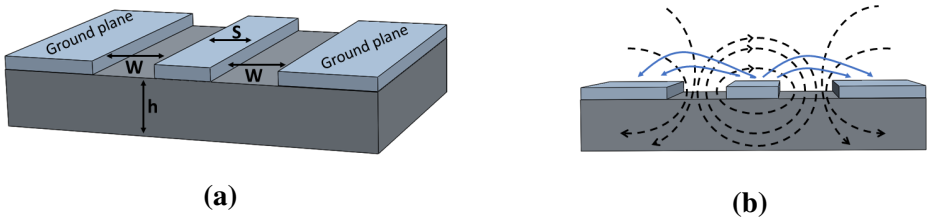

Figure 3.6: (a) A schematic drawing of the coplanar transmission waveguide, where the central signal line of width s is separated by air gaps of width w from the ground planes. The relation between s, w and h (thickness of dielectric substrate) determines the impedance of the waveguide. (b) Shows the rf-field distribution around the conductors of the coplanar transmission line: dashed lines show the magnetic field force lines, and the solid lines show the electric field force lines.

The impedance of the CPW is important for consideration when using it for FMR experiments, and it can be matched to 50 Ω by carefully controlling the parameters shown in Fig. 3.6, where the easiest parameters to vary are the signal line

width (s) and the distance from the ground plane to signal line (w) [80]. In order to employ the broadband oscillatory magnetic field to the sample, a copper CPW on a Rogers PCB, with a center conductor width of 1 mm and a gap of 0.5 mm, is used. The impedance matching of the microwave circuitary connnected to the CPW is carefully matched to 50 Ω.

The sample is centrally placed on top of the CPW, as shown in Fig. 3.7, where the CPW is mounted inside a copper sample box and features two SMP connectors, allowing the connection to microwave circuitry. The sample box sits inside a cryostat (with a temperature range of 3 K - 300 K) and the cryostat is placed between the poles of the electromagnet. The CPW is connected (via microwave coaxial cables) to the VNA which serves both as the source as well as the detector of the high-frequency signal. The VNA range of 50 MHz - 40 GHz allowed broadband FMR spectroscopy to be performed. The transmitted rf-current in the CPW creates h_{rf}, which is orthogonal to the externally applied static field H_{ex}, a condition to excite the resonance in the FMR technique.

The FMR spectra is obtained by the measuring the absorption (transmission) spectrum, S_{21}, as a function of probe frequency and externally applied magnetic field. If the FMR condition is met, the sample absorbs part of the microwave signal sent through the CPW and alters the phase of the transmitted microwave signal. This absorption is generally then fitted with symmetric and anti-symmetric Lorentzian function. By analysing these absorption peaks, the resonance position and the linewidth can be determined, and from these measurements it is possible to obtain the dynamic properties for a given magnetic sample. The advantage of the broadband FMR setup is the possibility of obtaining a full field vs. frequency map of the resonances, not being limited to a single frequency as compared to a cavity-based FMR setup. This allows determination of magnetic properties such as the demagnetisation field and magnetic anisotropy, and the spectroscopic g-factor. Measuring the FMR linewidth as a function of frequency allows one can extract both α, which characterises the frequency dependent contribution to the damping, as well as the inhomogeneous frequency independent contribution to the linewidth.

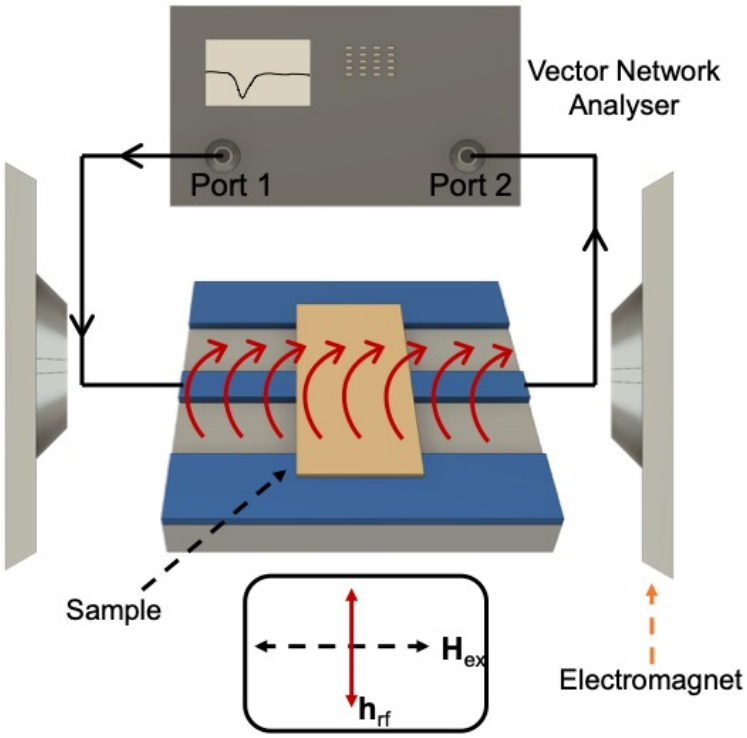

Figure 3.7: A schematic illustration of experimental setup for CPW-FMR technique. The sample is placed on top of a 50 Ω-matched CPW which is connected by microwave coaxial cables to the VNA. The CPW is placed in the cryostat and the cryostat is placed in between the poles of the electromagnet.

3.3 XMCD: Beam-line I-10

The XMCD experiments at Cr $L_{2,3}$ edges (E_{L3} = 574.1 eV and E_{L2} = 583.8 eV) are performed on the single crystal samples of $Cr_2Ge_2Te_6$ at the Diamond Light Source (DLS) facility in I-10 absorption line station, where the schematic of the X-ray beam-line is shown in Fig. 3.8 (a). The energy of this beam-line of soft X-rays can be tuned in the window of $400 - 1600$ eV, and hence it allowed to probe Cr edges where scans in the energy range of 570 eV to 600 eV were taken to obtain the XANES spectra for $Cr_2Ge_2Te_6$ sample in order to investigate the orbital moment quantitatively.

A full operational methodology of I-10 beam-line can be found in reference [81]. The main components of the absorption line station consist of a high-field superconducting magnet, where a magnetic field of up to $\approx$ 14 T can be applied, and a helium-4 cryogenic system able to reach temperatures between 5 K - 420

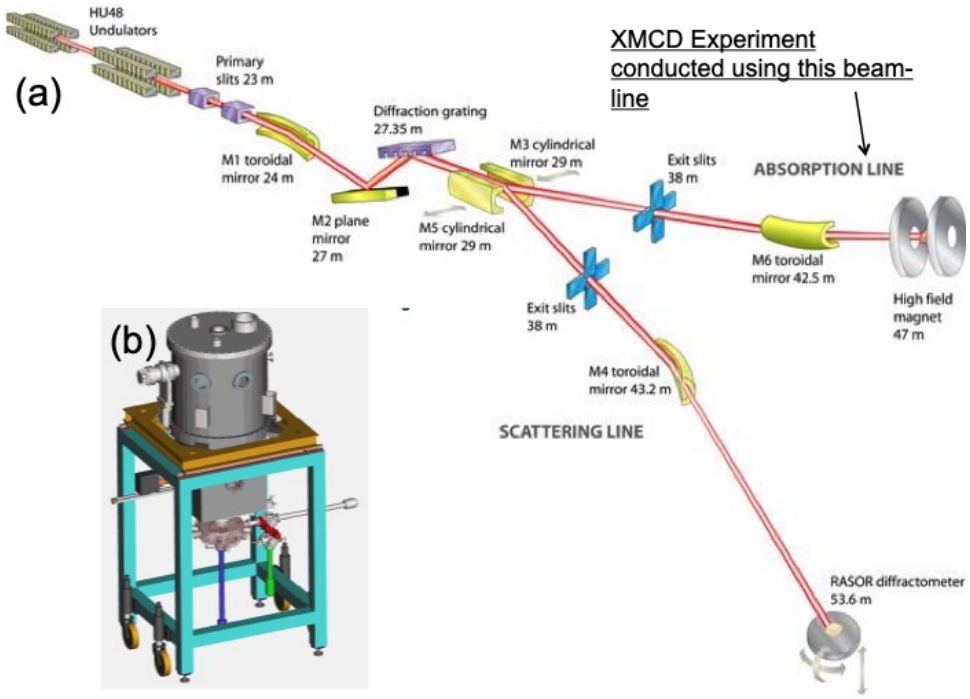

Figure 3.8: A schematic illustration of the beam-line (I-10) at the Diamond Light Source facility used for the Dichroism experiments. (b) Drawing of the chamber where the sample is held including the high-field magnet at the absorption line station. The figure is adapted from Ref. [81].

K (Fig. 3.8 (b)). The sample is placed in ultra-high vacuum (UVH) and can be moved in both directions normal to the incident beam and can be rotated about the vertical axis for varying the X-ray angle of incidence. The sample is cleaved in nitrogen (N_2) environment bag just before loading it into the UHV-magnet sample environment. The dichroic spectra for circularly polarised X-rays are collected in both total-electron yield (TEY) and total fluorescence yield (TFY) detection mode [81]. A magnetic field of 2 T is applied parallel ($\theta = 0°$) and perpendicular ($\theta = 75°$, containing the maximum contribution from the in-plane component at this angle) to the out-of-plane (c-axis) orientation, respectively, with the X-ray wavevector being parallel to the magnetic field in the out-of-plane direction and at an angle to the magnetic field in the in-plane orientation. The measurements are collected varying temperature from 10 K to 80 K in steps of 10 K.

3.4 Transport Measurements

A four-point measurement technique is quite often used to conduct electrical measurements [82] in order to identify the carrier type (electrons or holes), carrier density and resistivity (or mobility) for characterising the electronic properties of materials. A van der pauw [83, 84] (four-point) experimental technique, as illustrated in Fig. 3.9, is used to study the magneto-transport in the sodium (Na) intercalated $Cr_2Ge_2Te_6$ samples. The sample is placed on a copper PCB patterned with four electrical contacts. The epoxy-resin is used to make the contact between the PCB and the sample as shown in Fig. 3.9 (a). The PCB together with the sample is placed

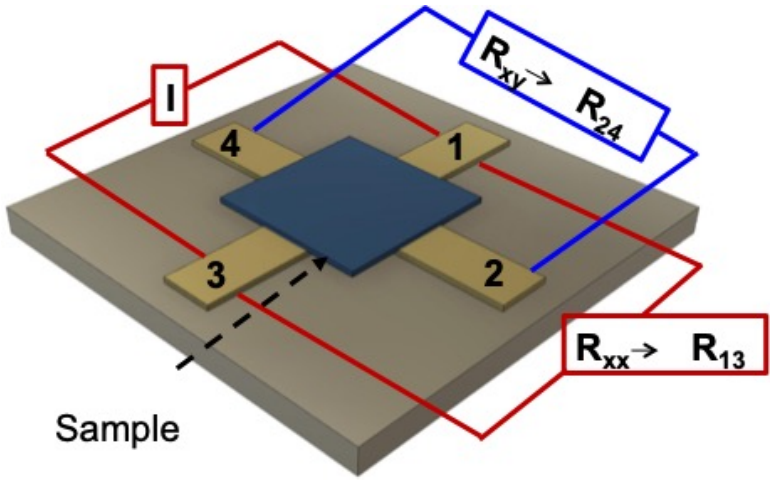

(a)

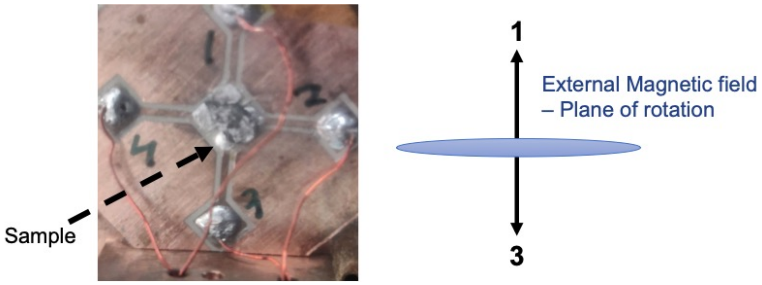

(b)

Figure 3.9: (a) A schematic illustration of the four-point electrical measurement technique. The current, I, is applied across contacts 1 to 3 and resistance is measured through contacts 1 to 3 (R_{13}, longitudinal resistance) and through contacts 2 to 4 (R_{24}, transverse resistance). (b) The left-side shows the actual image of the PCB with the sample on top and the right-side highlights that the PCB was placed in such a way in the cryostat that the external magnetic field plane of rotation is always perpendicular to the contacts 1 and 3.

in the cryostat which sits between the poles of an electromagnet.

The current, I, is applied across the contacts 1 and 3 (I_{13}), and the longitudinal resistance (R_{13}) and the transverse resistance (R_{24}) are measured (using the standard Keithley 2000 multimeter) corresponding to (R_{xx}) and (R_{xy}) signals, respectively. The PCB (and sample) is placed in the cryostat in such a way where the plane of rotation of the externally applied magnetic field is always perpendicular to applied current direction (I_{13}), as highlighted in Fig. 3.9 (b). Using this setup, the magneto-transport response is measured in Na intercalated $Cr_2Ge_2Te_6$ in the temperature range of 15 K - 200 K.

Chapter 4

Photon-Magnon Interaction in Cu_2OSeO_3

The light-matter interaction in the context of coupling between microwave photons and particle ensembles has been studied in a wide range of condensed-matter systems. These include ensembles of magnetically ordered spins [85, 86, 87, 88] , paramagnetic spins [89, 90] and two-dimensional electron systems [91, 92]. According to the Dicke model [93, 94, 95], the coupling strength between a photon and an ensemble of N particles scales with the square root of N, as $g_N = g_0\sqrt{N}$. The magnetic materials due to the large density of spins (hence large N) and low magnetic losses are exceptionally attractive, where the high number of spins makes them easy to couple to the photons and the low losses giving long coherence times.

The strong coherent coupling phenomenon between cavity photons and magnons results in creating a hybridised state between the two. This leads to the formation of a quasi-particle, the cavity-magnon-polariton (CMP), displaying an intriguing dual spin-photon nature as the two systems coherently exhange energy before it is lost to the environment via damping [96]. Quantum information processing as quantum memories [97, 98] and quantum transducers [99] are particularly interesting applications which could be made possible due to the hybrid spin-ensemble-photon systems. New phenomenon of photon-magnon coupling has been recently observed in ferrimagnet, yttrium iron garnet (YIG), these include a coherent coupling between a superconducting qubit and a magnon [100], cavity

mediated coherent coupling between multiple ferromagnets [101, 102] and spin pumping in a coupled magnon-photon system [103].

In strong coupling studies of magnetic materials, the focus has remained on the ferrimagnetic materials having $(\mathbf{S}_i \cdot \mathbf{S}_j)$-like Heisenberg exchange interaction between the neighbouring spins $\mathbf{S}_i$ and $\mathbf{S}_j$. The spin configurations in these systems are collinear in the ground state, and the excitation i.e. the uniform precession ferromagnetic mode (or Kittel mode) has been used in the studies of magnon-photon coupling. Coupling photons to non-collinear and non-trivial spin systems has however attracted interest too [104, 105]. The spin-spin exchange interaction in chiral magnets consists of two terms: (i) symmetric Heisenberg exchange favouring collinear spin configuration, and (ii) antisymmetric $(\mathbf{S}_i \times \mathbf{S}_j)$-like Dzyaloshinskii-Moriya interaction (DMI), which tends to twist the neighbouring spins [106]. The interplay of the two exchange interactions leads to the formation of non-collinear spin textures in chiral magnets, such as helical, conical, and skyrmion spin textures [107]. The coupling of cavity-photons and non-collinear spin textures is a potentially rich and an unexplored area.

In this chapter, the results of interaction between cavity photons and the different spin-textures in Cu_2OSeO_3 are presented. The study of interaction in the collinear, helical and conical phases was carried out by Bruker MD5 cavity. In the collinear phase, a strong coupling regime was observed between magnons and the two modes of the cavity. In the conical phase, the fundamental helimagnon mode coupled dispersively to cavity modes and the magnetic phase diagram of Cu_2OSeO_3 was reconstructed. A hybridised state between a cavity mode and a higher-order helimagnon, a helimagnon polariton, was found in the helical phase. A strontium titanate (STO) resonator was used to probe the coupling of photons to counter clockwise (CCW) skyrmion mode. The breathing mode skyrmions and photons interaction was carried out by the helical resonator. The strong coupling regime between cavity photons and skyrmions was not observed in this study.

4.1 Copper-Oxoselenite Sample

Copper-Oxoselenite, Cu_2OSeO_3, is a chiral magnetic insulator which belongs to the non-centrosymmetric cubic space group $P2_13$ (point group T) [108]. The unit cell of Cu_2OSeO_3 [1]is shown in Fig. 4.1 (a). There are sixteen $Cu^{2+}(3d^9)$ ions within the unit cell, and the Cu-ions are located on the vertices of corner-shaped tetrahedra. The four Cu^{2+} spins in a 3-up-1-down spin configuration in the tetrahedral cluster, as illustrated in Fig. 4.1 (b), make the basic magnetic building block of Cu_2OSeO_3, and this behaves as a spin triplet with the total spin $S = 1$ [109, 110].

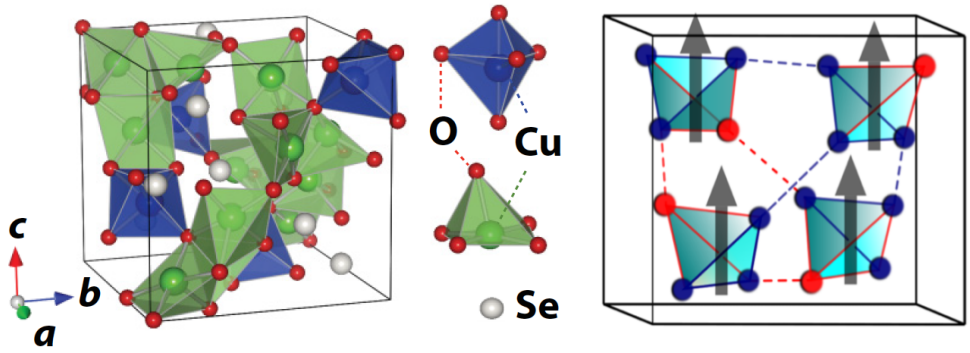

(a) (b)

Figure 4.1: (a) Crystal structure of Cu_2OSeO_3 from Seki et al [111]. (b) The magnetic unit cell of Cu_2OSeO_3, where blue (spin-up) and red (spin-down) represent $Cu^{2+}S = 1/2$ spins. The 3-up-1-down spin triplet ($S = 1$) clusters are indicated in light blue with spin in grey and the figure is taken from Versteeg et al study [110].

In Cu_2OSeO_3, multiple magnetic phases stabilise under the presence of an external magnetic field. Different magnetic exchange interaction having a hierarchy of energy scales operate in this sample and other cubic chiral helimagnets. The exchange energy, J, favours the collinear spin alignment between the neighbouring spins in short distances, but the Dzyaloshinskii-Moriya exchange interaction, D, prefers the perpendicular spin alignment, and thus the competition between the two leads to the twisting of magnetisation, with momenta ($Q = D/J$) on long scales, into chiral spin structures [112]. Below the Curie temperature, $T_c \approx 58K$, the system of $S = 1$ spin triplet clusters forms helical, conical and skyrmion spin textures with

[1]Dr. S. Seki (University of Tokyo) provided the Cu_2OSeO_3 samples used for experiments in this chapter. More information about the sample growth is given in appendix A.

variation of an external magnetic field [113], as can be seen in Fig. 4.2 (a). The qualitative magnetic phase diagram of Cu_2OSeO_3 is shown is Fig. 4.2 (b). The critical fields, H_{c1} and H_{c2} highlights the transition from one magnetic phase to the other below T_c. The system is in long range helimagnetic order at zero magnetic field and this persists up to the field value of H_{c1}. Increasing the field value from H_{c1} leads to a transition to conical phase followed by a transition spin polarised state at H_{c2}. The skyrmion phase in bulk Cu_2OSeO_3 exists within a narrow temperature window ($\approx$ 2 K) for moderate magnetic fields [113]. Above T_c, the system goes to the paramagnetic state.

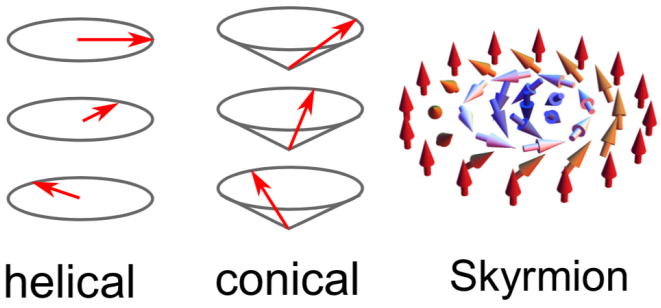

(a)

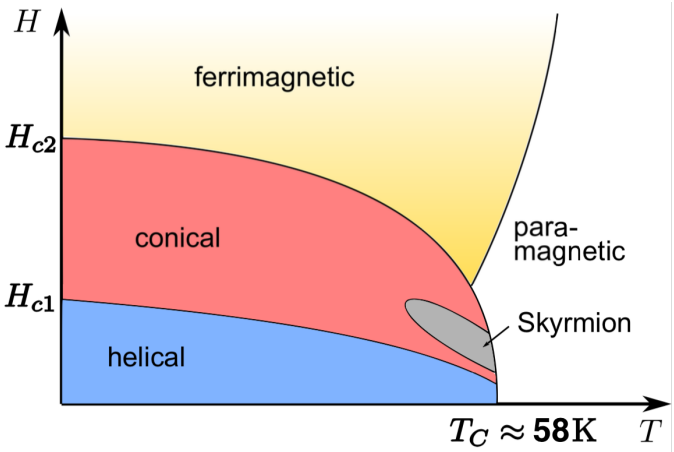

(b)

Figure 4.2: (a) Illustration of non-collinear spin textures: helical, conical and skyrmion states in cubic chiral magnets. (b) Qualitative magnetic phase diagram of Cu_2OSeO_3 taken from Ref.[55]

4.2 Collinear Phase

The cavity-FMR technique using the Bruker MD5 cavity to study the magnon-photon coupling in the collinear phase of Cu_2OSeO_3 is shown in chapter 3. The microwave X-band spectroscopy was performed in the temperature range of 5–100 K. The sample was placed in the anti-node of the microwave magnetic field of the primary cavity mode and external magnetic field was applied perpendicular to it. The reflection parameter $|S_{11}|^2$ was measured as a function of microwave probe frequency and external magnetic field. The orientation of the external magnetic field relative to the crystallographic axes of sample was chosen arbitrarily.

The raw experimental data and the background corrected data from the reflection experiment at the temperature of 5 K is shown in Fig. 4.3. The anti-crossing feature can even be clearly seen in the raw data (Fig. 4.3(a)), where this feature was accompanied by a background pattern comprising of horizontal stripes. The first set of data processing was carried out by correcting the raw experimental data. The presence of a standing-wave in coaxial cables and the vector network analyser caused the background to have this sort of stripe feature, and it was due to the impedance mismatch at the input of the cavity resonator. The standing-wave profile, with different microwave pieces being taken into account at different values of the external magnetic field, was calculated by a piecewise-defined function, where the anti-crossing feature did not affect the standing-wave background. The corrected data was obtained by subtracting the standing-wave profile the raw experimental data (4.3. (b)).

The cavity used in this experiment supported two microwave modes as discussed earlier in chapter 3. The primary mode $TE_{01\delta}$ with the resonance frequency of about $\omega_1/2\pi \approx 9.74$ GHz and the hybrid mode $HE_{11\delta}$ with the resonance frequency of $\omega_2/2\pi \approx 9.24$ GHz. It was found that both the cavity modes interacted with the magnons in the collinear phase of Cu_2OSeO_3. This was confirmed by the visible anti-crossings (as can be seen in Fig. 4.4 (a)) observed at the degeneracy points where the excitations of the cavity modes (i.e. photons) and the excitations of the magnetic system (magnons) started hybridising, and where otherwise the cavity

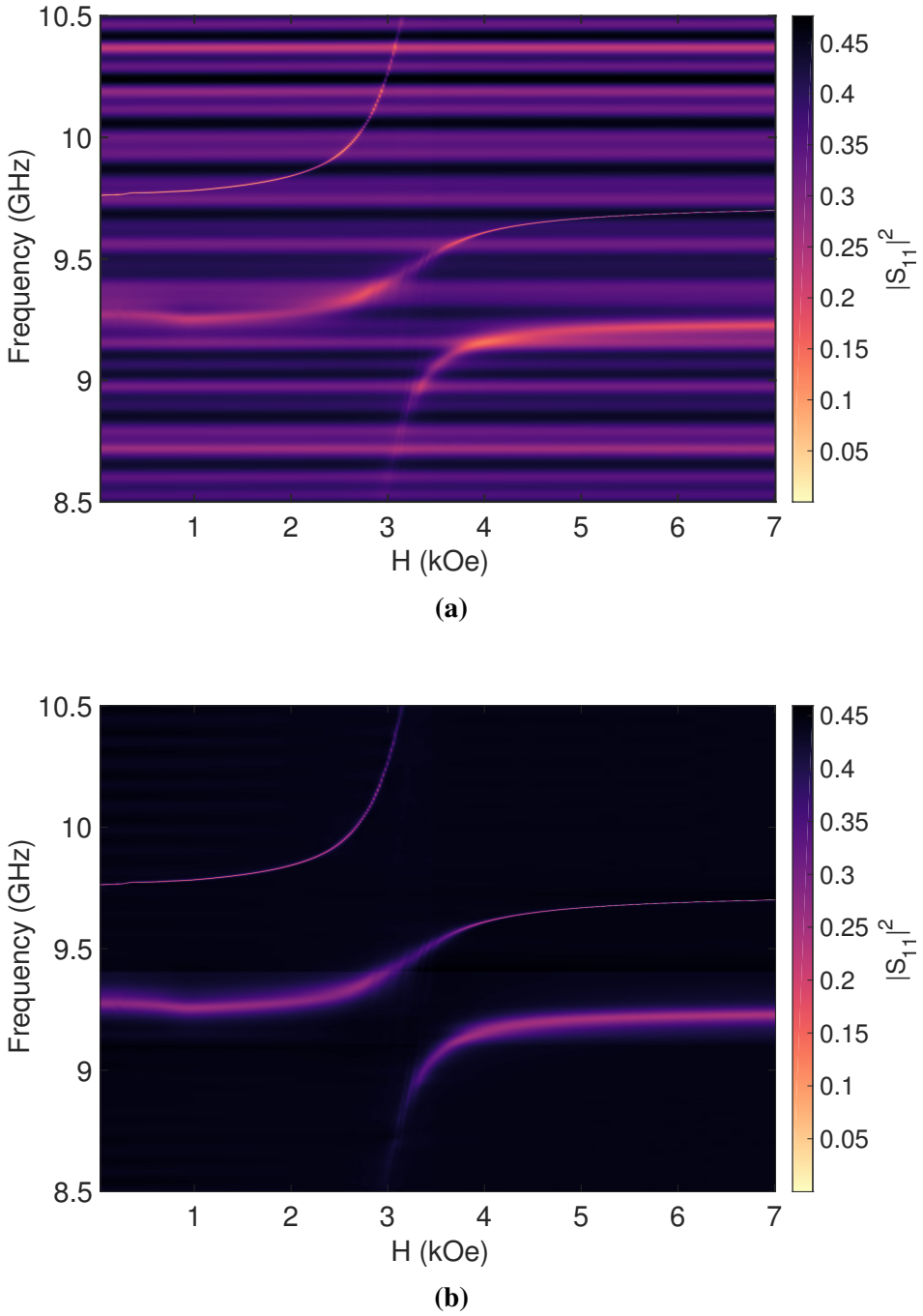

Figure 4.3: The standing wave background correction. (a) An example of the experimental data at 5K. (b) The same data after correction.

modes would have intersected the magnon mode as highlighted by the white dashed lines in Fig. 4.4 (a).

The magnon mode frequency, $\omega_m/2\pi$, shown in 4.4 (a) as a dashed white line corresponds to the uniform excitation precession mode, the so-called Kittel mode.

The field dependent magnon dispersion (along the magnetic easy axis orientation) of the ferromagnetic resonance mode reads

$$\omega_m/2\pi = \gamma(H_0 + H_{\text{demag}}) \tag{4.1}$$

where H_0 is the externally applied magnetic field, H_{demag} is the demagnetising field, and $\gamma/2\pi = 28$ GHz/T is the electron gyromagnetic ratio. The resonance frequency ω_m of the Kittel mode can be tuned by changing the externally applied magnetic field until it is matched close to the unperturbed cavity photon frequency ω_c, and the excited states of the ferrimagnetic-cavity system i.e. magnons and photons enter the strong coupling regime depending on the damping/loss rates of the individual systems as discussed below.

The interaction of the two cavity modes and a magnon mode is described (as earlier shown in chapter 2) by the following Hamiltonian in the rotating wave approximation (RWA) as

$$\begin{aligned} H_0/\hbar = {} & \omega_1 a_1^\dagger a_1 + \omega_2 a_2^\dagger a_2 + \omega_m m^\dagger m \\ & + g_1(a_1^\dagger m + a_1 m^\dagger) + g_2(a_2^\dagger m + a_2 m^\dagger), \end{aligned} \tag{4.2}$$

where $a_1^\dagger$ (a_1) is the creation (annihilation) operator for microwave cavity photons at frequency ω_1, $a_2^\dagger$ (a_2) is the creation (annihilation) operator for microwave cavity photons at frequency ω_2, $m^\dagger$ (m) is the creation (annihilation) operator for magnons at frequency ω_m, and g_1 (g_2) is the coupling strength between the magnon mode and the first (second) cavity mode.

In order to reliably extract the coupling parameters i.e. the coupling strengths g_1 and g_2 from the experimental data along with the damping rates of cavity-spin system, the well-known input-output formalism to investigate the resonant hybrid systems, derived earlier in chapter 2, was used. The complex reflection $|S_{11}|$ function for coupling of the two photon modes with a magnon mode in the collinear spin phase is derived as

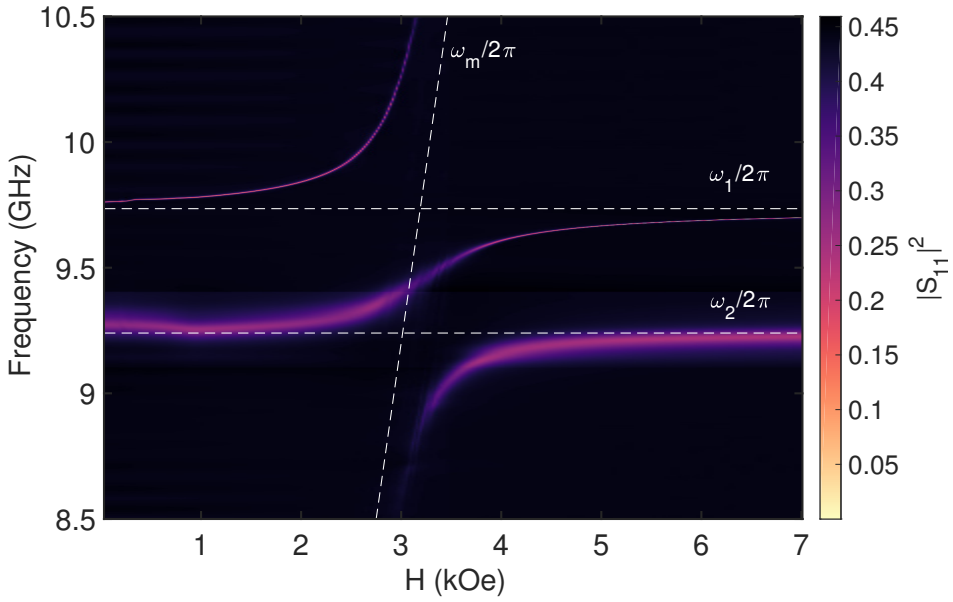

(a)

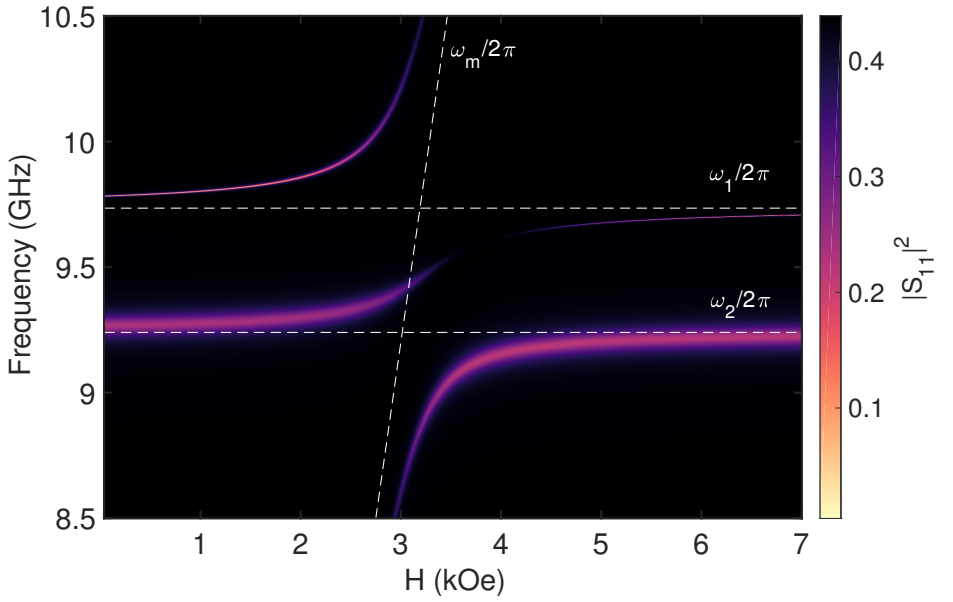

(b)

Figure 4.4: Strong coupling between ferrimagnetic mode of Cu_2SeO_3 and multiple microwave cavity modes: (a) experimental data of microwave reflection $|S_{11}|^2$ as a function of the applied external field and the microwave probe frequency at temperature of $T \approx 5\,\mathrm{K}$, (b) microwave reflection $|S_{11}|^2$ calculated using Eq.(4.3) and parameters described in the text.

$$|S_{11}|^2 = \left| -1 + \frac{\kappa_1^{(c)} F_2 + \kappa_2^{(c)} F_1 - 2\sqrt{\kappa_1^{(c)} \kappa_2^{(c)}} F_3}{F_1 F_2 - F_3^2} \right|^2, \tag{4.3}$$

where

$$F_1 = i(\omega_1 - \omega) + \left(\kappa_1 + \kappa_1^{(c)}\right)/2 + g_1^2(i(\omega_m - \omega) + \gamma_m/2)^{-1},$$
$$F_2 = i(\omega_2 - \omega) + \left(\kappa_2 + \kappa_2^{(c)}\right)/2 + g_2^2(i(\omega_m - \omega) + \gamma_m/2)^{-1},$$
$$F_3 = \sqrt{\kappa_1^{(c)}\kappa_2^{(c)}}/2 + g_1 g_2(i(\omega_m - \omega) + \gamma_m/2)^{-1},$$

and κ_1 (κ_2) is the intrinsic damping rate of the first (second) cavity mode, $\kappa_1^{(c)}$ ($\kappa_2^{(c)}$) is the external loss rate due to the coupling between the first (second) cavity mode and the output transmission line, and γ_m is the damping rate of the magnonic mode. The damping rates here represent the linewidths (full-width half maximum) of the corresponding modes.

The experimental data at 5 K (4.4 (a)) showing the anti-crossing feature associated with strong coupling between the two cavity modes and the magnon mode is well reproduced by using Eq. (4.3. The following parameters were obtained in analysis of the data at 5 K and the calculated spectra as a function of the probe frequency and externally applied magnetic is shown in 4.4 (b), where the coupling strength between the primary cavity mode and magnon mode in the collinear phase was $g_1/2\pi \approx 600\,\text{MHz}$, and $g_2/2\pi \approx 450\,\text{MHz}$, for the coupling between the hybrid cavity mode and magnon mode. The damping rates were found to be $\kappa_1/2\pi \approx 1\,\text{MHz}$, $\kappa_1^{(c)}/2\pi \approx 1\,\text{MHz}$, $\kappa_2/2\pi \approx 60\,\text{MHz}$, $\kappa_2^{(c)}/2\pi \approx 10\,\text{MHz}$ and $\gamma_m/2\pi \approx 50\,\text{MHz}$. The demagnetisation field $H_{\text{demag}} \approx 280\,\text{Oe}$, was used to extrapolate the magnon dispersion (dashed white line) in Eq. 4.1.

The strong coupling regime, which allows the coherent transfer of excitations the resonant systems, is reached when the transfer rate of excitations between the two systems is greater than the damping rate of cavity mode and magnon mode, giving a condition for the strong coupling as $g > \kappa_c, \gamma_m$. It is evident from the calculated parameters at 5 K that the coupling strengths are much greater than the damping rates of both the cavity and magnon modes, $g_1 \gg (\kappa_1 + \kappa_1^{(c)}), \gamma_m$ and $g_2 \gg (\kappa_2 + \kappa_2^{(c)}), \gamma_m$. Hence, the strong coupling condition was realised for both anti-crossing features seen in Fig. 4.4 in the collinear phase of Cu_2OSeO_3. The coupling

was greatest at 5 K, and scaling of the coupling strength (g_1) for the primary mode of the cavity with the magnetisation (proportional to number of spins in the system) is discussed in more detail below.

As mentioned earlier, the damping forces in magnetic systems are essential factors in cavity-magnon-polariton coupling, as the coupling process requires that the energy must be exchanged between the magnon and photon systems before it is lost to damping. Cooperativity, C, is another parameter considered when investigating a coupled system. It quantifies the ratio of the coherent coupling rate g to the incoherent rates of the cavity and magnon dissipation and is given as [114]

$$C = \frac{g^2}{\kappa_c \omega_m}, \tag{4.4}$$

where the strong coupling in the cavity-magnon-polariton systems occurs when $C > 1$, showing an anti-crossing feature in the dispersion. When $C < 1$, other coupling effects such as the Purcell effect [115] or the electromagnetically induced transparency [116] may occur, which will not produce the mode splitting seen within the coupled system but may still influence the dispersion of cavity photons and magnons. In the collinear phase of Cu_2OSeO_3, the cooperativity parameters for both cavity modes are found to be much higher than unity. For the the primary mode, $C_1 = g_1^2/\left(\gamma_m\left(\kappa_1 + \kappa_1^{(c)}\right)\right) \approx 3600$, and for the hybrid mode $C_2 = g_2^2/\left(\gamma_m\left(\kappa_2 + \kappa_2^{(c)}\right)\right) \approx 60$. Also, it is found that the ratio of the coupling strength to the the resonance frequency, $g_1/\omega_1 \approx 0.06$ and $g_2/\omega_2 \approx 0.05$ are close to the condition of the ultra-strong coupling regime ($g/\omega \geq 0.1$), and it is where the coupling strength in two resonantly coupled system is comparable with the frequency of the degeneracy of point of the anti-crossing feature, and new physics beyond the RWA can be explored [87, 117].

The coupling strength between cavity photons and magnons can be estimated theoretically using the following expression [118],

$$g_i^{(\mathrm{th})} = \frac{\eta_i}{2}\gamma\sqrt{\frac{\mu_0\hbar\omega_i}{V_i}}\sqrt{2SN}, \quad (i = 1,2), \tag{4.5}$$

where μ_0 is the vacuum permeability, and as shown in Chapter 3 earlier $V_1 \approx 230\,\mathrm{mm}^3$ ($V_2 \approx 290\,\mathrm{mm}^3$) is the mode volume of the primary (hybrid) cavity resonance. The form factor, η_i ranging from 0 to 1, outlines the spatial overlap between the cavity modes and the magnon mode. When $\eta_i = 0$, the excitation field in the cavity is not either perpendicular to the externally applied magnetic field or contained in the magnetic sample, and $\eta_i = 1$ means that all of the excitation field is perpendicular and in the sample. The form factor calculated in Chapter 3 for the primary mode was $\eta_1 \approx 0.85$ and $\eta_2 \approx 0.83$ for the hybrid mode. S is the total spin and N is the effective spin number. By substituting these and other known parameters in the above equation, the coupling strengths were calculated.

The theoretically estimated coupling strengths at 5 K, using Eq. 4.5, for the primary mode $g_1^{(\mathrm{th})}/2\pi \approx 825\,\mathrm{MHz}$ and and the hybrid mode $g_2^{(\mathrm{th})}/2\pi \approx 700\,\mathrm{MHz}$, were obtained. The theoretical estimate of coupling strength is found to be in good agreement with the experimentally obtained values. The slight disparity between theoretical and experimental values of coupling strengths is thought to be caused by the excitation of additional spin-wave modes ($k \neq 0$) in the magnetic sample and it can be seen as additional faint narrow lines in the experimental data. This leads to the reduction in the effective number of spins taking part in the uniform FMR mode excitation [119], and keeping in mind that the coupling strength is proportional to the number of spins the theoretically estimated values were higher than the ones obtained from the experiment.

The coupling strength scales with the number of spins involved in the interaction between magnons and cavity photons in a coupled system (as can be seen by Eq. 4.5). The experimental results of the coupling strengths obtained in the collinear phase confirms that it is indeed the case where the coupling strengths showed a strong temperature dependence. The temperature dependence of coupling strength for the primary cavity mode g_1 is shown in Fig. 4.5. It can be seen that the experimental data is well described by the square root of net magnetisation, $\sqrt{M(T)}$, function normalised to the value of coupling strength at low temperatures, where it is assumed that the effective number of spins is proportional to M, as $N(T) \propto M(T)$.

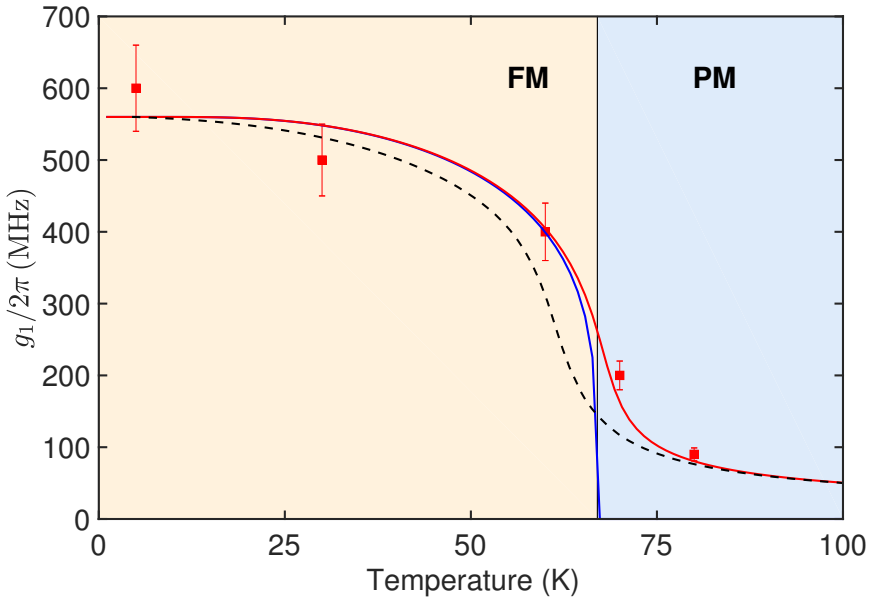

Figure 4.5: Temperature dependence of the coupling strength, g_1, in the ferrimagnetic (FM) and paramagnetic (PM) phases. Experimental data (red squares) points of g_1 obtained in the zero-field-cooled regime and theoretical estimation of $g_1 \propto \sqrt{M(T)}$ for $H = 0$ Oe (solid blue line) and $H = 3$ kOe (solid red line). An estimation of g_1 based on the magnetisation profile of a Cu_2OSeO_3 sample of isotropic shape at the magnetic field of $H_0 = 3$ kOe (with $H_0 ||$ [110]) is shown by the dashed black line (where the SQUID data was used to generate this line).

In Fig. 4.5, the theoretical estimates for the coupling strength were done based on the magnetisation profile[2] of a Cu_2OSeO_3 sample of isotropic shape at the magnetic field of $H_0 = 3$ kOe (dashed black line) and the magnetisation profiles calculated using the Weiss model of ferromagnetism for $H = 0$ Oe (solid blue line) and $H = 3$ kOe (solid red line). A slight difference is found in the theoretical estimates of temperature dependence of g_1 from the two calculation techniques of magnetisation profile from a standard SQUID measurement and the profiles from the Weiss model of ferromagnetism. This difference is attributed due to main reasons (i) different demagnetisation factors for the two samples, and (ii) a temperature gradient present in the helium-flow cryostat where the actual sample temperature not exactly matching the temperature value from the sensor in the cryostat.

The net magnetisation M as a function of temperature and externally applied

[2]The magnetisation profile, $M(T)$, for the sample used in this experiment was not measured directly, but the theoretical estimate of g_1 was done based on $M(T)$ measured using a standard SQUID system by Dr. S. Seki (who also provided the Cu_2OSeO_3 sample).

magnetic field B, $M = M(T,B)$, is calculated using the Weiss model for ferromagnetism [24, 55], which is then used to theoretically estimate the coupling strength as a function of temperature (solid red and blue lines in 4.5). The molecular field is introduced for modelling the ferromagnetic interaction as

$$B_{mf} = \lambda M, \tag{4.6}$$

where λ is a constant parameter, and for a ferromagnet, $\lambda > 0$. The following non-linear equations are self-consistently solved in order to find the magnetisation:

$$M = M_s B_J(y), \tag{4.7}$$

$$y = \frac{g_J \mu_B J(B + \lambda M)}{k_B T}, \tag{4.8}$$

where M_s is the saturation magnetisation as

$$M_s = n g_J \mu_B J, \tag{4.9}$$

and $B_J(y)$ is the Brillouin function given by

$$B_J(y) = \frac{2J+1}{2J} \coth\left(\frac{2J+1}{2J} y\right) - \frac{1}{2J} \coth\left(\frac{y}{2J}\right), \tag{4.10}$$

and μ_B is the Bohr magneton, g_J is a g-factor, J is a spin number, k_B is the Boltzmann constant and n is the spin density. It can be shown that the parameter λ is related to the Curie temperature T_c as [24]

$$\lambda = \frac{3 k_B T_c}{g_J \mu_B (J+1) M_s}. \tag{4.11}$$

In the case of Cu_2OSeO_3 sample used in this experiment, $J = 1$, $g_J \approx 2$, $n = 4/a^3$ (lattice constant $a = 8.93$ Å), and assuming that the $T_c \approx 67K$ at the magnetic field of $B_0 \approx 3$kOe, the above equations are solved numerically in order to obtain the magnetisation profile. The magnetisation profiles for magnetic values of 0 Oe and 3 kOe are calculated [55], which are then used to theoretically estimate the coupling

strength is Fig. 4.5, where the solid red line corresponds to $H = 3$ kOe and solid blue line corresponds to $H = 0$ Oe. Hence, it is found that in the collinear phase, the temperature dependence of the coupling strength is well fitted by the square-root function of magnetisation, meaning that g_1 scales with the number of spins in the system, and it is found to be in agreement with the results of studies of strong coupling in collinear ferrimagnetic systems [120].

4.3 Helical & Conical Spin Textures

The insulating ferrimagnet, Cu_2OSeO_3, compared to other ferrimagnetic systems, for example yitrium iron garnet (YIG) [120], studied previously for the case of strong coupling of cavity photons and magnons is unique as it comprises of different spin textures shown earlier by the phase diagram. The Bruker MD5 microwave cavity, same as for the collinear phase, was used to study the magnon-photon coupling in the non-collinear spin textures, the helical and conical spin phases. The measurements were performed at low magnetic fields as it is where the two phases in the system exist in the phase diagram.

The frequency of the cavity resonance is found to be dependent on the externally applied magnetic field not only in the field-polarised phase, but also in the helical and conical states, as shown in Fig. 4.6 (a-b). In the microwave response, two different features are identified (as highlighted in Fig. 4.6 (a) in the field-up sweep) at magnetic field values H_{c1} and H_{c2} which can be attributed to the helical and conical magnetic phase transitions in Cu_2OSeO_3, respectively. The transition observed at H_{c1}, from helical to conical, is relatively smooth. The smooth transition can be related to the fact that the spin system forms a multidomain structure of flat helices in the helical phase [113], and due to the externally applied magnetic field not being aligned along the high symmetry directions of the crystal structure, the increase of magnetic field can gradually reorient the domains [112].

The transition observed at H_{c2} is from the conical to ferrimagnetic state, and the value of H_{c2} is found to be dependent on the direction of the externally applied magnetic, as can be seen in 4.6 (a-b) where sweeps of field-up (low to high magnetic

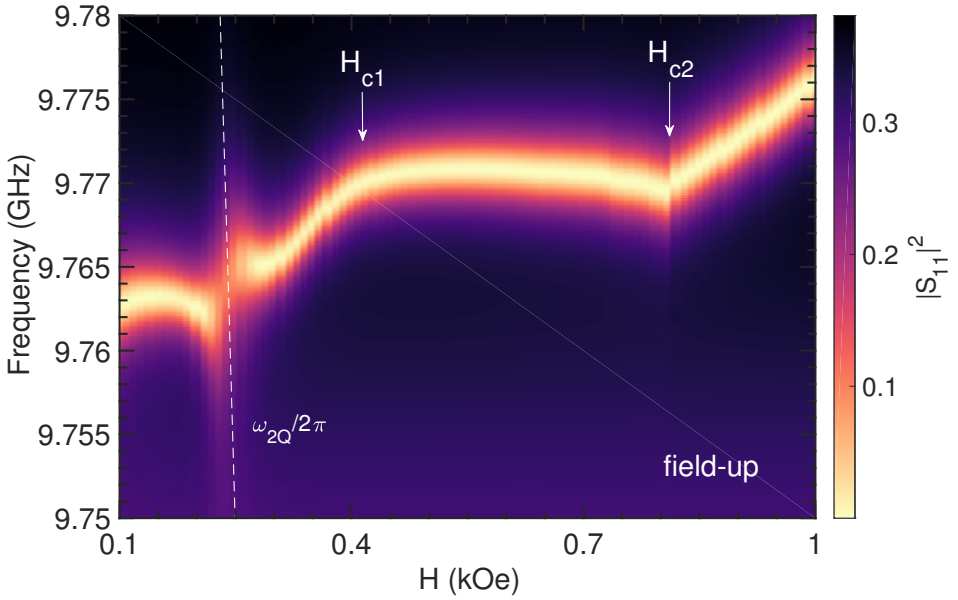

(a)

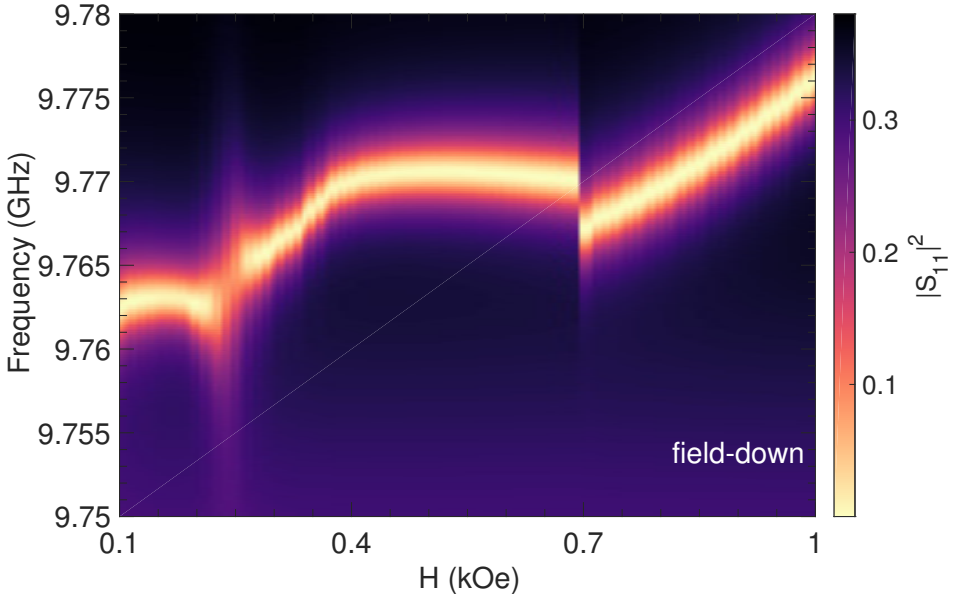

(b)

Figure 4.6: The magnon-photon coupling in non-collinear magnetic states, with microwave reflection $|S_{11}|^2$ measured at 5 K. (a) The magnetic field sweep was performed from low to high field values ("field-up"). Dashed line corresponds to a higher-order helimagnon $k = \pm 2Q$ mode, and an avoided crossing between the helimagnon mode and the cavity mode is clearly visible. H_{c1} and H_{c2} are critical magnetic fields of helical-to-conical and conical-to-ferrimagnetic phase transitions, respectively. (b) The magnetic field sweep was performed from high to low values ("field-down"). The transition from ferrimagnetic to conical phase demonstrated hysteretic behavior.

field) and field-down (high to low magnetic field) show a different magnetic field value of H_{c2}. This hysteretic behaviour is seen only at low temperatures $T \lesssim 40K$, and it can be related to the competing phases of the conical state and the unusual "tilted conical" state recently reported in [121]. The changes in the frequencies of cavity modes are supposed to be caused by the dispersive coupling of microwave photons in cavity and a magnonic mode in the helical and conical states, i.e. helimagnons [112, 122]. The dispersive magnon-photon coupling is qualitatively discussed as the frequencies of the degenerate fundamental $n = \pm 1$ helimagnon modes $\omega_{\pm Q}$ lie well below the cavity resonance frequencies and depends weakly on the magnetic field and a complete theoretical model of helimagnon-photon coupling requires a detailed calculations of spectral weights of helimagnon modes [112]. Therefore, the dispersive magnon-photon coupling to the fundamental helimagnon mode is quite weak in the helical phase $H < H_{c1}$ as the net magnetisation M is small [113]. In the conical phase $H_{c1} < H < H_{c2}$, the increase in the net magnetisation causes the cavity mode to dispersively couple to the helimagnon mode resulting in a shift of the cavity resonance frequency. The net magnetisation is close to its maximum value (i.e. saturation magnetisation) in the ferrimagnetic phase $H > H_{c2}$, and as shown earlier that the magnon-photon coupling scales with the number of spins, the coupling strength to the uniform Kittel mode is high, and the shift of the cavity resonance with the increase of the magnetic field is large. The features identified by magnetic field values of H_{c1} and H_{c2} in Fig. 4.6 (a) are extracted as a function of temperature and the magnetic phase diagram of Cu_2OSeO_3 sample is reconstructed from the field-up measurements of cavity photon and magnon coupling as shown in Fig. 4.7.

In the helical magnetic phase and also in the low magnetic field region in Fig. 4.6 (a-b), a normal-mode splitting feature is observed between the cavity mode and a higher-order helimagnon mode, and the zoomed-in region of this experimentally observed feature at 5 K can be seen in Fig. 4.8 (a). By analogy with the hybrid state created by the coupling of photons and magnons which is the cavity magnon polariton [117, 103, 96], a hybrid helimagnon-photon state can be called a heli-

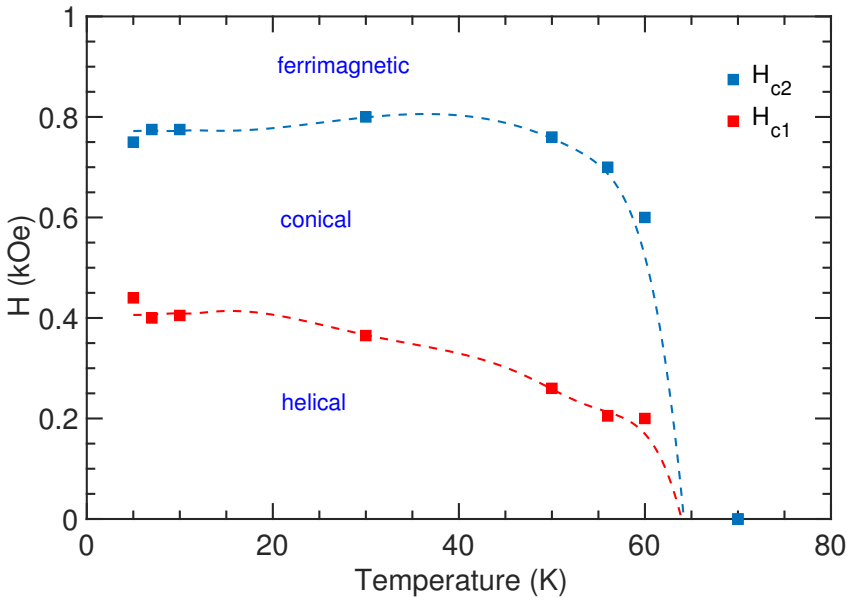

Figure 4.7: The magnetic phase of Cu_2OSeO_3 sample reconstructed from the "field-up" (low to high magnetic field sweep) measurements of H_{c1} and H_{c2}. The dashed lines are for eye guidance.

magnon polariton. The dispersion relation of a helimagnon mode $\omega_{nQ}(H)$ exhibits a negative slope, $d\omega_{nQ}/dH < 0$, contrasting with the dispersion relation of the uniform Kittel mode in the ferrimagnetic phase. The helical phase is characterized by a multidomain structure of flat helices, where the propagation vectors of the different helices are pinned along the preferred axes of the system. The cubic anisotropies of Cu_2OSeO_3 need to be taken into account for an accurate description of helimagnons in the helical phase [112], and instead, an analytical equation is used for the description of magnons in the conical phase [122] as

$$\omega_{nQ} = |n| \frac{\gamma B_{c2}}{1 + N_d \cdot \chi} \sqrt{n^2 + (1+\chi)(1-(B_0/B_{c2})^2)}, \tag{4.12}$$

where χ is the internal conical susceptibiliy ($\chi \approx 1.76$ for Cu_2OSeO_3 [112]), N_d is the demagnetisation factor along the direction of the Q vector, B_0 is the externally applied magnetic field, and B_{c2} is the critical field for the transition between conical and ferrimagnetic phases ($B_{c2} \approx 0.08\,\mathrm{T}$ in this experiment). The relationship between the helimagnon wave vector k and the wave vector of the helical spiral Q is described by the mode number n, as $k = \pm nQ$. The observed helimagnon mode

is determined to be an $n = \pm 2$ mode by tuning the parameters n and N_d (where the demagnetization factor is approximated as $N_d \approx 0.1$), and it is shown by the white dashed line in Fig. 4.8.

In order to quantitatively discuss the avoided crossing feature seen in Fig. 4.8 (a), the input-output formalism description for the coupling between two resonant modes is used to numerically simulate the observed experimental results by using the following equation to calculate the microwave reflection parameter [87]

$$|S_{11}|^2 = \left| -1 + \frac{\kappa_1^{(c)}}{i(\omega_1 - \omega) + \frac{\kappa_1 + \kappa_1^{(c)}}{2} + \frac{g_{2Q}^2}{i(\omega_{2Q} - \omega) + \frac{\gamma_{2Q}}{2}}} \right|^2, \tag{4.13}$$

where ω_{2Q} and γ_{2Q} are the resonance frequency and the linewidth of the helimagnon mode, respectively, and g_{2Q} is the coupling strength between the cavity mode and the helimagnon mode. It is found that the experimental data at 5 K in the helical phase can be partly reproduced (as can be seen in Fig. 4.7 (b)) by tuning the parameters in Eq. 4.13 as $g_{2Q}/2\pi \approx 8.5\,\text{MHz}$, $\kappa_1/2\pi \approx 1.5\,\text{MHz}$, $\kappa_1^{(c)}/2\pi \approx 1.5\,\text{MHz}$, and $\gamma_{2Q}/2\pi \approx 60\,\text{MHz}$. The extracted damping parameters showed that the loss rate of helimagnons in the helical phase is greater than both the loss rate of the cavity and the coupling between the helimagnons and cavity photons, as $\kappa < g_{2Q} < \gamma_m$. Therefore, the experimentally observed normal-mode splitting is attributed to the Purcell effect as the spin relaxation dominates the relaxation of the hybrid system, and the relaxation rate of the cavity photons is increased due to the coupling to the lossy magnons in the spin system [87]. The Cooperativity parameter in this helical phase is $C \approx 0.4$ and hence it is another sign that the system doesn't enter the strong coupling regime as $C < 1$. The higher-order helimagnon mode, ω_{2Q}, was not detected at temperatures $T \gtrsim 30\,\text{K}$ consistent with the earlier reported work on the excitation of helimagnons [122].

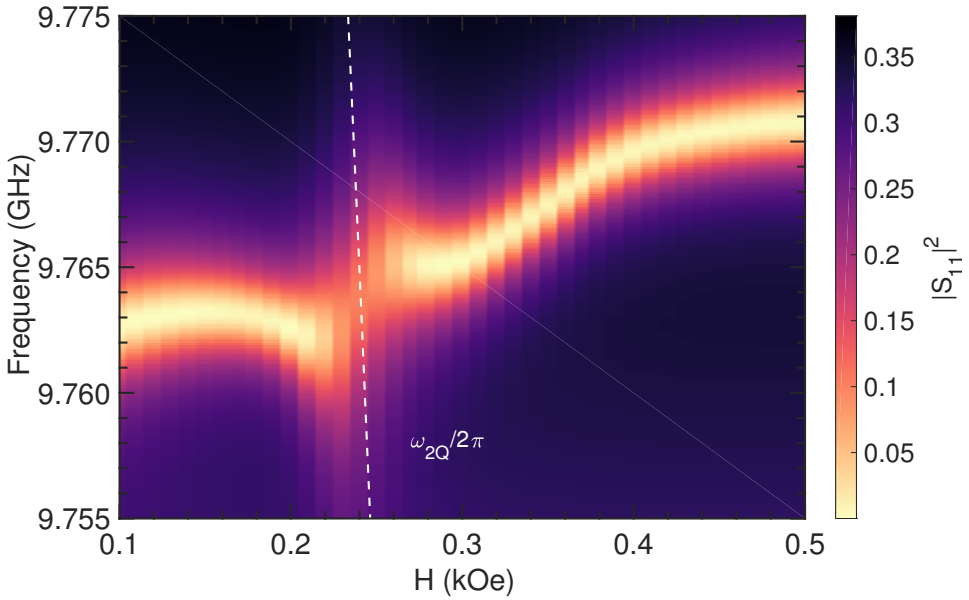

(a)

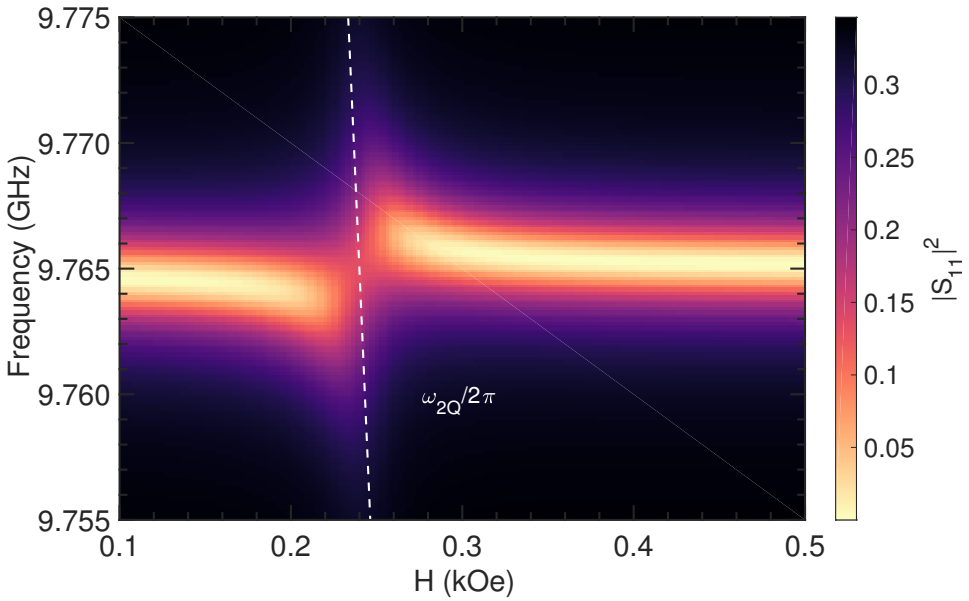

(b)

Figure 4.8: The normal-mode splitting between a cavity mode and a higher-order helimagnon mode in the helical phase. (a) Experimental measured microwave reflection $|S_{11}|^2$ at 5 K. (b) Results of the numerical calculation of $|S_{11}|^2$ for comparison with the experimental data.

4.4 Counter-Clockwise & Breathing Skyrmion Modes

The concept of skyrmion as the quantised topological defeats in a continuous field was initially proposed to account for the stability of hadrons in particle physics [123, 124]. It turned out later that the principle of skyrmions is applicable in various different condensed matter systems, and particularly focusing on the ferromagnetic materials, where skyrmions represent a particle nature with a localised spin texture [125, 126].

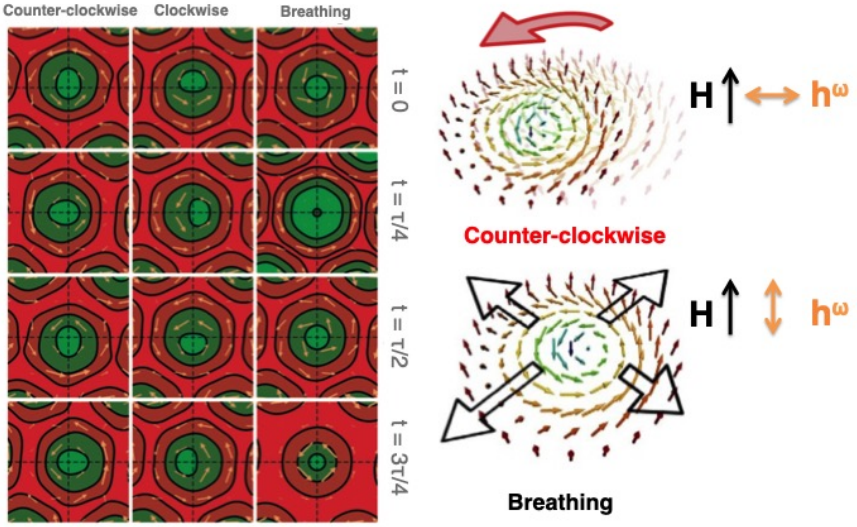

Figure 4.9: (Left panel): Illustration of counter-clockwise and clockwise gyration modes, and the breathing mode in skyrmion phase at different times during a period τ. A plane perpendicular to externally applied magnetic field is shown. The green shading at the centre of the skyrmion cores represents the spins being anti-parallel to the external magnetic field and the surrounding spins highlighted by the red shading. The arrows (orange) highlight the in-plane spin component, and the modified figure is taken from Ref. [112]. (Right panel): Schematic illustration of skyrmion spin textures showing the resonant motions of counter-clockwise mode where the core of skyrmion rotates, and breathing mode where the skyrmion oscillating shrinks and enlarges. The counter-clockwise mode is excited when the external magnetic field, **H**, is perpendicular to microwave field, $\mathbf{h}^{\omega}$, and for the breathing mode **H** is parallel to $\mathbf{h}^{\omega}$, and the figure is taken from Ref. [127].

Similar to vibrations in atomic crystals, i.e. phonons, having a role in lattice dynamics, the vibrations of skyrmions is necessary for the low-energy dynamics of skyrmion crystal. Mochizuki et al. reported the first theoretical study on such spin-vibrational modes, where three internal modes of the skyrmion crystal

were predicted by numerically analysing a two-dimensional spin model using the Landau-Lifshitz-Gilbert equation [128]. The three modes are named, by their real-space configuration, as the counter-clockwise (CCW) mode, clockwise mode and the breathing mode, where the magnetic resonance of these modes are illustrated in Fig. 4.9 (left panel). The resonances comprise of a collective skyrmion core precession in the counter-clockwise and clockwise directions (gyration modes), and the skyrmion core oscillation shrinking and enlarging in the breathing mode. These modes can be excited by an oscillating ($\approx$ GHz frequency) magnetic field being applied either perpendicular or parallel to the static magnetic field. In order to excite the CCW mode, the ac magnetic field should be perpendicular to static magnetic field, and the two field vectors should be parallel relative to each other for the breathing mode as shown in the right panel of Fig. 4.9. The CCW and breathing skyrmion modes were of interest for experimentally investigating the interaction of cavity photons with topological spin textures in Cu_2OSeO_3, as discussed in more detail below.

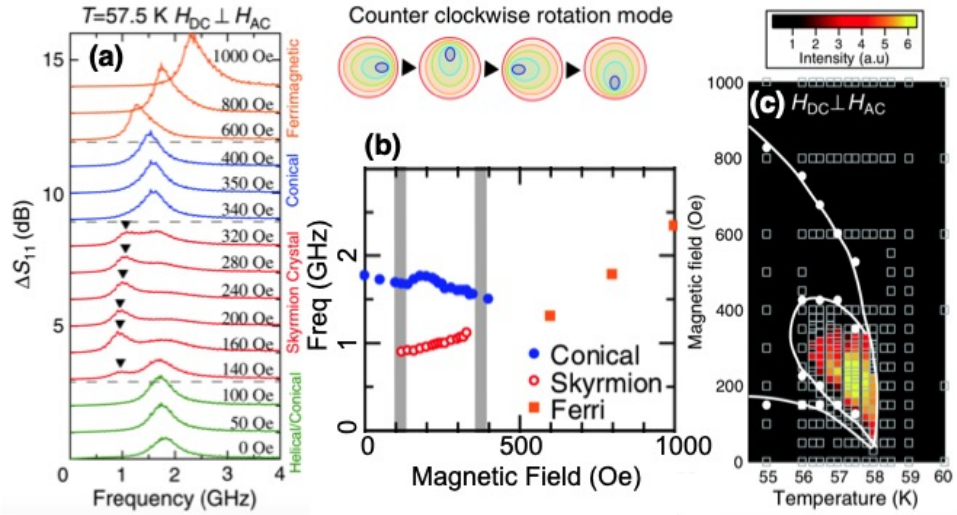

Figure 4.10: (a) Microwave absorption spectra measured (by Onose et al. [129]) for Cu_2OSeO_3 crystal at 57.5 K for different magnetic fields with $\mathbf{H} \perp \mathbf{h}^{\omega}$ configuration. (b) The frequency dependence of magnetic modes, open circles (red), closed circles (blue) and closed squares (orange) corresponding to excitations in skyrmion, conical and ferrimagnetic states, respectively. (c) The counter-clockwise mode resonance intensity plotted in the magnetic field-temperature phase diagram highlighting the skyrmion window for $\mathbf{H} \perp \mathbf{h}^{\omega}$ configuration. (a), (b) and (c) are taken from Ref. [129].

The first experimental realisation of magnetic resonance of collective skyrmion modes in Cu_2OSeO_3 was done by Onose et al. [129]. The microwave response of the skyrmion crystal was measured by the standard broadband resonance technique commonly used in ferromagnetic resonance experiments, i.e. measuring the reflection parameter using a network analyser with sample placed on a microstrip line. The observed resonance peaks, in **H** (applied magnetic field) $\perp$ $\mathbf{h}^{\omega}$ (ac microwave magnetic field) configuration, for different magnetic phases in Cu_2OSeO_3 is shown in Fig. 4.10 (a), and the frequency dependence of the conical, CCW skyrmion and the field-polarised states can be seen in Fig. 4.10 (b). In the bulk form of Cu_2OSeO_3 sample, the skyrmion phase exists in a narrow window of temperature ($\approx$ 2 K) and magnetic field below T_c as confirmed in Fig. 4.10 (c) [129].

As highlighted in Fig. 4.10 (b), the resonance frequency of the CCW skyrmion mode as a function of magnetic field lies in the vicinity of $\approx$ 1 GHz and magnetic field range of $\approx$ 10 - 40 mT. The interaction between the cavity photons and the skyrmions was not realised in the Bruker MD5 cavity used for investigating the coupling in the helical and field-polarised states of Cu_2OSeO_3, as the cavity primary mode resonance was $\approx$ 9.74 GHz.

The STO resonator (as mentioned earlier in chapter 2) with the resonance frequency of the primary mode ($TE_{01\delta}$), $\omega/2\pi \approx 0.965$ GHz at 57.5 K, was used to study the coupling between the CCW skyrmion mode in Cu_2OSeO_3 and microwave photons. The perpendicular configuration between the microwave magnetic field and the static external field was ensured in order to excite the CCW skyrmion mode. The interaction of the CCW skyrmions with cavity photons is experimentally captured for the very first time, and the transmission spectra of microwave absorption parameter, S_{21}, as function of external magnetic field and probe frequency is shown in Fig. 4.11 (a). An onset of anti-crossing feature (a signature of coherent coupling in a hybrid system) between the CCW skyrmion mode and the cavity photons is visible at the degeneracy point where the cavity mode (orange dashed line) would otherwise intersect the dispersion of CCW skyrmion mode (dashed red line taken from Onose et al [129]). The interaction is different compared with the coherent coupling

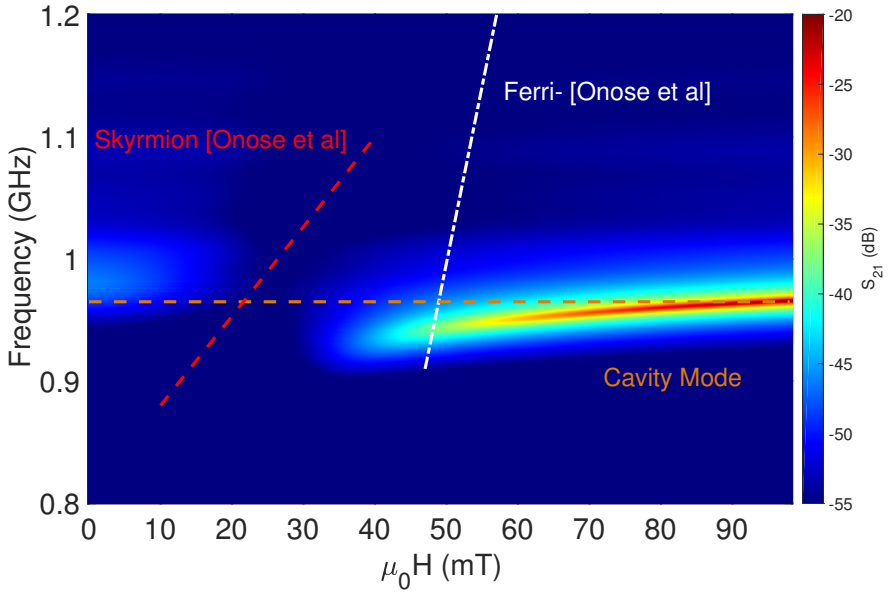

(a)

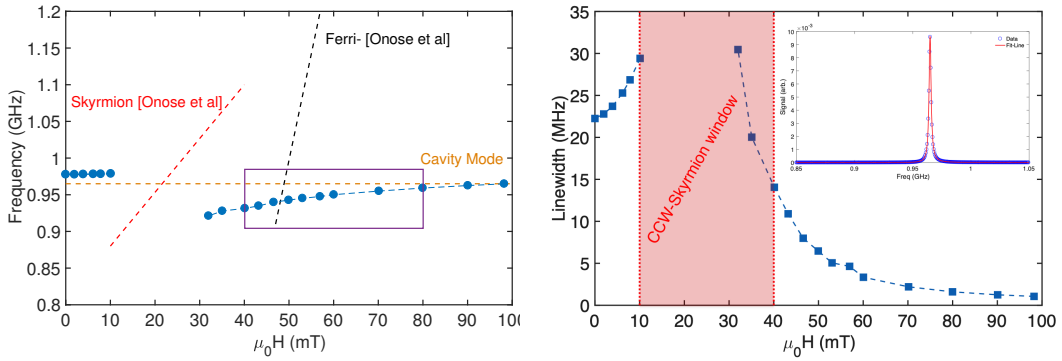

(b) **(c)**

Figure 4.11: (a) The experimentally measured magnitude of the microwave transmission spectra, S_{21}, in single crystal of Cu_2OSeO_3 at 57.5 K. The dashed orange line represents the cavity mode, dashed red line highlights the frequency dependence of counter-clockwise skyrmion mode, and the dotted-dashed white line shows the dispersion of ferrimagnetic state. (b) The resonance peak position plotted from the data in (a), where the box (purple) shows the deviation of the peaks from the cavity mode. (c) Shows the linewidth (full-width-half-maximum) as function of magnetic field extracted by fitting the peaks with a Lorentzian function (inset).

and realisation of a hybrid state between the cavity photons and low-loss magnons (cavity-magnon-polariton) in the field-polarised state as shown earlier. The absorption peaks (line cuts at different magnetic fields from the colour-plot in Fig. 4.11 (a)) were fitted with a Lorentzian function, as shown inset of Fig. 4.11 (c), in or-

der to extract the resonance frequency (peak-position) and the linewidth (full-width half maximum). An important observation from the experimental data is that the cavity mode starts to get influenced from a high magnetic field region ($\approx$ 80 mT), whereas from the phase diagram (in Fig. 4.10 (c)) the skyrmion region lies in the magnetic field window of $\approx$ 10 - 40 mT as highlighted by the purple box in Fig. 4.11 (b). The excitation of the other spin texture modes lies above the frequency of the CCW skyrmion mode and even extending the dispersion of the ferrimagnetic phase (dotted-dashed white line in Fig. 4.11 (a)) from Onose et al study [129] does not help in understanding the cause of the cavity mode deviation at high magnetic field. The extracted linewidth as a function of magnetic field is shown in Fig. 4.11 (c), and as one gets near to the skyrmion window in the magnetic field range the linewidth increases from both sides, i.e from low to high and high to low magnetic field, and it diverges approaching the degeneracy point within the skyrmion window.

In order to quantitatively characterise the observed onset of anti-crossing between CCW skyrmion mode and cavity photons, the magnetic field and frequency-dependent transmission of the cavity and spin-system was numerically modelled using the input-output formalism. The transmission parameter, S_{21} was determined using the following equation (as discussed earlier in Ch. 2):

$$S_{21} = \frac{\sqrt{2\kappa_1\kappa_2}}{i(\omega-\omega_c) - (\kappa_c+\kappa_1+\kappa_2) + \frac{g_{sky}}{i(\omega-\omega_{sky})-\gamma_{sky}}}, \tag{4.14}$$

where ω is the probe frequency, ω_c is the frequency of the primary cavity mode, ω_{sky} is the frequency of CCW skyrmion mode, κ_c is the damping rate of the primary cavity mode, κ_1 (κ_2) is the loss rate between the cavity mode and transmission line to port 1 (port 2), γ_{sky} is damping rate of the CCW skyrmion gyration and g_{sky} is the coupling strength between the cavity mode and the CCW skyrmion mode. The frequency dependence of the CCW skyrmion mode as a function of external magnetic was taken from Onose et al. work (as shown in Fig. 4.10 (b)) [129]. The resonance frequency lies in the proximity of $\approx$ 1 GHz and narrow magnetic field window of $\approx$ 10 - 40 mT, and this was used initially (as can be seen in the inset of Fig. 4.12) to compare the experimental data with the numerical calculation.

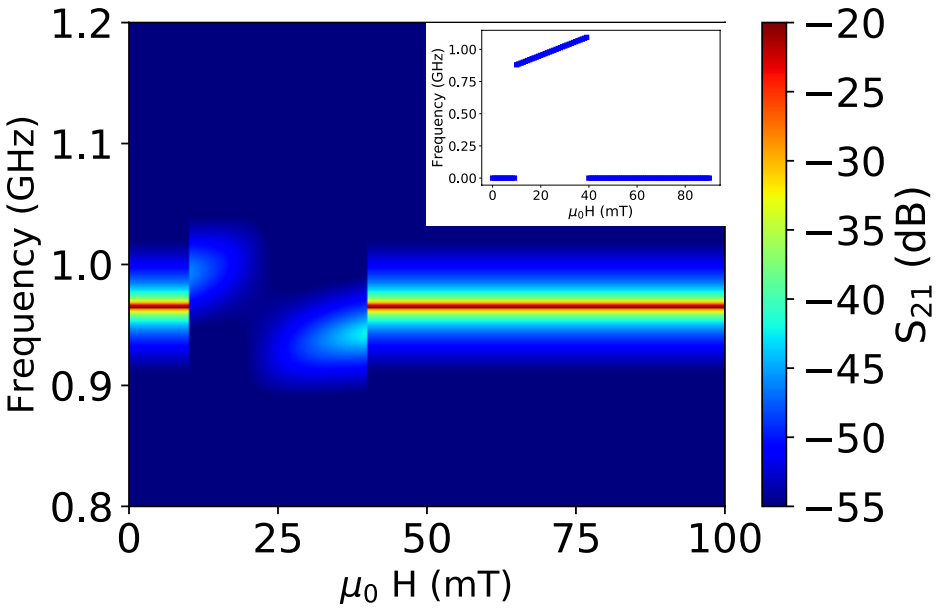

(a)

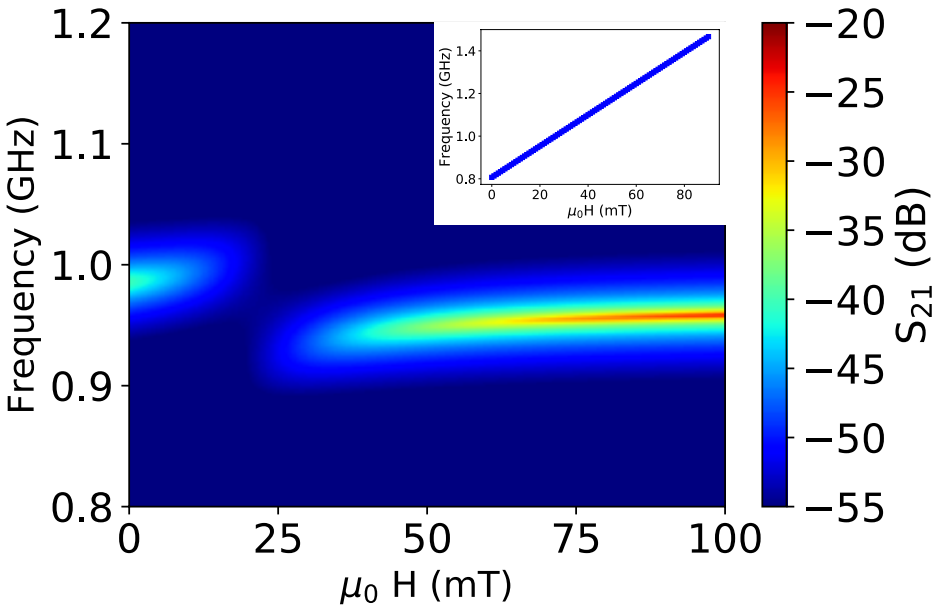

(b)

Figure 4.12: Results of numerical calculation of magnitude of transmission spectra, S_{21}, for comparison with experimental data of cavity photon interaction with the counter-clockwise skyrmion mode at 57.5 K: (a) where the previous experimentally observed frequency dependence of counter-clockwise skyrmion mode (inset) is considered in the calculation, (b) where the numerical calculation qualitatively agrees well with the experimental data in Fig. 4.11 (a) but with different dispersion (inset) compared to the experimentally observed one.

The experimental data in Fig. 4.11 (a) could not be reproduced by considering the reported dispersion of CCW skyrmion mode as shown in Fig. 4.12 (a), where the cavity mode frequency did not shift from a high magnetic field point and also an abrupt transition into skyrmion phase was seen, the two aspects not observed experimentally. Numerical calculations for determining S_{21} were then performed using the frequency dependence shown in the inset of Fig. 4.12 (b). Even though the frequency dependence for the CCW skyrmion mode was not similar to the one reported in the literature, as it extends in magnetic field region outside of skyrmion phase, the feature of the onset of anti-crossing was successfully reproduced as shown in Fig. 4.12 (b). Qualitatively, the experimental data (in Fig. 4.11 (a)) can be directly compared with the numerical calculation (in Fig. 4.12 (b)). The following parameters were extracted from the numerical calculation: $\kappa \approx 1.2$ MHz ($\kappa = \kappa_c + \kappa_1 + \kappa_2$, where $\kappa_c \approx 1$ MHz, $\kappa_1 \approx 0.1$ MHz and $\kappa_2 \approx 0.1$ MHz), $\gamma_{sky} \approx 170$ MHz and $g_{sky} \approx 65$ MHz. This suggests that the CCW skymion mode - cavity photon system does not enter the strong coupling regime as $\kappa < g_{sky} < \gamma_{sky}$, i.e. the coherent coupling rate is less than the damping rate of the skyrmion gyration mode. A recent theoretical study on the coupling of cavity photons (in planar resonator) and gyration modes of magnetic spin textures (vortex and skyrmions) concludes that reaching the strong coupling condition in such a system is quite difficult due to the large damping rate of the gyration modes [130].

In order to confirm that the cavity photons were indeed interacting with the CCW skyrmion mode, microwave transmission experiments were performed outside of the skyrmion phase temperature region. Fig. 4.13 (a) shows the frequency dependence and magnetic field dependence of S_{21} at 53 K (below the ferrimagnetic T_c and the skyrmion window), and Fig. 4.13 (b) shows the S_{21} measured at 59 K (above the T_c and in the paramagentic phase). In both cases, the onset of anti-crossing feature seen in the skyrmion phase (at 57.5 K) disappears, and hence, this verifies that the experimentally observed coupling is indeed between the photons and the CCW skyrmion mode.

The breathing skyrmion mode is excited when the microwave excitation field

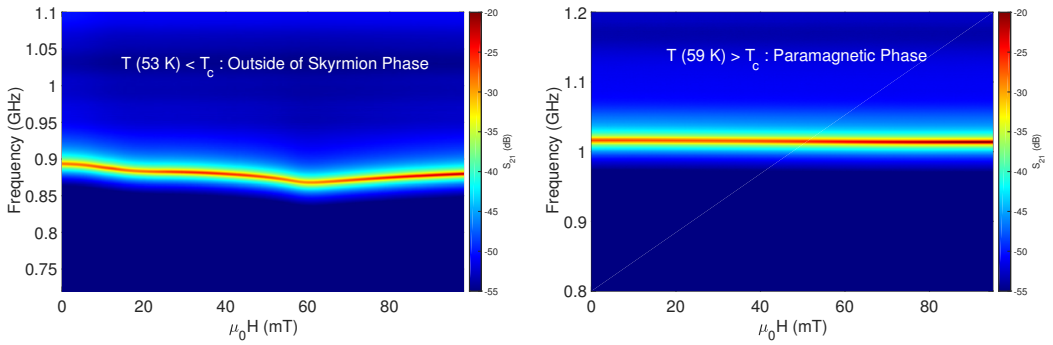

(a) **(b)**

Figure 4.13: The experimentally measured magnitude of the microwave transmission spectra, S_{21}, in single crystal of Cu_2OSeO_3: (a) at 53 K i.e. below the skyrmion phase and (b) at 59 K i.e. above the skyrmion phase as suggested by the magnetic field-temperature phase diagram.

($\mathbf{h}^{\omega}$) is parallel to the external magnetic field ($\mathbf{H}$) as shown earlier in Fig. 4.9 (right panel). Onose et al [129] also reported the very first magnetic resonance of breathing mode in Cu_2OSeO_3 as can be seen in Fig. 4.14 (a). Fig. 4.14 (b) shows the frequency dependence of breathing mode as a function of magnetic field. It can be seen that the excitation of other magnetic phases is suppressed in this configuration ($\mathbf{H} \parallel \mathbf{h}^{\omega}$) and only the breathing mode is excited. The temperature-magnetic field phase diagram (Fig. 4.14 (c)) constructed from the intensity of the observed resonance peaks highlights that the skyrmion phase exists just below Curie temperature (within a $\approx$ 2 K window) and within the magnetic field range of $\approx$ 6 - 24 mT [129]. Another point to note is that the excitation frequency of breathing mode has a negative slope with increasing external magnetic field and it is excited at higher frequencies than the counter-clockwise mode at the same sample temperature of $\approx$ 57.5 K.

The geometrical limitation of the experimental setup of STO resonator and the electromagnet in order to get excitation field of the cavity parallel to the external together with the requirement of higher resonance frequency of the primary cavity mode at 57.5 K meant that the same cavity as in the case of counter-clockwise mode was not used to excite breathing skyrmion mode. Instead, a helical resonator (discussed in more detail in chapter 3) with the resonance frequency of the primary

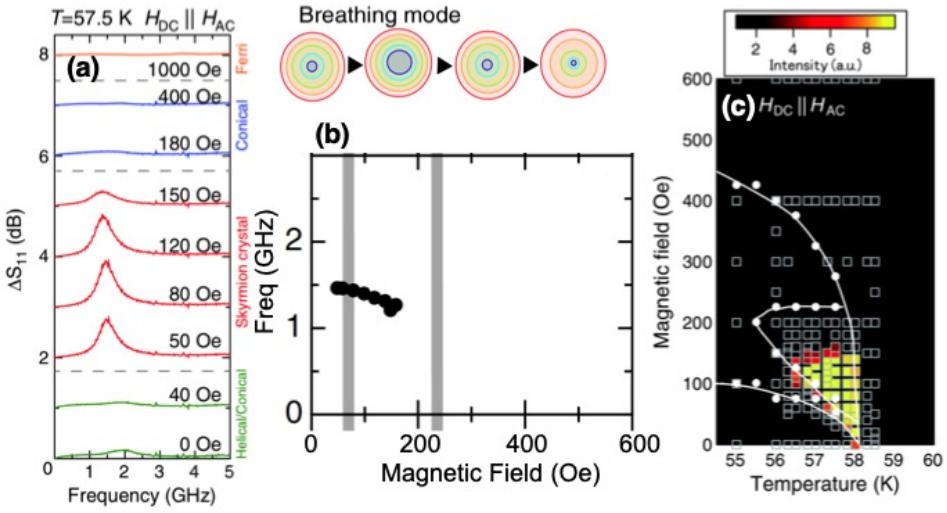

Figure 4.14: (a) Microwave absorption spectra measured (by Onose et al. [129]) for Cu_2OSeO_3 crystal at 57.5 K for different magnetic fields with $\mathbf{H} \parallel \mathbf{h}^{\omega}$ configuration. (b) The frequency dependence of breathing skyrmion mode as a function of external magnetic field. (c) The breathing mode resonance intensity plotted in the magnetic field-temperature phase diagram highlighting the skyrmion window for $\mathbf{H} \parallel \mathbf{h}^{\omega}$ configuration. (a), (b) and (c) are taken from Ref. [129].

mode, $\omega_c \approx 1.42$ GHz was used to experimentally study the interaction of cavity photons with the breathing skyrmion mode in Cu_2OSeO_3.

Figure 4.15 (a) shows the observed microwave transmission spectra (S_{21}) as a function of the probe frequency and external magnetic field in the breathing skyrmion phase at 57. 5 K. In comparison with the coupling of cavity photons and counter-clockwise skyrmion mode, the breathing mode excitation did not show any anti-crossing feature. The primary cavity mode (white line) in the helical resonator in Fig. 4.15 (a) intersects the the dispersion of the breathing mode (red line) as reported by Onose et al. [129] and also the excitation of other phases is suppressed in parallel excitation regime. Hence, the feature of weak-interaction is the excitation of the breathing mode in this experiment and the cavity mode enters in the breathing mode skyrmion phase from high magnetic field point and excites the skyrmion resonance which is dispersive. The scan-cuts taken in the magnetic field skyrmion region at 16 mT and away from the skyrmion region at 35 mT are shown in Fig. 4.15 (a) and (b), respectively. At the high magnetic field region, only the cavity resonance is seen which was fitted with a single Lorentzian peak but in the

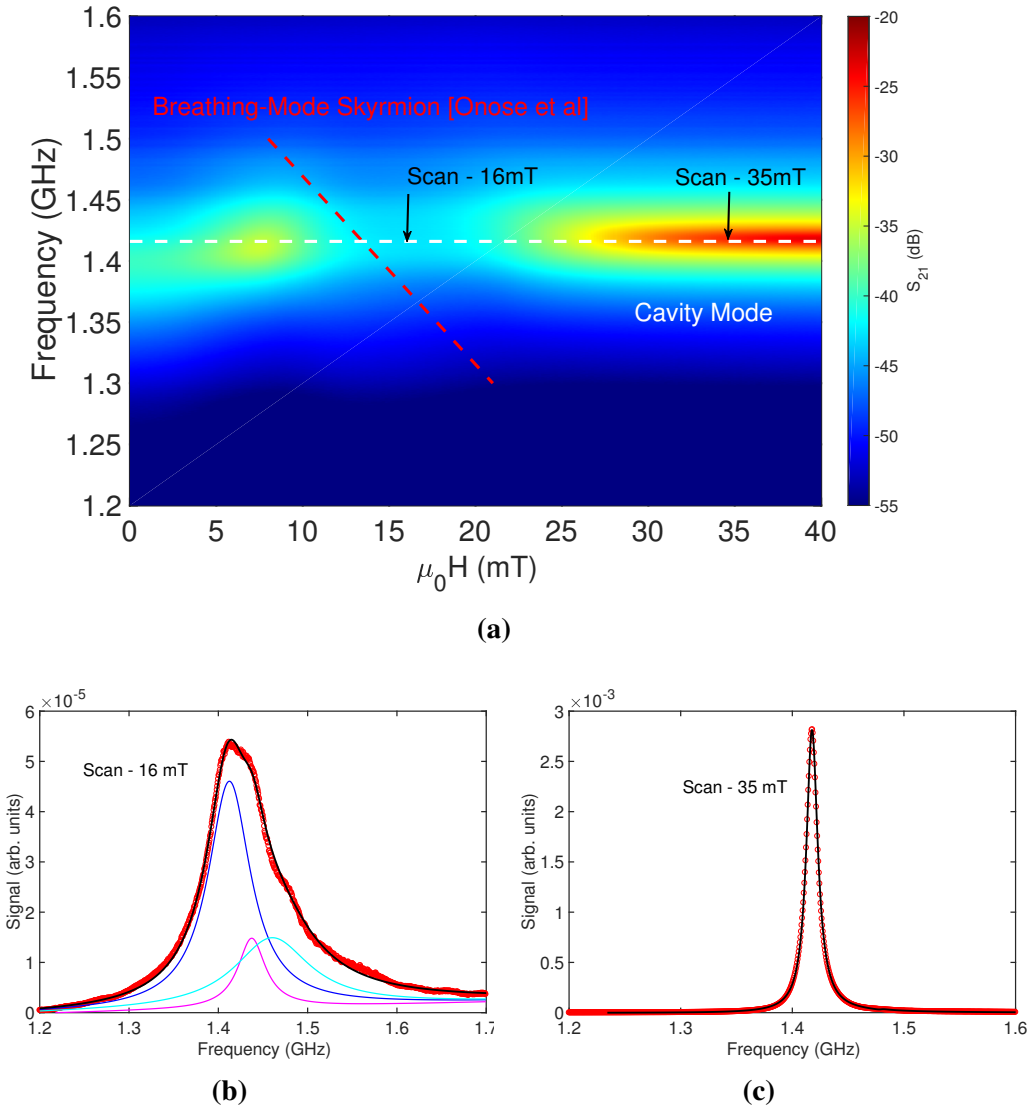

Figure 4.15: Shows (a) the experimental measurement magnitude of the microwave transmission spectra, S_{21}, at 57.5 K in the parallel excitation configuration for the breathing skyrmion mode. The white represents the cavity mode and the red line shows the frequency dependence of breathing mode. (b) The scan-cut taken in the skyrmion magnetic field region of 16 mT, where data (red circles) is fitted by three-Lorentzian peaks. (c) The scan-cut taken outside of the skyrmion region at 35 mT showing the cavity resonance and the data is fitted with a single Lorentzian peak.

skyrmion phase the resonance feature shows a broader signal where multiple peaks were identified which are fitted with multiple Lorentzian peaks and the peak positions and linewidth parameters were extracted. This multi-peak behaviour suggests excitation of higher-order modes of the breathing skyrmion mode which is signifi-

cantly different of the magnetic resonance spectra shown by Onose et al. (Fig. 4.14 (a)), where a single resonance peak is observed for the breathing mode excitation [129].

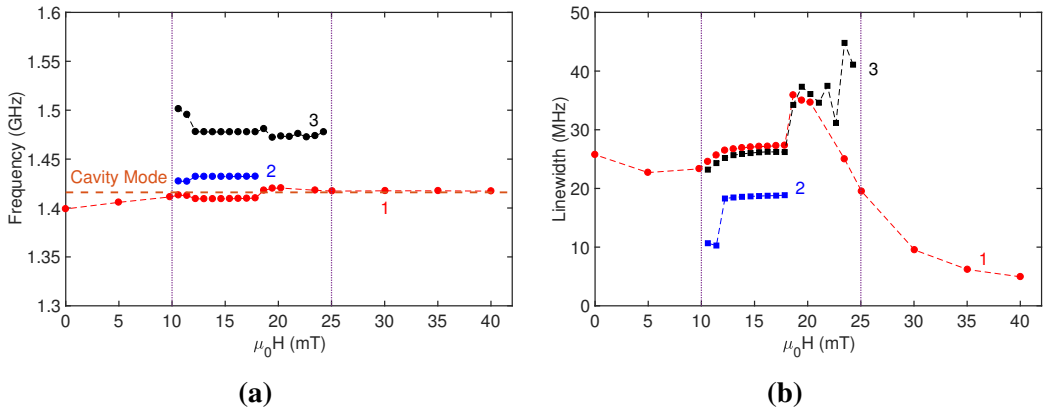

(a) **(b)**

Figure 4.16: (a) Shows the resonance peak position of extracted from the Lorentzian fitting of the breathing mode resonance. Three different modes are identified within the skyrmion magnetic field region at 57.5 K. (b) The extracted linewidth (full-width-half-maximum) of three different modes observed for the breathing mode excitation.

Figure 4.16 (a) and (b) show the frequency and linewidth dependence of the observed multiple peaks in the breathing mode as a function of external magnetic field, respectively. Three different peaks are identified in the skyrmion phase and are discussed here qualitatively. The primary cavity mode is perturbed when the system enters the skrymion phase, and as the excitation was in a parallel regime, this condition rules out observing resonance of other magnetic phases in the sample, and these modes can be attributed to higher-order excitation modes of breathing skyrmion mode. The linewidth of cavity resonance, as can be seen in 4.16 (b), increases as the magnetic field approaches the skyrmion phase. Qualitatively, the combined linewidth of the three resonance peaks can be compared to the linewidth of the spectra observed by Onose et al. [129]. Therefore, it shows that the excitation by the helical resonator is sensitive to resolve the higher-order modes of skyrmion resonance, which might not be possible by a co-planar waveguide technique, but further theoretical insight is required to confirm that the experimentally seen features here are indeed the higher-order modes of the breathing mode.

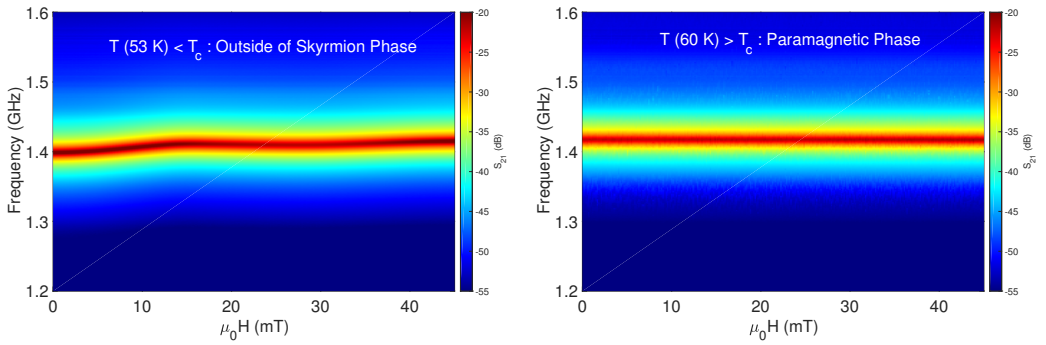

Figure 4.17: The experimentally measured magnitude of the microwave transmission spectra, S_{21}, in single crystal of Cu_2OSeO_3: (a) at 53 K i.e. below the skyrmion phase and (b) at 60 K i.e. above the skyrmion phase. In both cases the primary cavity mode remains unperturbed as function of the external magnetic field.

Further microwave transmission experiments in the parallel excitation configuration were carried outside of the skyrmion phase but below the ferrimagnetic T_c and in the paramagnetic phase. Fig. 4.17 (a) and (b) show the dependence of S_{21} as a function of probe frequency and external magnetic field at 53 K (outside of skyrmion phase) and at 60 K (in the paramagnetic phase). In both cases, the resonance feature seen at 57.5 K (in the skyrmion phase) disappears and the cavity resonance remains unperturbed. Experimentally, this confirms that the resonance at 57.5 K is indeed the excitation of breathing skyrmion mode, so the cavity photons in the helical resonator interact with breathing mode, and the resonator possesses higher sensitivity than excitation by co-planar waveguide where different modes within breathing mode were resolved.

4.5 Conclusion

In conclusion, the coupling of cavity photons and excitations in magnetic materials was mainly studied in the field-polarised regime i.e. collinear spin phase, for example most literature was focused on yitrium iron garnet (yig) sample. In this study, a magnetic sample of copper -oxoselenite (Cu_2OSeO_3) possessing different non-collinear and collinear magnetic phases (helical, conical, skyrmion and field-polarised) was investigated for the first time to study the interaction of cavity pho-

tons with the excitations of multiple magnetic phases in the system. Three different microwave cavity resonators (Bruker MD5, STO and helical resonators) were used to carry the microwave excitation experiments in the parallel and perpendicular configuration of oscillating microwave magnetic field to the external magnetic field.

The Bruker MD5 cavity was used to study the coupling of photons to magnons in the field polarised, helical and conical magnetic phases. Strong-coupling regime was achieved between the ferrimagnetic magnon mode and multiple cavity modes in the field-polarised case, with the cooperativity reaching 3600 for the hybridised state of primary cavity mode and the magnon mode. In the non-collinear conical phase, dispersive coupling was observed between the fundamental helimagnon mode and the cavity modes, and this behaviour was used as a magnetic sensing probe for phase transition in the system to map out the phase diagram. A Purcell-effect regime was detected with a normal-mode splitting feature between the cavity photons and high-order helimagnons in the non-collinear helical phase.

The STO and helical resonators were used to probe the interaction of microwave photons with the resonant skrymion counter-clockwise and breathing modes, respectively. In the case of the counter-clockwise mode, the very first experimental observation of an onset of anti-crossing feature is reported here, where the coupling strength was found to be ≈ 3 times smaller than the loss-rate of skyrmions, hence the system does not enter the strong coupling regime. In the parallel excitation configuration, the breathing mode resonance was seen and higher-order modes were distinguished.

Chapter 5

Spin Dynamics in van der Waals Single Crystal

Two-dimensional (2D) van der Waals (vdWs) single crystals, belonging to the family of lamellar ternary chalcogenides (i.e. $Cr_2Ge_2Te_6$ and $Cr_2Si_2Te_6$) and chromium halides (i.e. CrI_3 and $CrBr_3$), have recently attracted a great deal of interest due to the presence of long-range magnetic order in the 2D limit [131, 132, 133, 134]. The presence of magnetism in the 2D state has a potential to open new avenues in the field of spintronics leading to new magneto-optical and magneto-electric applications[135, 136]. According to the Mermin-Wagner theorem [137], thermal fluctuations in 2D systems at finite temperatures can restrain the long-range magnetic order, however due to the presence of large magnetocrystalline anisotropy in these layered systems the magnetic order remains dominant down to a few layers.

$Cr_2Ge_2Te_6$ (CGT) has been a subject of vast experimental studies over the past few years. Gong et al. discovered the intrinsic ferromagnetism down to atomic bilayers of CGT using the magneto-optical technique and showed a significant control between paramagnetic to ferromagnetic phase transition temperature with application of very small magnetic fields [134]. For CGT with only few layers (≈ 3.5 nm thickness of crystalline flakes), Wang et al. demonstrated the control of magnetism by an electric field, showing a possibility for new applications in 2D vdWs magnets [138]. Liu et al. reported an anisotropic magnetocaloric effect associated with the critical behaviour of CGT and provide evidence of 2D Ising-like ferromagnetism,

which is preserved in few-layer devices [139]. There still remains an ambiguity in the type of magnetic interaction in CGT, as experimentally, Heisenberg-like ferromagnetism is reported [134], but other reports looking at the critical exponents in CGT predict 2D Ising-like ferromagnetism [140, 141].

CGT has been proposed as a potential substrate for topological insulators in order to realise the quantum anomalous hall effect [142]. Upon to the point of the experiments performed in this chapter, there has been only one brief report of determination of the uniaxial magnetic anisotropy in CGT by ferromagnetic resonance (FMR) [143], while recent experiments rely on probing the sample by means of magneto-optical, magnetometry and transport techniques. Understanding the magnetisation dynamics by FMR is beneficial as it measures the uniform-mode excitations of spin-waves with $k \approx 0$ [144]. The FMR experiment allows to determine the magnetic anisotropies in the system, the spectroscopic splitting g-factor, and addtionally it can provide information on the relative orbital contribution to the magnetic moment [145]. Therefore, it is significant to better understand the magnetisation dynamics in bulk CGT in order to unfold the full potential of these layered vdWs systems in the field of spintronics.

In this chapter, the broadband FMR results in CGT in the temperature range of 60 K - 2 K, with the external magnetic field applied along the in-plane (ab-plane) and out-of-plane (c-axis) orientations are presented. The extracted value of the uniaxial magnetocrystalline anisotropy constant, K_{u}, was found to be temperature-dependent. The scaling of magnetic anisotropy constant and saturation magnetisation as a function of temperature was observed to deviate from the theoretical prediction by the Callen-Callen power law. The determined g-factor in CGT was found to be anisotropic for the different crystallographic directions. Domain-mode resonance phenomenon below the saturation field along the ab-plane was observed and this indicated presence of multiple domain structures in CGT. Finally, based on findings of the g-factor temperature dependence, X-ray Magnetic Circular Dichroism (XMCD) experiment was performed to probe the anisotropy in the orbital moment of bulk CGT.

5.1 Chromium-Tellurogermanate Sample

CGT[1] is a layered 2D ferromagnetic semiconductor with vdWs coupling between the adjacent layers, and bulk CGT has a trigonal crystal structure belonging to the centrosymmetric $R\bar{3}$ space group [146]. The crystal structure is shown in Fig. 5.1, where each unit cell contains three layers stacked in an ABC sequence and with a gap between each layer corresponding to the vdWs gap. This vdWs gap makes CGT similar to graphite where it can also be exfoliated down to a few layers.

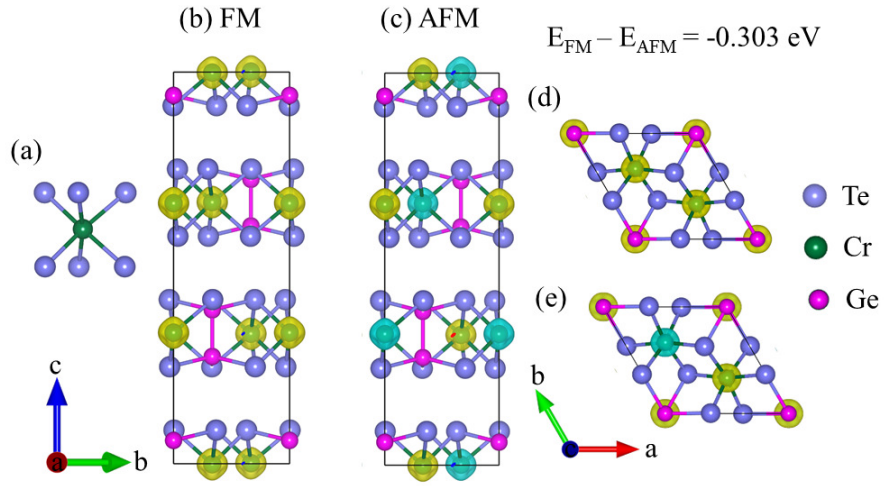

Figure 5.1: (a) Side-view of the local structure of bulk $CrGeTe_3$, showing that one Cr atom surrounded by six Te atoms in a octahedral configuration. (b) and (d) show the side and top view of spin polarised charge densities of CGT in the FM configuration, respectively, and (c) and (e) the same in AFM configuration. The yellow color and green color represent the charge density of spin up and down, respectively. The gap in the unit cell between the Te atoms represents the vdWs gap and it is approximately 0.33 nm [147].

In bulk CGT, the magnetic order originates from the Cr-Cr exchange and 90° Cr-Te-Cr super-exchange interactions, where the ferromagnetic (FM) state is found to be the ground state, as the anti-ferromagnetic (AFM) configuration is 0.303 eV per unit cell higher in energy that the FM state [147]. The Curie temperature of the

[1]The single crystal samples of CGT were grown and synthesised by the direct vapor transport method and the growth procedure was done by Dr. I. Verzhbitskiy from National University of Singapore. More information about sample can be found in appendix A.

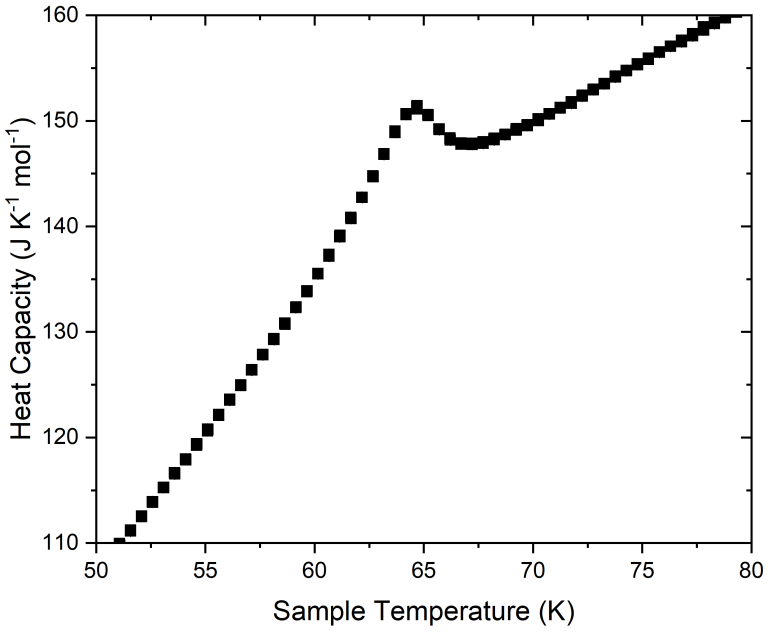

Figure 5.2: Heat capacity of a CGT sample measured by thermal relaxation calorimetry. The anomaly in the heat capacity associated with the paramagnetic to ferromagnetic transition indicates a Curie temperature of 64.7 ± 0.5 K.

CGT sample was determined to be $T_c = 64.7 \pm 0.5$ K via a characteristic peak in the heat capacity associated with magnetic ordering (Fig. 5.2). The cusp in the heat capacity data as a function of sample temperature corresponds to collinear magnetic ordering in CGT, as reported elsewhere [141].

The magnetisation of the CGT sample was measured[2] below the Curie temperature for fields along the in-plane (ab-plane) and out-of-plane (c-axis) directions as shown in Fig. 5.3 (a) and (b), yielding respective saturation magnetisations of 2.68 ± 0.06 and 2.78 ± 0.06 μ_B per Cr atom at 2 K (Fig. 5.3 (c)). The observed magnetisation-external magnetic field (*M-H*) curves confirmed that bulk CGT has easy magnetic axis in the out-of-plane (i.e. along the c-axis) and hard axis in the in-plane (ab-plane) configuration.

[2]The magnetometry measurements were performed with the help of Dr. D. M. Arroo.

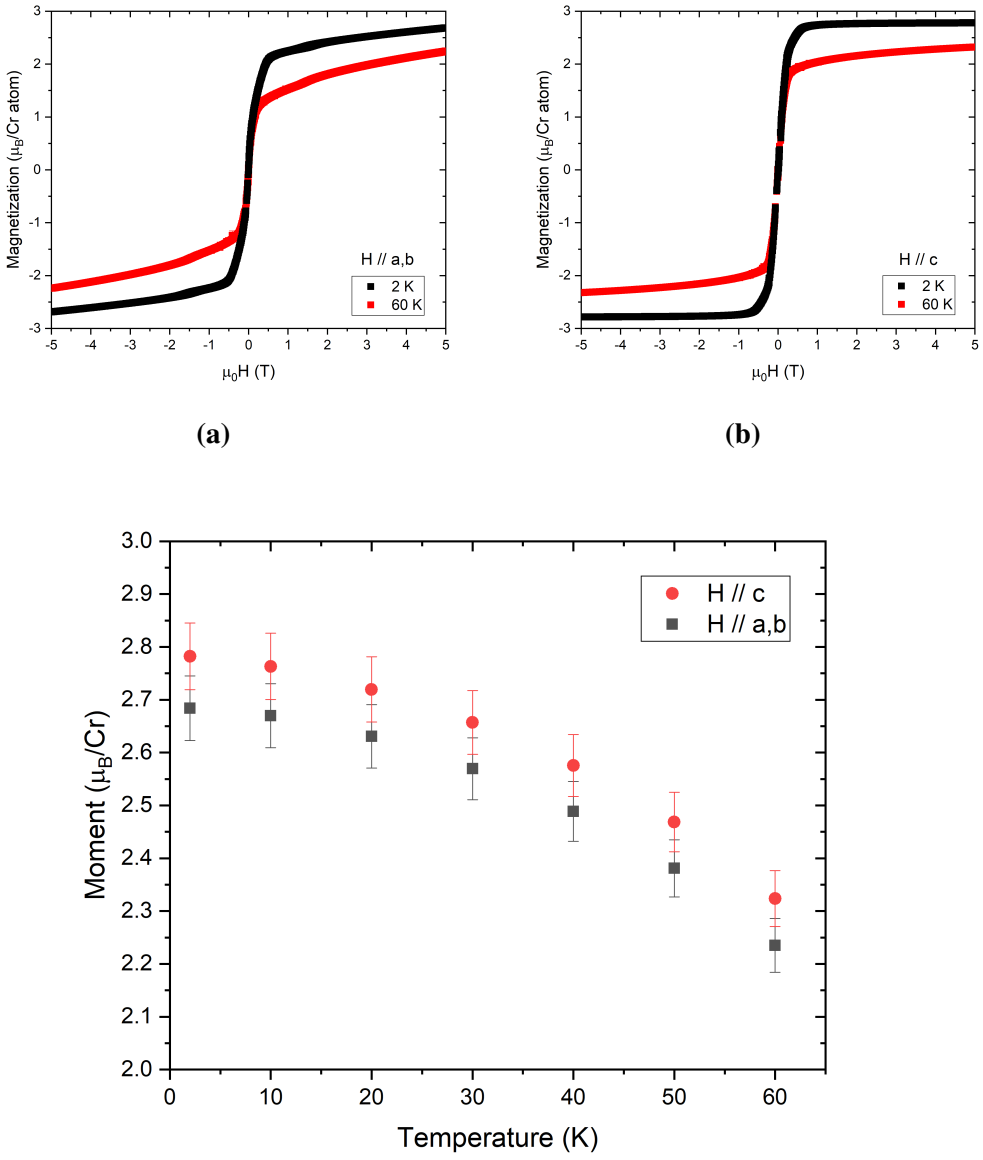

Figure 5.3: Magnetisation data for CGT measured via vibrating sample magnetometry carried out at temperatures from 2 K to 60 K. (a) Magnetisation curves with the field applied along the in-plane direction. (b) Magnetisation curves with the field applied along the out-of-plane direction. (c) Magnetisation with an applied field of 5 T as a function of temperature.

5.2 Resonance Spectra

The broadband FMR, for externally applied magnetic fields along the in-plane and out-of-plane directions for 60 K, 30 K, and 2 K are shown in Fig. 5.4. The inset shows an exemplary experimental resonance spectra. The resonance is described by the derivation of the dynamic susceptibility from the Landau-Lifshitz and Gilbert equation, and hence it was analysed by fitting a linear combination of symmetric and anti-symmetric Lorentzian functions in order to determine the resonance field, H_r (i.e. peak position)[148], as discussed earlier in chapter 2.

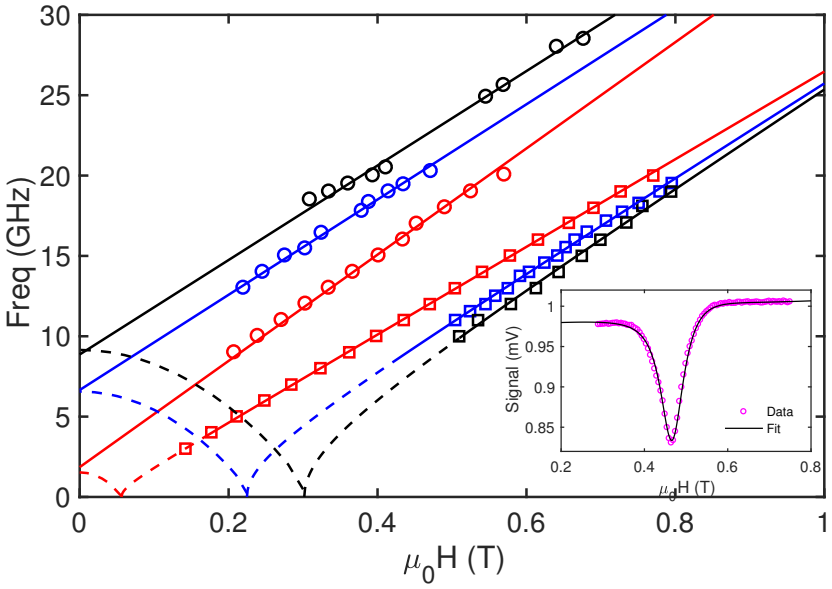

Figure 5.4: The inset shows the experimental resonance spectra with a Lorentzian line shape (black line). Main plot shows frequency dependence of resonance field at 60 K (red), 30K (blue) and 2 K (black), along the in-plane (squares data points) and out-of-plane (circle data points) orientations. The solid lines represents the Kittel fitting for both orientations giving straight line fit along the c-axis (fitted with Eq. 5.4) and square-root dependence along ab-plane (fitted with Eq. 5.3) i.e. easy and hard axis, respectively. The dotted line along in-plane orientation show an expected spectrum of frequency dependence for a single domain case.

The frequency dependence of H_r exhibited the typical characteristic of magnetisation dynamics in a ferromagnet with easy and hard magnetic axis. The easy axis in this case is along the c-axis (out-of-plane), which showed a linear frequency dependence with a non-zero y-intercept corresponding to the anisotropy field. The ab-plane (in-plane) resonance spectra showed a non-linear frequency dependence

with the x-intercept increasing in value as the temperature was decreased from 60 K to 2 K, exhibiting an increase in the uniaxial magnetocrystalline anisotropy. The dotted lines show the expected resonance spectra of a uniform ferromagnetic resonance in single domain crystals. An important observation in the extracted FMR Kittel relations, is the difference in slope for in-plane and out-of-plane orientations. Additionally, the slope for the two orientations showed a temperature dependence. This suggests that the spectroscopic g-factor is not isotropic for CGT (discussed in more detail below).

The Smit-Beljers-Suhl approach (as shown earlier in chapter 2) was used to derive the fitting equations describing the dependence of the resonance frequency on the external magnetic field, which were then used to fit the experimental data along the in-plane and out-of-plane directions in Fig. 5.4. The angular dependence of free energy density, F, for the CGT system in-plane dimensions of 2 x 1.5 mm and thickness of 0.3 mm, i.e. in the out-of-plane direction) is considered as

$$F = -\mu_0 \mathbf{M}\cdot\mathbf{H} + \mu_0(\mathbf{M}\cdot\mathbf{n})^2 - K_\mathrm{u}(\mathbf{M}\cdot\frac{\mathbf{z}}{M_\mathrm{s}})^2, \tag{5.1}$$

where $\mathbf{H}$ and $\mathbf{M}$ are the external magnetic field and magnetisation vectors, respectively. The first term in Eq. 5.1 is the Zeeman energy, the second term is the demagnetisation energy and the third term is the uniaxial magnetic anisotropy term, with K_u, the magnetocrystalline anisotropy constant, M_s, the saturation magnetisation, and $\mathbf{n}$ and $\mathbf{z}$ are the unit vectors normal to the surface of the sample and orientated along the easy axis (c-axis), respectively. $\mathbf{H}$ and $\mathbf{M}$ are functionally dependent on $\theta_\mathrm{H/M}$ and $\phi_\mathrm{H/M}$, which are the polar (accounted from normal to the rectangular sample platelet ab-plane) and azimuthal (in-plane) angles, respectively. The double derivatives approach (as shown in chapter 2) of the magnetic free energy with respect to the polar and azimuthal angles (the azimuthal angles in the CGT system can be set to $\phi_\mathrm{H/M} = 0$, as the in-plane magnetocrystalline anisotropy energy is negligible) was then used to analytically calculate the resonance frequency, $\omega = 2\pi f$. Solving for the perpendicular anisotropy case ($\mathbf{n} = \mathbf{z}$, along the easy axis i.e. parallel to out of plane c-axis), one arrives at the general Kittel relation for arbitrary

polar angles of the external magnetic field with respect to the easy axis of the magnetisation, which reads

$$\left(\frac{\omega}{\gamma}\right)^2 = [H_r\cos(\theta_H-\theta_M)-4\pi M_{eff}\cos^2(\theta_M)] \times [H_r\cos(\theta_H-\theta_M)-4\pi M_{eff}\cos(2\theta_M)] \tag{5.2}$$

where γ, is the gyromagnetic ratio, H_r is the ferromagnetic resonance field, $4\pi M_{eff} = 4\pi M_s - H_u$ is the effective demagnetisation field and $H_u = 2K_u/\mu_0 M_s$, the perpendicular anisotropy field. The Kittel equations for the in-plane ($\|$) and perpendicular ($\perp$) orientations were determined by setting $\theta_M = \theta_H$ in a saturated state, and are given by

$$\omega_{(\|)} = \gamma\sqrt{H_r(H_r+4\pi M_{eff})} \ , \tag{5.3}$$

$$\omega_{(\perp)} = \gamma(H_r-4\pi M_{eff}) \ . \tag{5.4}$$

5.3 Anisotropy Energy

The temperature dependence of the out-of-plane uniaxial magnetocrysatlline anisotropy constant, K_u, is shown in Fig. 5.5 (a). This was determined from the least-square fitting of equations 5.3 and 5.4 to the frequency-dependent FMR spectra, with spectroscopic g-factor (contained in $\gamma = g\mu_B/\hbar$) and M_{eff} as fitting parameters. A positive sign convention is used, where $K_u > 0$ favors perpendicular magnetic anisotropy. K_u was found to be in the range of $(0.77-3.95)\times 10^5$ erg/cm^3 from 2 K to 60 K, which confirmed that the magnetic easy axis in CGT is along the c-axis as seen by the magnetometry data and previous experimental observations [143, 146]. The reported magnetocrystalline anisotropy energies for other similar layered 2D magnets are $K_u = 1.46\times 10^7$ erg/cm^3 at 4 K and $K_u = 3.1\times 10^6$ erg/cm^3 at 1.5 K, for Fe_3GeTe_2 [150] and CrI_3 [151], respectively. CGT is found to be less anisotropic then these systems whereas the ferromagnetic T_c of CGT is close to that of CrI_3 ($\sim$ 61 K) and Fe_3GeTe_2 possesses high transition temperature ($\sim$ 223 K).

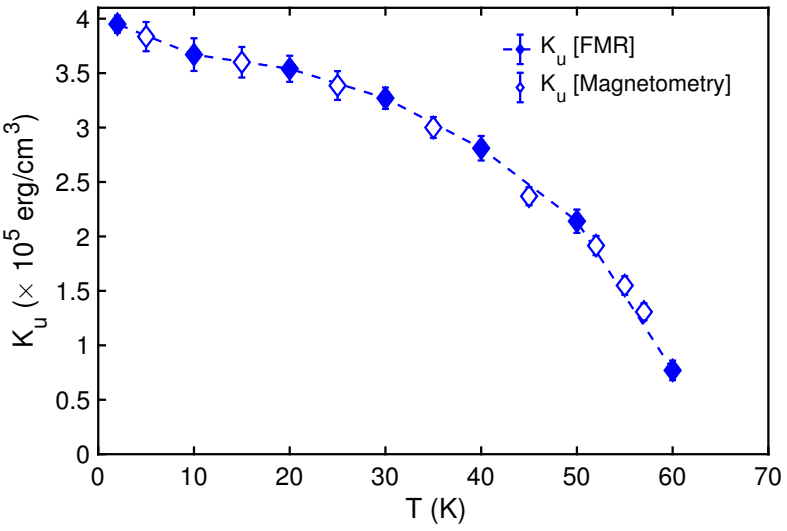

(a)

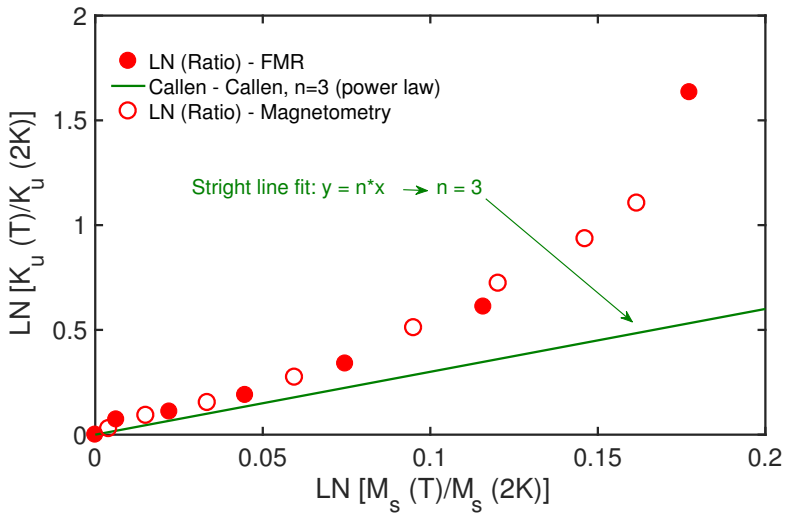

(b)

Figure 5.5: (a) Temperature dependence of uniaxial magnetocrystalline anisotropy constant, K_u, where the filled points are extracted from the FMR data as discussed in the main text and the non-filled points are extracted from the magnetometry measurements [149]. (b) The ratio $K_u(T)/K_u(2\text{ K})$ is compared with the ratio $[M_s(T)/M_s(2\text{ K})]$ in the absolute value of the logarithm scale. A solid line with the exponent, n = 3, is plotted to highlight that the experimental data does not follow the Callen-Callen behaviour.

At 2 K, the anisotropy energy value corresponds to 0.24 meV per unit cell of CGT, which is six times smaller than the value, 1.4 meV per unit cell, obtained from

the DFT calculations[3]. The difference in the experimental and calculated magnetic anisotropy energy can arise as (i) the DFT calculation performed for 0 K, (ii) the structure model used in the calculation is considered to be a defect-free system (the unit cell shown in Fig. 5.1).

In Fig. 5.5 (b), the reduced anisotropy constant, $K_u(T)/K_u(2\,\mathrm{K})$, and the reduced magnetisation, $M_s(T)/M_s(2\,\mathrm{K})$, at different temperatures are shown for the CGT single crystal. The theory of the temperature dependence of magnetic anisotropies was developed by Callen and Callen, and others[152, 153, 154]. It predicts that the magnetocrystalline anisotropy constant as a function of temperature for uniaxial and cubic systems distinctly differs depending on the crystal symmetry and on the degree of correlations between the direction of neighbouring spins. The well-known Callen-Callen power law based on the single-ion anisotropy model relates the temperature dependence of K_u to M_s in the low temperature limit ($T << T_c$) as

$$\frac{K_u(T)}{K_u(0)} = \left[\frac{M_s(T)}{M_s(0)}\right]^n , \tag{5.5}$$

where the exponent, $n = l(l+1)/2$, depends on the crystal symmetry and degree of correlations between adjacent spins, and l being the order of spherical harmonics and it describes the angular dependence of the local anisotropy. In the case of uniaxial anisotropy, the exponent is predicted to be $n = 3$ and it suggests a single-ion origin of magnetic anisotropy.

An unexpected behaviour of the scaling between the temperature dependence of the anisotropy constant and magnetisation was found in hexagonal CGT. This can be seen in Fig. 5.5 (b), where the experimental data departs from the trend of a straight line (plotted in logarithmic scale) with a slope of $n = 3$, predicted by the Callen-Callen power law for uniaxial systems. In simple ferromagnetic systems such as ultrathin Fe films [155], the Callen-Callen power law for uniaxial anisotropy has been experimentally verified, across the whole temperature range below T_c, with an exponent $n = 2.9$, and it is considered as a good model for

[3]The DFT calculations were performed by H. Cheng.

ferromagnets with localised moments. In the past, deviations from the expected scaling exponent of $n = 3$ have been reported in complex systems containing a non-magnetic element with a large spin-orbit coupling, which can contribute to magnetic anisotropy without having a significant effect on other magnetic properties [156, 157, 158]. In highly anisotropic barium ferrite systems, K_u was found to be linearly proportional to M_s, clearly inconsistent from the theoretical predictions [159]. The departure from the Callen-Callen theory for these reported systems is suggested due to the violation of simple assumptions considered in the theory[160], (i) magnetisation origin in the material coming from single-ions with localised magnetic moments, (ii) spin-orbit coupling being regarded as a small perturbation to the exchange coupling and (iii) temperature dependence of anisotropy and magnetisation having the same origin. Recent first principles calculations in CGT predict the interplay between single-ion anisotropy and Kitaev interaction [161]. They are found to be induced by the off-site spin-orbit coupling of the heavy ligand, i.e. Te atoms. Another recent study [162], investigating the origin of magnetic anisotropy in layered ferromagnetic Cr compounds, suggests that an additional magnetic exchange anisotropy induced by the spin-orbit coupling from the ligand (Te) p-orbital through superexchange mechanism plays a crucial role in determining the magnetocrystalline anisotropy in CGT and other layered systems such as CrI_3 and $CrSiTe_3$. Hence, CGT is a complex magnetic system with no simple correlation between the thermal behaviour of anisotropy and magnetisation.

5.4 Spectroscopic g-factor

The temperature dependence of the spectroscopic g-factor for the in-plane (ab-plane) and out-of-plane (c-axis) orientations, can be seen in Fig. 5.6. There is contrasting behaviour in the temperature dependence of g-factor, where g increases with decreasing temperature in the in-plane (hard-axis) direction, and it decreases in the out-of-plane (easy-axis) direction as the temperature decreases. At 2 K, $g_{\parallel} = 2.18 \pm 0.02$ (ab-plane) and $g_{\perp} = 2.10 \pm 0.01$ (c-axis), indicating that the g-factor is anisotropic in CGT and shows a crossing between 20 K and 30 K. The

g-factor was determined by extracting the proportionality of the gyromagnetic ratio in Eqs. (5.3) and (5.4), given by $\gamma = g\mu_B/\hbar$, where μ_B is the Bohr magneton and $\hbar$ is the reduced PlanckFLs constant. Determining a value of g is important since one can find the relative spin and orbital moments of a material by using the well-known relation [163]

$$\frac{\mu_L}{\mu_S} = \frac{g-2}{2} \quad , \tag{5.6}$$

where μ_L is the orbital moment per spin and $\mu_S = \mu_B$ is the spin moment. The deviation of the spectrocopic factor from the electron's g-factor of $g = 2$ suggests an orbital contribution to the magnetisation [164].

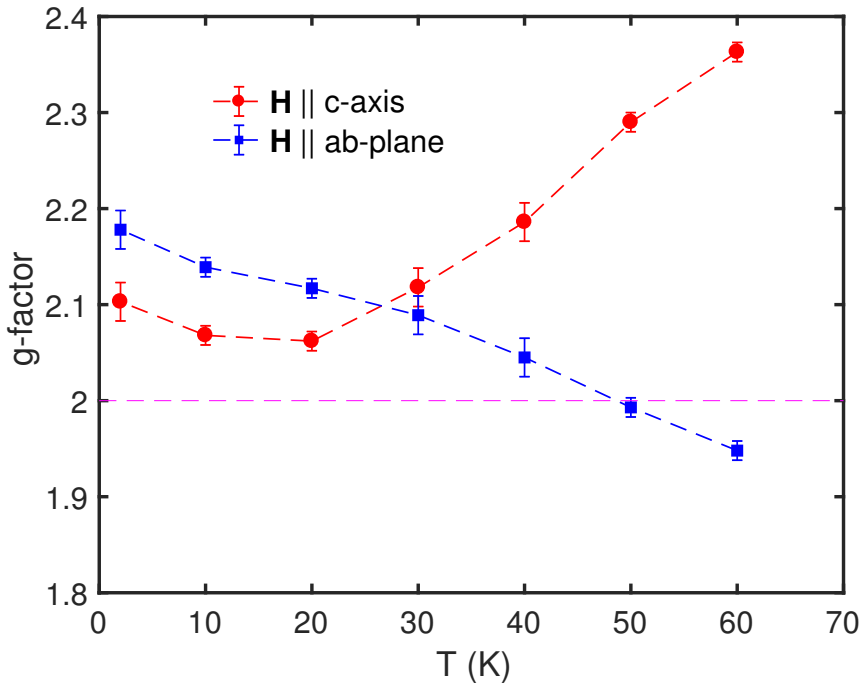

Figure 5.6: Temperature dependence of the spectroscopic g-factor with external magnetic field along the c-axis (easy-axis, red circles) and the ab-plane (hard-axis, blue squares). The dashed horizontal line (magenta) at $g = 2$ indicates a case of pure spin magnetism where the orbital moment is completely quenched.

The g value of the free electron case is considered in systems where the orbital moment is assumed to be nearly completely quenched due to the high symmetry of the bulk crystals, and hence magnetism in such systems is described in terms of pure spin magnetism. The non-spherical charge distribution in the d-shells can

prevent the complete quenching of the orbital momentum [165], i.e. $L_z \neq 0$. An orbital moment of 8 % and 5 % for μ_L/μ_S along the in-plane and out-of-plane orientations, respectively, was found in CGT at 2 K. The small orbital moment anisotropy could be explained by the presence of the spin-orbit interaction from the d-orbitals of the Cr atoms as well as the off-site spin-orbit coupling of p-orbitals of Te atoms, giving g a tensor character i.e. dependence on the crystallographic directions. The g-factor extraction from the FMR experiment here only gives a relative insight into the orbital moment contribution to the magnetism in CGT. One can determine the orbital moment, μ_L, and its anisotropy from the x-ray magnetic circular dichroism (XMCD) experiments at synchrotron facilities in order to further improve the understanding of orbital magnetism in these layered van der Waals magnetic systems[62, 166, 167]. In fact, the study referenced previously [162] looking into the origin of magnetic anisotropy in layered 2D systems also carries out an initial XMCD investigation of Cr $L_{2,3}$-edge in CGT at 20 K. They report a sizable anisotropy in the orbital angular momentum (i.e. related to the orbital moment), where $L_c = -0.045$, $L_{ab} = -0.052$ and $\Delta L = 0.007$. This work complemented the results of g-factor anisotropy obtained in the FMR spectroscopy experiment, where a deviation from $g = 2$ confirmed the presence of orbital angular momentum in CGT and based on these findings beam-time was acquired at the Diamond Light Source, where a detailed XMCD study of CGT was carried out as discussed in more detail below.

5.5 Presence of Multidomains

In Fig. 5.7, the temperature evolution from 60 K to 2 K of the frequency-dependent FMR spectrum in the in-plane (hard-axis) orientation is shown. The red arrows indicate the saturation field points for the CGT system, where a transition from the multidomain magnetic states to a single domain state occurs in the sample[168]. At 60K, there is no sign of domain-mode resonance but as the temperature decreases, the strength of the perpendicular uniaxial magnetic anisotropy increases, and the multiple domain-mode resonances (dotted white lines) appear. Qualitatively, this

shows the presence of multi-domain structures in bulk CGT [169]. The co-planar ferromagnetic resonance setup used in this experiment is sensitive to observe the resonance of these domain structures. The minimum feature of the resonance frequency (red arrow) increases with decreasing temperature. This type of feature is markedly different for samples with a single magnetic domain state[170], where the frequency-dependent resonance spectra has a x-intercept along the hard axis of magnetisation.

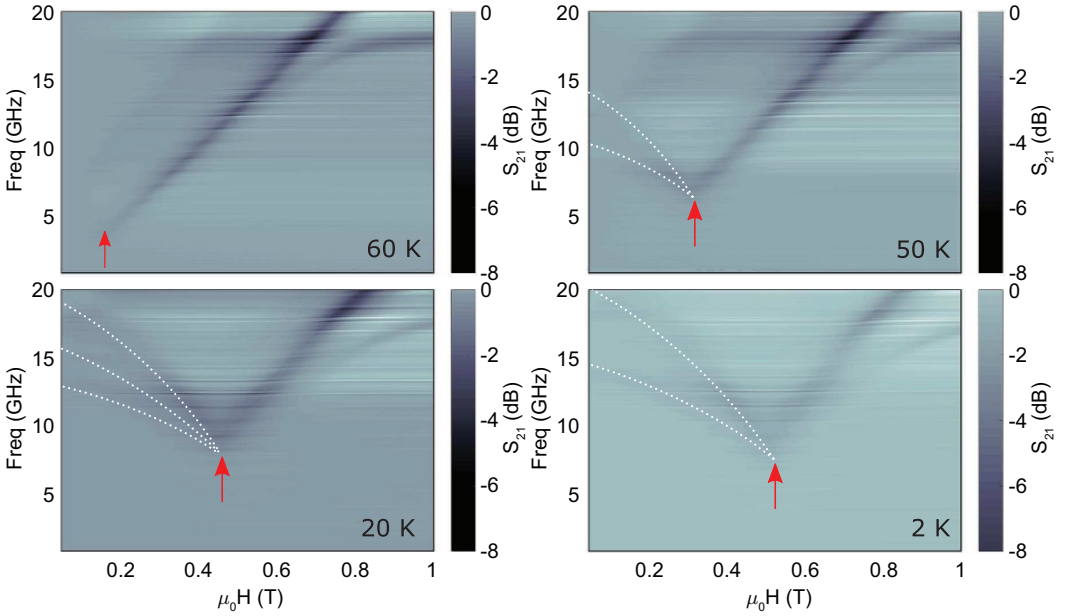

Figure 5.7: Temperature evolution of the frequency-dependent ferromagnetic resonance spectra (in-plane orientation) from 60 K to 2 K. The red arrow indicates the saturation field point in the system where the system goes from multidomain to single domain state. The dotted white lines do not represent any fittings and are used only for guidance.

The *M-H* curves in Fig. 5.3 (a) & (b) show no hysteresis behaviour, but this does not reflect signatures of a single domain system below the saturation state for CGT. The remanent magnetisation at zero external magnetic field does not have any net magnetisation, indicating magnetic moment cancellation due to multi-domain states with up-and-down flux closures. This seems to be common for layered van der Waals magnets i.e. exhibiting a soft magnetic behaviour of a linear *M-H* curve before saturation [171, 172]. The experimental evidence of the presence of multiple magnetic domain structures in bulk CGT along the in-plane sample orientation

has been confirmed using magnetic force microscopy (MFM) [173], as shown in Fig. 5.8. The observed domain structures were classified with different symmetry types and showed an evolution from one symmetry type to another as function of both temperature and external magnetic field. This reaffirms that the features observed in the magnetisation dynamics experiment below the saturation field (Fig. 5.7) corresponds to dynamics of multiple magnetic domain structures. Although, the presence of multidomains are realised by the FMR experiment, it is not possible to obtain the symmetry and type of structures for these domains by a resonance experiment alone. Hence, one has to be careful in extracting any magnetic parameters in the bulk layered CGT system at low magnetic fields as a small dynamic demagnetising field can exist from the interaction of different magnetic domains with each other and also with that of domain wall boundaries.

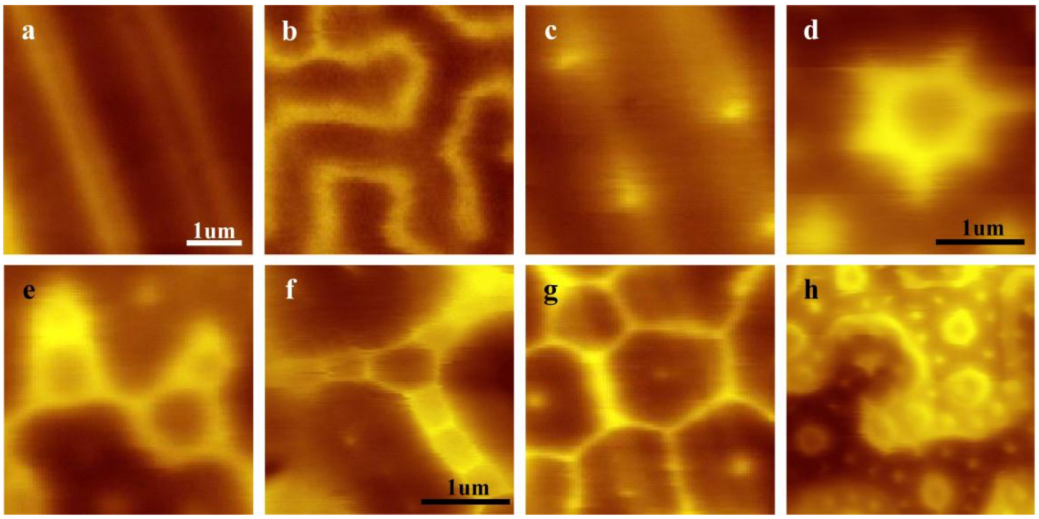

Figure 5.8: (a-h) Shows the MFM images for different kinds of magnetic structures obtained in the single cyrstal sample of CGT, where 8 different magnetic structures are identified by varying the temperature and externally applied magnetic field. These structures are characterised as (a) stripe, (b) maze, (c) dot, (d) disk, (e) line-connected dots, (f) Y-shaped connects, (g) honeycomb and (h) self-fitting disk. The figure is taken from Ref. [173].

5.6 Anisotropic Orbital Moment

The observation of anisotropic spectroscopic g-factor mentioned earlier in sec. 5.4 (by FMR experiments) as a function of temperature along the in-plane and out-of-plane orientations lead to acquiring beam-time at Diamond light Source (DLS) synchrotron facility (beam-line I10). A detailed XMCD investigation[4] was carried out for the CGT single crystal in order to probe the presence of the unquenched orbital moment in CGT originating from the d-orbitals of Cr atoms. Experiments were performed in the temperature range of 10 - 80 K with external magnetic field ($\approx$ 2 T) applied along the out-of-plane (c-axis, 0°, referred to as the normal incidence) and close to the in-plane ($\approx$ 15° off the ab-plane referred to as the grazing incidence) orientations, where the X-ray wavevector was parallel to the c-axis orientation and at an angle to the in-plane orientation. The X-ray absorption spectra (XAS) were obtained in the photon energy range of 565 - 600 eV as the Cr $L_{2,3}$ edges lie in this window (E_{L3} at $\approx$ 574.1 eV and E_{L2} at $\approx$ 583.8 eV) [162].

Figure 5.9 (a) shows the XAS spectra obtained at 10 K for CGT single crystal sample with external magnetic field parallel (XAS^{-}) and anti-parallel (XAS^{+}) to the helicity of the incident circularly polarised photons. The raw data showed a strong background dependence as a function of energy (discussed in more detail below) beyond $\approx$ 586 eV when compared with the spectra of other Cr-based materials [174]. The sum-rule analysis (as earlier mentioned in chapter 2) were applied in order to calculate the orbital moment [61]. For this reason, the XMCD signal was obtained by subtracting (XAS^{-}) with (XAS^{+}), which can be seen in Fig. 5.9 (b), along with the corresponding integrated XMCD signal. The green arrow in Fig. 5.9 (a) and (b) highlights an additional feature at $\approx$ 573 eV which is attributed to the M_5 edge of Te [175]. This feature is not seen if the elementary character measured by XMCD is Cr as the energy of the L_3 edge is at $\approx$ 574.1 eV, and therefore it provides further evidence of the hybridisation of the d-orbitals of Cr and p-orbitals of Te as discussed earlier in the case of g-factor temperature dependence.

The amplitude of the XMCD signal (proportional to the magnetisation in the

[4]The XMCD experiments were performed together with Dr. Larissa Ishibe Veiga (LCN) and also with the help of beam-scientist Dr. Peter Bencok (DLS).

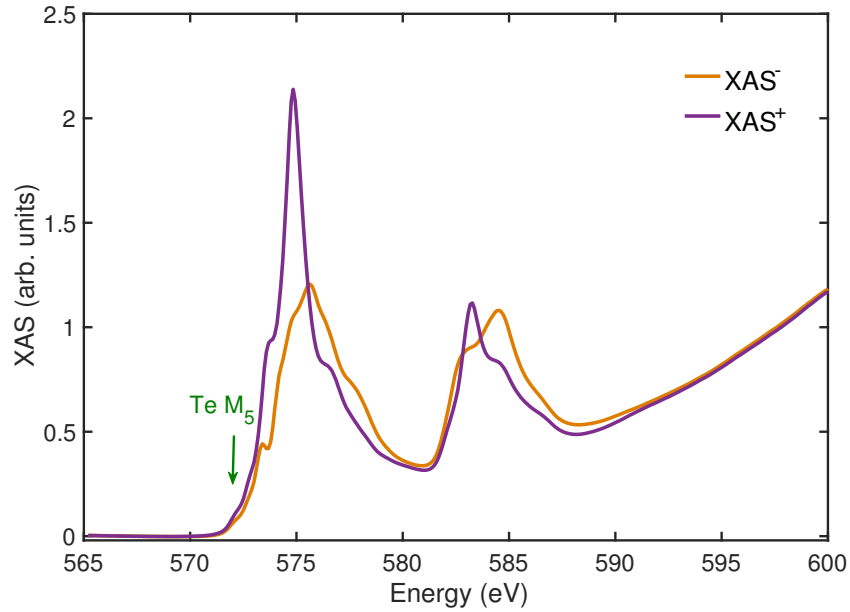

(a)

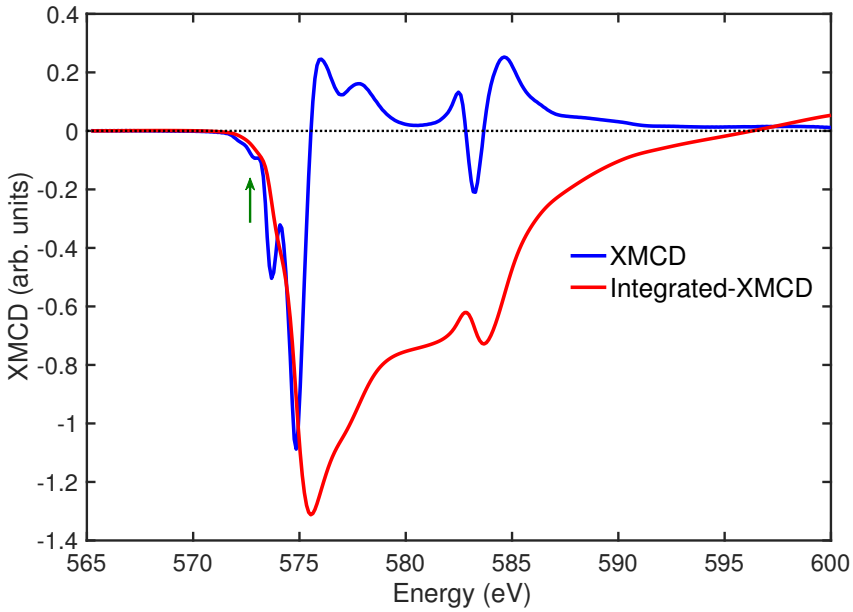

(b)

Figure 5.9: (a) $L_{2,3}$ edge x-ray absorption spectra (XAS) with the external magnetic field (≈ 2 T) parallel (XAS^{-}) and anti-parallel (XAS^{+}) to the helicity of the incident circularly polarised photons at 10 K for the grazing incident. A small feature at $\approx 573eV$ is seen which agrees with the energy at which the Te M_5 edge is expected. (b) The corresponding XMCD, ($XAS^{-} - XAS^{+}$) and integrated XMCD signal ($\int XAS^{-} - XAS^{+}$ dE) used for the application of the sum rules.

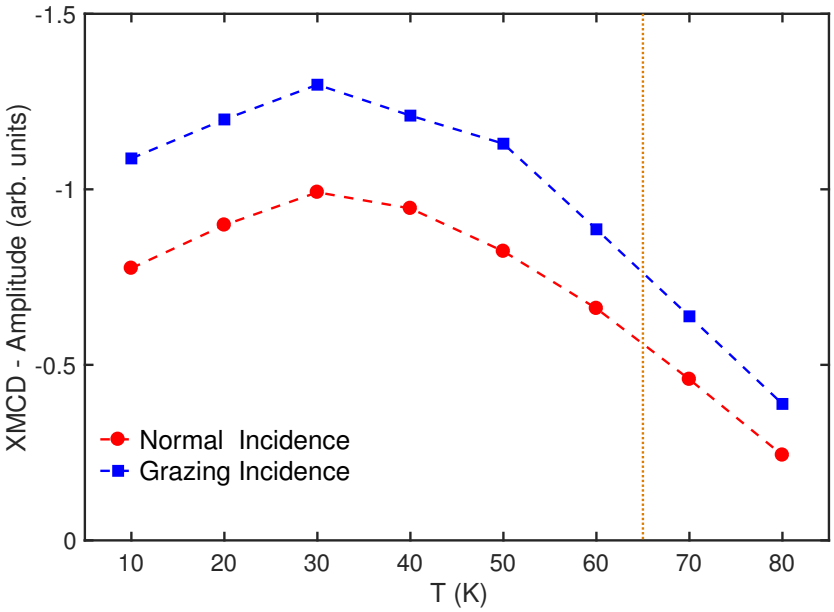

(a)

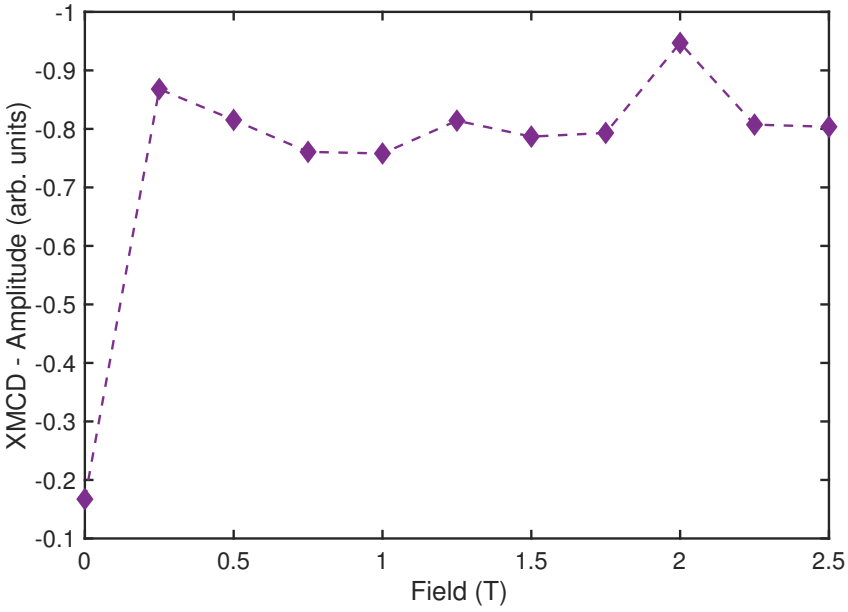

(b)

Figure 5.10: (a) Shows the amplitude of the XMCD signal as a function of temperature with external magnetic field applied along the normal incidence (c-axis) and grazing incidence (ab-plane) orientations. (b) The dependence of the XMCD signal on the external magnetic field applied along the c-axis at 10 K.

material) as a function of both temperature and external magnetic field ($\approx$ 2 T) orientation of in-plane and out-plane directions was extracted and is shown in Fig.

5.10 (a). The amplitude qualitatively showed a decreasing trend beyond the T_c of CGT sample. Figure 5.10 (b) shows the dependence of the XMCD amplitude on the external magnetic field with field direction along the c-axis at 10 K, and the CGT sample saturates at ≈ 2 T as shown by the magnetometry measurements in section 5.1, so all the measurements were performed with this strength of the magnetic field.

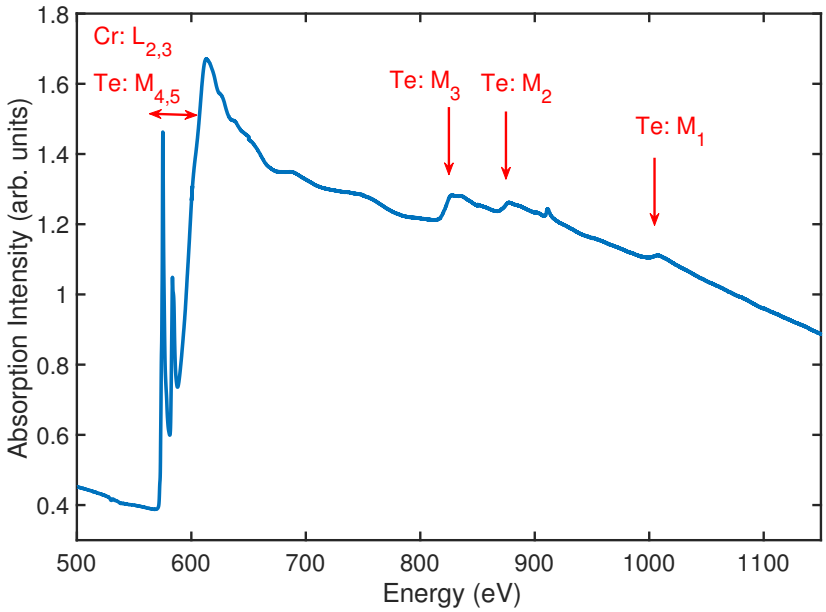

Figure 5.11: Shows the absorption intensity of the XAS at room temperature for the CGT sample in the extended energy range which is beyond the range of Cr $L_{2,3}$ edges in order to probe the influence of Te M edges on the background signal.

In order to find the origin of the background signal observed in the XAS spectra of CGT after the photon energy of ≈ 586 eV in Fig. 5.9 (a), an extended XAS measurement was performed through the Cr $L_{2,3}$ edges and up to the 1150 eV energy value, and it is shown in Fig. 5.11. It is realised that the background in fact was caused by the presence of the Te atoms in CGT, where different M edges of Te were identified [176] as highlighted in Fig. 5.11. The background signal in the energy range of $586 - 600$ eV is most likely due to the Te M_4 edge, whereas when the CGT sample is cooled down below the T_c, an additional feature at 573 eV appears (as shown in Fig. 5.9) corresponding to the Te M_5 edge, highlighting that there is hybridisation between the d-orbitals of Cr and p-orbitals of Te in CGT.

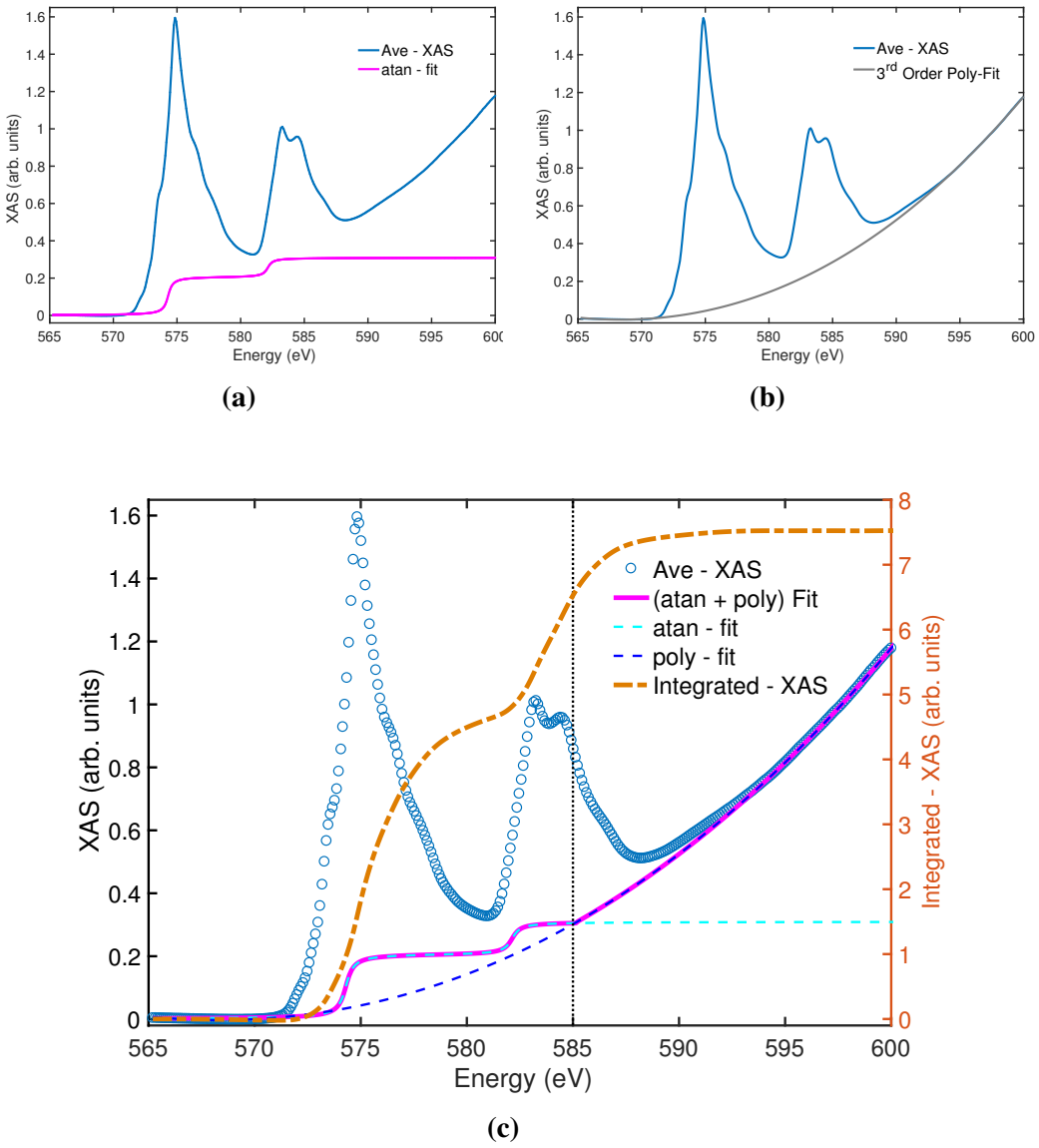

Figure 5.12: (a) Shows the arc-tangent step function fit to the XAS raw data. (b) The XAS is fitted with a third-order polynomial function to correct the background signal present due the *M* edges of the Te. (c) The arc-tangent and the polynomial functions were combined, and then subtract from the XAS data. The corrected XAS signal was then integrated in order to obtain the $\int$ XAS^{-}+ XAS^{+} dE for the sum-rule analysis.

The next steps of the sum-rule analysis were followed, where firstly for the application of the sum-rules it is a requisite to remove the photoelectron excitations into the continuum states from the absorption coefficient [61, 177], hence for this reason an ad hoc arc-tangent step function was first fitted to the XAS spectra (XAS^{-}+ XAS^{+}), as can be seen in Fig. 5.12 (a). In order to correct the XAS

spectra from the background coming from Te *M* edges, a third-order polynomial function was fitted to the $XAS^{-} + XAS^{+}$ data in the energy range of 570 - 600 eV, as shown in Fig. 5.12 (b). The step and polynomial functions were then combined and subtracted from the raw XAS data before the integration. Then, the numerical integral ($\int XAS^{-} + XAS^{+}$ dE) was calculated, and the full procedure is captured in Fig. 5.12 (c). As discussed in chapter 2, the orbital moment can be calculated from the XAS and XMCD signals by performing the well-known sum-rules analysis, where the orbital moment can be determined by the following equation [61]:

$$\mu_L[\mu_B/\text{atom}] = -\frac{4}{3}\frac{\int_{L_3+L_2}(XAS^{-} - XAS^{+})dE}{\int_{L_3+L_2}(XAS^{-} + XAS^{+})dE}(10 - n_{3d}) \tag{5.7}$$

where $XAS^{-/+}$ is the helicity of the incident circularly polarised photons parallel and anti-parallel to external magnetic field, respectively. n_{3d} is the 3_d electron occupation number of the specific transition metal atom.

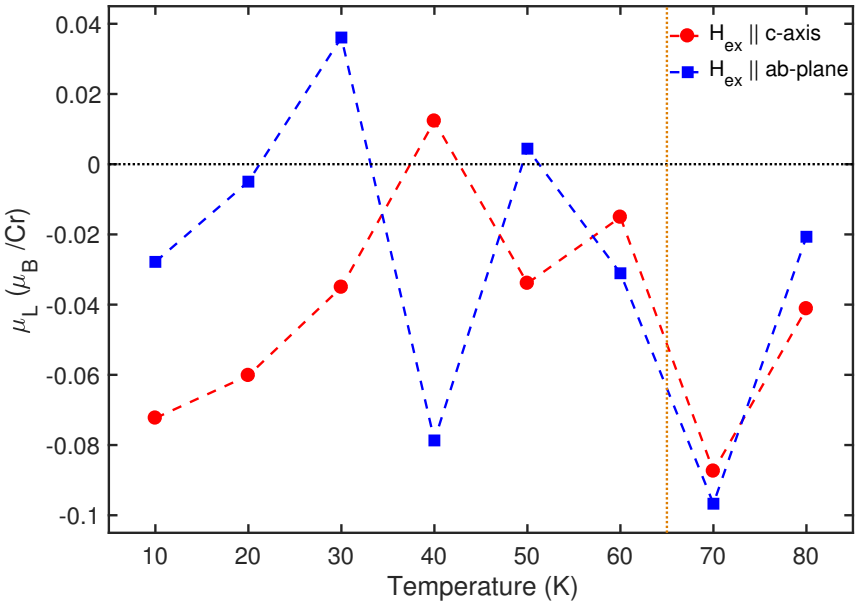

Figure 5.13: The temperature dependence of experimentally obtained orbital moment for the CGT single crystal determined using the sum-rule analysis with magnetic field along the out-of-plane (c-axis) and in-plane (ab-plane) orientations.

The integral values of the numerator and the denominator in Eq. 5.7 were numerically calculated using the procedure shown in figures 5.9 and 5.12, respectively,

with the value of n_{3d} taken as 3.5 for the case of Cr [175]. Therefore, the temperature dependence of the orbital moment in CGT sample was determined with external magnetic field along the c-axis and ab-plane, as shown in Fig. 5.13. A sizeable orbital moment was seen confirming the earlier prediction by the FMR experiment that the orbital moment is not quenched in single crystal of CGT. Also, a visible anisotropy can be seen between the two orientations. The existence of orbital moment anisotropy qualitatively complements the g-factor anisotropy shown in Fig. 5.6. An important observation is the change in the sign of the orbital moment, as at 20 K the recent literature [162] reports a negative sign of the orbital moment expected for less than half-filled system (L and S are anti-parallel), but in this experiment in the temperature range of 30 - 50 K, a crossing behaviour was observed with some values of the orbital moment having a positive sign.

Even though a sizeable orbital moment is seen in Fig. 5.13, one has to be very cautious in the trend of the temperature of the orbital moment along the in-plane and out-of-plane orientations. The reason behind this is the presence of the background signal due to the *M* egdes of Te towards the high-energy part of the spectrum. As mentioned earlier, the sum-rule analysis are used to determine the orbital moment, μ_L, which is calculated as following

$$\mu_L \ [\mu_B/\text{atom}] = -\frac{4q}{3r}(10 - n_d) \tag{5.8}$$

where q (r) is the numerator (denominator) in Eq. 5.7. The process of determining the value of q in the above equation involves the analysis procedure shown in Fig. 5.12, and it can be seen that the cut-off point in subtracting the polynomial background makes it difficult to calculate q reliably, and hence, the sign change in the temperature dependence of orbital moment in Fig. 5.12 can be misleading. In order to reliably confirm the trend seen in this measurement, theoretical *ab initio* calculations of the XAS and XMCD spectra in CGT as a function of temperature can shed more light into the origin of the sign-flip of the orbital moment at certain temperatures. The spin moment (μ_S) was not calculated by this experiment as in order to determine the spin moment, the XMCD integral must also be evaluated over

the spin-orbit split edges separately. This is especially problematic in the case of Cr because the L_2 and L_3 edges are so close in energy (Fig. 5.9) that their overlap leads to errors of up to 100% [178].

5.7 Conclusion

In conclusion, the FMR behaviour of bulk two dimensional CGT was investigated. In particular, broadband FMR experiments were performed within the temperature range of 60 K - 2 K with external magnetic fields along the in-plane and out-of-plane orientations. The initial focus was on the temperature dependence of the magnetic anisotropy energy, spectroscopic g-factor and the multi-domain resonance features (observed below the saturation fields along the ab-plane). A uniaxial perpendicular magnetic anisotropy was found with easy axis parallel to the c-axis (out-of-plane). The scaling of the normalised magnetocrystalline anisotropy constant and saturation magnetisation showed a deviation from the theoretically predicted Callen-Callen power law. The presence of spin orbit coupling from d-orbitals of Cr atoms and an off-site spin orbit coupling from p-orbitals of the ligand Te atoms can be a contributing factor to this contradicting behaviour of power law dependence of magnetic anisotropy to magnetisation.

The obtained g-factor showed an anisotropic response, i.e. a cystallographic dependence, and at 2 K it was found to be $g_{\parallel} = 2.18 \pm 0.02$ (ab-plane) and $g_{\perp} = 2.10 \pm 0.01$ (c-axis). The determined g-factor values were greater than 2, again, indicating that the orbital magnetism played an important role in bulk CGT when considering magnetic interactions in this system. A small anisotropy in the orbital magnetic moment relative to the spin moment was found from the FMR experiments. Based on these findings, a detailed X-ray magnetic circular dichroism study was performed at the DLS facility. The XMCD investigation of CGT experimentally confirmed that a sizeable orbital moment was present. The orbital moment also showed an anisotropy with external magnetic field along the c-axis and and the ab-plane as a function of temperature, complementing the results obtained through FMR spectroscopy. Finally, the presence of multidomain structures was qualita-

tively confirmed as domain-mode resonance phenomena was observed along the ab-plane (in-plane) orientation.

Chapter 6

Modifying Magnetic Properties of CGT via Intercalation

The presence of intrinsic magnetic order in layered van der Waals (vdWs) bulk pristine single crystal of $Cr_2Ge_2Te_6$ (CGT) is discussed in the previous chapter. As already mentioned in the introduction of this thesis, a slight draw-back of these two-dimensional (2D) magnets is that the Curie temperature (T_c) lies towards the low temperature region, where cryogenic facilities are required to probe their magnetic properties [17].

Recently, efforts have been made to enhance the T_c and tune the magnetic properties in these systems. One such example is the study of gate-tunable room temperature ferromagnetism in layered 2D Fe_3GeTe_2 (FGT) [18]. In a few layer FGT system, the application of an ionic (lithium based solid electrolyte) gate, probed by Hall resistance method, raises the T_c above room temperature, which is much higher than the bulk T_c [18]. The reason of the enhancement of ferromagnetic order is stated as that the application of gate voltage intercalates lithium ions into the FGT thin flakes, similar to a charging process in a lithium-ion battery, and the charge tranfer between the host crystal and the lithium ions induces strong electron doping. The electron doping causes a sizable shift of the electronic bands of FGT, showing a large variation of density of states (DOS) at the Fermi level, and this leads to appreciable modulation of ferromagnetism. Another case study is the signficant enhancement of T_c in gated (polymer gel based ionic liquid)-CGT sample,

where hysteresis in magnetoresistance (MR) measurements (a signature of ferromagnetism) is seen at temperatures of up to $\approx$ 200 K in an electron doped CGT device [19]. Along with the enhancement of T_c, angle-dependent MR measurements in this study reveals switching of magnetic easy-axis from out-of-plane easy axis to in-plane (layer plane) compared to the undoped-CGT. The change in the exchange mechanism from superexchange interaction dominant in the insulating phase (undoped CGT) to double-exchange interaction (doped CGT) mediated by free carriers is proposed as a reason of tailoring the magnetic properties via electrostatic gating [19].

In this chapter, the experimental evidence for the enhancement of ferromagnetic transition temperature and the change in magnetic anisotropy is presented for the case of alkali metal ($Na_{0.3}$) intercalated CGT ($Na_{0.3}$-CGT). The chemically intercalated Na-ions sit in the vdWs gap of CGT. The magnetic properties are probed by the magneto-transport and ferromagnetic resonance (FMR) spectroscopy techniques. The sample investigated by the magneto-transport measurement shows a magnetoresistance (MR) signal up to 195 K, whereas the sample used for the FMR experiment reveals a FMR signal up to the temperature of 240 K. In both the transport and magnetic resonance measurements, the magnetic anisotropy is found to be changed compared with unintercalated CGT sample, as the magnetic easy-axis is found to lie along the in-plane (ab-plane) orientation whereas it is along the out-of-plane (c-axis) orientation in the case of CGT.

6.1 Sodium (Na_x)-CGT Sample

Among the doping methods, ion-intercalation [179] is the optimal candidate for the study of the effect of doping on the magnetism of CGT, as electrostatic doping devices prohibits direct access to the sample surface [18] thus hindering the use of surface sensitive techniques and in-situ surface doping [180] would likely deteriorate sample crystallinity. A $x = 0.3$ (where x is the amount of intercalation) stoichiometric amount of Na was used in the employed low temperature liquid metal ammonia technique[1] [179] in order to intercalate alkali metal ions in the vdW gaps of bulk CGT and make $Na_{0.3}$-CGT. The unit cell of the CGT and $Na_{0.3}$-CGT is shown in Fig. 6.1, where the Na ions are shown to sit in the gaps between the layers.

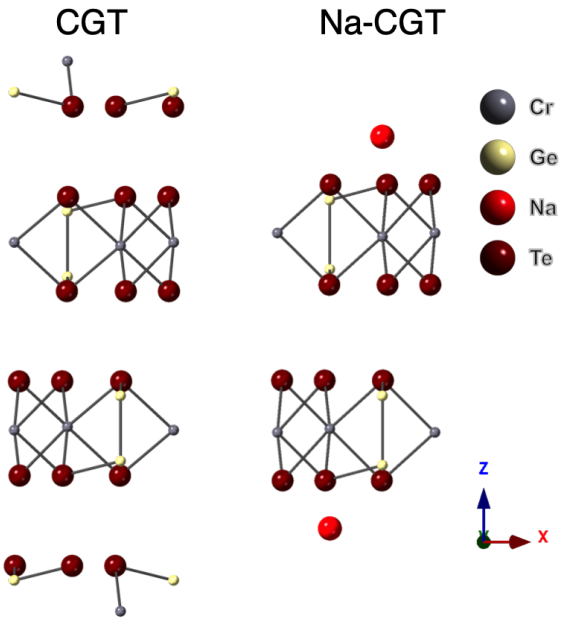

Figure 6.1: Shows the schematic of the unit cell of CGT (left-side) and $Na_{0.3}$-CGT (right-side).

The X-ray diffraction (XRD) patterns of the pristine bulk crystals of CGT and the intercalated $Na_{0.3}$-CGT displaying a series of out-of-plane (00l) peaks are shown in Fig. 6.2 (a) and (b). The XRD pattern of unintercalated CGT (Fig. 6.2 (a)) agrees well with the earlier reports in the literature [181]. The starting CGT crystal

[1] As mentioned in the previous chapter, the single crystal samples of pristine CGT were grown by Dr. I. Verzhibitskiy (National University of Singapore). The CGT samples were intercalated by Dr. M. K. Bin Subhan (UCL Department of Physics & Astronomy), who also performed the XRD measurements, and the XRD data presented here is used with his permission.

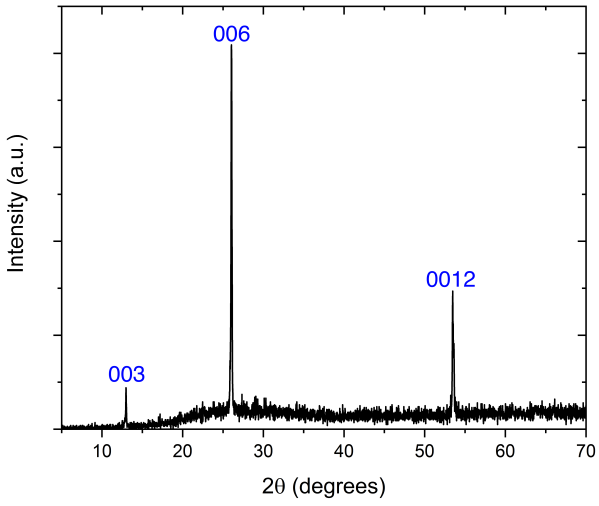

(a)

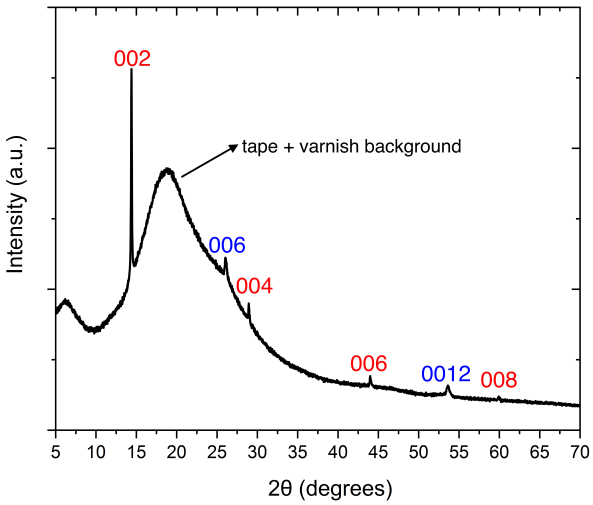

(b)

Figure 6.2: X-ray diffraction (XRD) patterns of (a) pristine bulk CGT and (b) intercalated $Na_{0.3}$-CGT showing a series of (00l) diffractions. The peaks labelled blue are CGT peaks and peaks referred in red shows the appearance of new peaks after intercalation.

has 3 layers in the unit cell with the (003) out-of-plane peak in the XRD pattern at 12.9° giving inter-layer spacing of 2.28 $\AA$. After the intercalation process, the Na ions sit in every other layer and so forming a two layer unit cell rather than 3 layer cell and a new stacking order. A new peak can be seen around 14.4° which can be

attributed to the (002) out-of-plane peak of the intercalated structure (Fig. 6.2 (b)), giving an increased layer spacing of 3.08 $\AA$, and hence an increase of ≈ 0.8 $\AA$ in the vdWs gap. A small increase in the layer spacing like the one reported here is not unusual and a similar effect is seen in Cu intercalated Bi_2Se_3 [182]. It seems like a small amount of unintercalated CGT phase remains in the XRD patterns, as can be seen by the peaks in Fig. 6.2 (b), highlighted in blue.

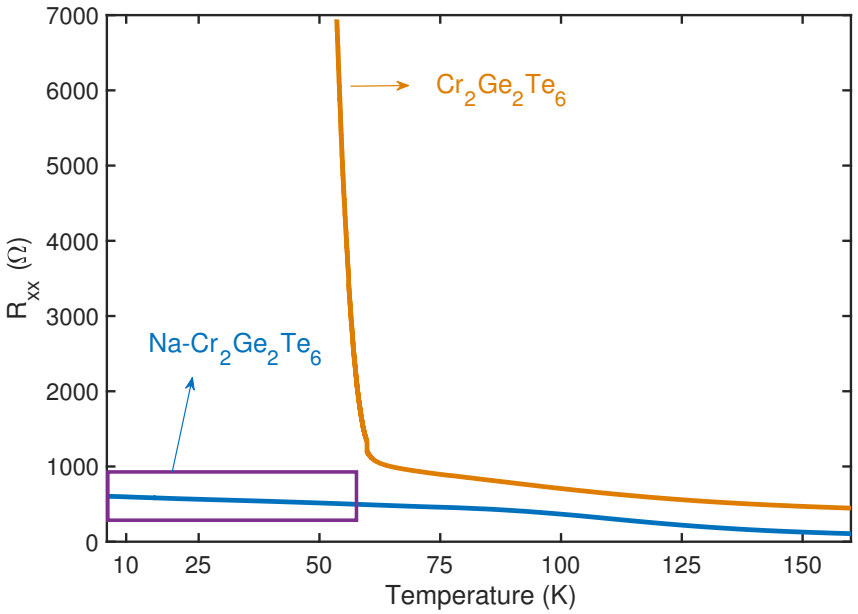

Figure 6.3: The electrical transport measurement of the bulk CGT and $Na_{0.3}$-CGT as a function of temperature. The purple box highlights that the resistance of the intercalated sample is measurable in the low-temperature region.

Figure 6.3 shows the temperature dependent resistance (R_{xx}) of CGT and $Na_{0.3}$-CGT in the zero-field cooling regime (no external magnetic field). In the case of CGT, a typical semiconductor behaviour is seen and it enters the insulating phase just below the ferromagnetic transition temperature, as reported elsewhere [183]. In addition to the XRD data, the temperature dependent resistance measurement also confirms successful intercalation of the Na ions in CGT, where the system does not enter the insulating phase as clearly evident by the purple box in Fig. 6.3. This contrasts with the unintercalated CGT system, and highlights that the intercalation induces electron doping in $Na_{0.3}$-CGT, which may cause the shifts in the electronic band structure. A recent theoretical study using the first principles cal-

culations and spin-wave theory suggests that the surface adsorption of alkali metals induces metallicity in CGT, hence providing a way to control the band structure [184]. A point to note here is that $Na_{0.3}$ intercalation does not make the system fully metallic as the resistance still goes up in the low-temperature region instead of going down, but this does allow probing the magnetic properties of the sample via electrical transport technique which is not possible in CGT.

Several samples of intercalated CGT samples were made and kept in an inert atmosphere. The samples were found to be air-sensitive, and hence, the preparation of the samples for magneto-transport and FMR measurements was carried out in the glovebox in order to prevent damage from oxygen and moisture. Two different samples of $Na_{0.3}$-CGT were used, referred to as sample (I) and sample (II) for magneto-transport and FMR studies, respectively. As discussed in more detail below, there were some differences in the observed magnetic response of the two samples, which is attributed to possible exposure to air during the transfer to experimental equipment for one sample relative to the other as the chemical intercalation is a reversible process where the sample reverts back to the original form after exposure to ambient conditions [179].

6.2 Magnetoresistance Measurements

The magnetoresistance (MR) measurements on $Na_{0.3}$-CGT sample (I) are performed using the setup described in section 3.4 (Fig. 3.9). A well-known four-point van der Pauw [83] electrical measurement technique was designed to probe the Hall resistance (R_{xy}), and the anisotropic magnetoresistance (AMR) in the device. The Hall resistance signal is composed to two-parts, as $R_{xy} = R_{NH} + R_{AH}$, where R_{NH} is the normal Hall resistance and $R_{AH} = R_s M$ is the anomalous Hall resistance containing the crucial information about the magnetic order due to dependence on magnetisation, M [18]. During the sample loading and cooling down process, one of the electrical contacts stopped working in the device, and hence only the two-point resistance ($R_{xx} = R_{13}$ in Fig. 3.9) was examined as a function of temperature and external magnetic field. The external magnetic field was applied along

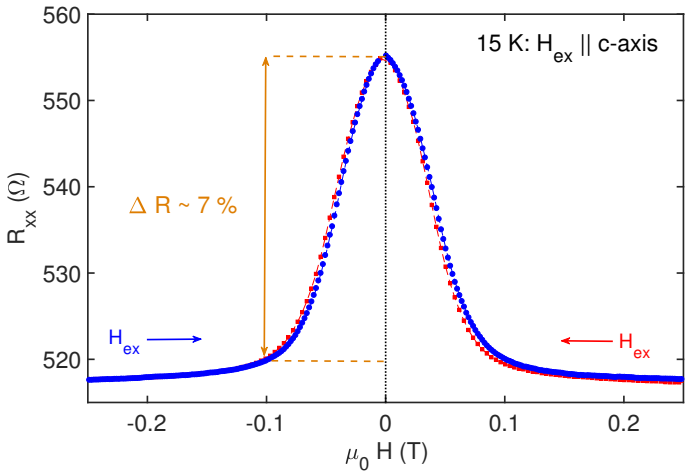

(a)

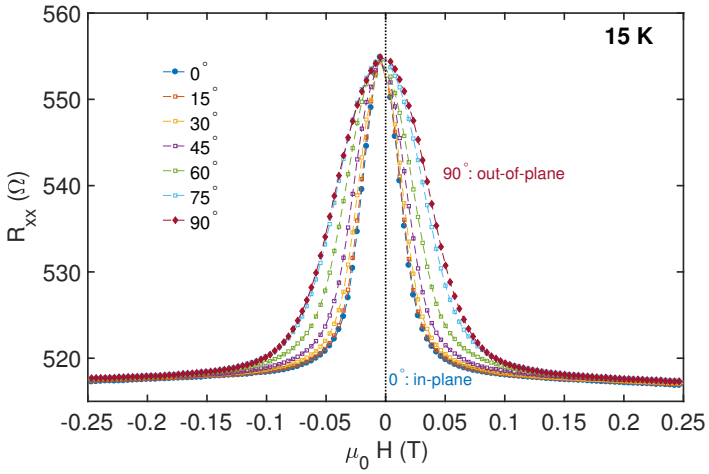

(b)

Figure 6.4: (a) Shows the experimental MR curve at 15 K for the $Na_{0.3}$-CGT sample with the external magnetic field along the out-of-plane (c-axis) orientation and the magnetic field (H_{ex}) swept from the $+$ve field to $-$ve field and vice versa. (b) Highlights the dependence of the MR curve as a function of H_{ex} applied from the out-to-plane to the in-plane orientation.

different orientation of the crystalline axis from the in-plane (ab-plane) and out-of-plane (c-axis) directions, and throughout the measurement the current direction was transverse to the magnetic field as shown earlier in Fig. 3.9 (b).

The experimental MR curve at 15 K in $Na_{0.3}$-CGT with external magnetic field (H_{ex}) along the c-axis is shown in Fig. 6.4 (a). Approximately, 7% change of resistance at 15 K is seen from R($H_{ex} = 0$) to R(H_{ex} = high-field value), and a very small hysteresis is also observed with H_{ex} swept from positive-field to negative-field

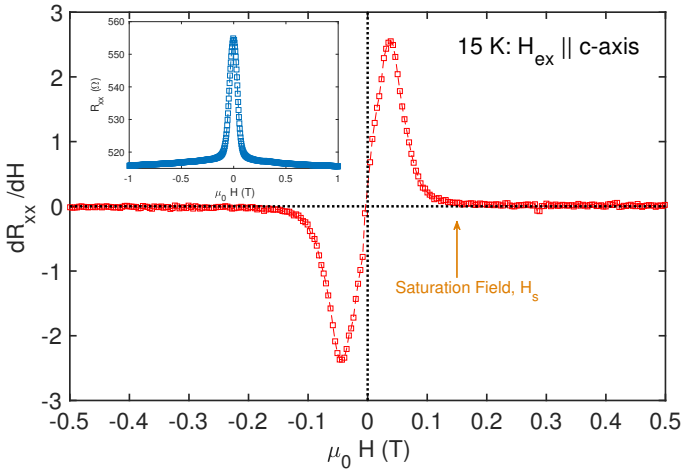

(a)

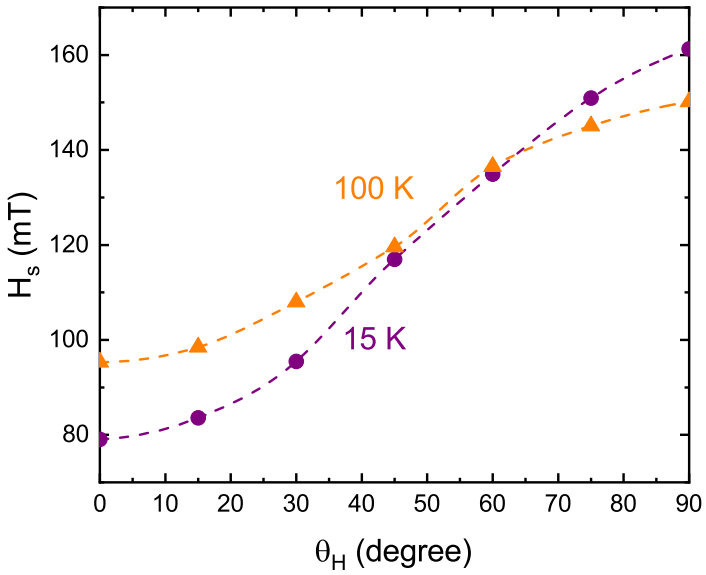

(b)

Figure 6.5: (a) Inset shows the raw R_{xx} signal and the main plot shows the derivative, dR_{xx}/dH, used for extracting the saturation field. (b) Angular dependence of the saturation field from in-plane (0°) to out-of-plane (90°) at 15 K and 100 K.

and the reverse direction. Fig. 6.4 (b) shows the dependence of R_{xx} signal on the orientation of H_{ex} along the different directions from in-plane to out-of-plane directions. This provided the first experimental evidence of the switching of magnetic anisotropy in $Na_{0.3}$-CGT compared to unintercalated CGT (as shown in the previous chapter), where the magnetic easy axis lies along the in-plane direction as the

c-axis direction shows a high saturation field value.

Figure 6.5 (a) shows the method of extracting the saturation field, H_s. The raw R_{xx} signal exhibits linear MR component at high magnetic field values as can be seen in the inset of Fig. 6.5 (a). The numerical differential of R_{xx} is obtained, dR_{xx}/dH, which then excludes the linear MR component as it shows a constant gradient making it easier for reliable extraction of H_s [185]. The angular dependence of the extracted H_s at 15 K and 100 K is shown in Fig. 6.5 (b). It clearly highlights that the magnetic anisotropy in the system has a two-fold symmetry where the size of anisotropy is reduced at 100 K compared with 15 K.

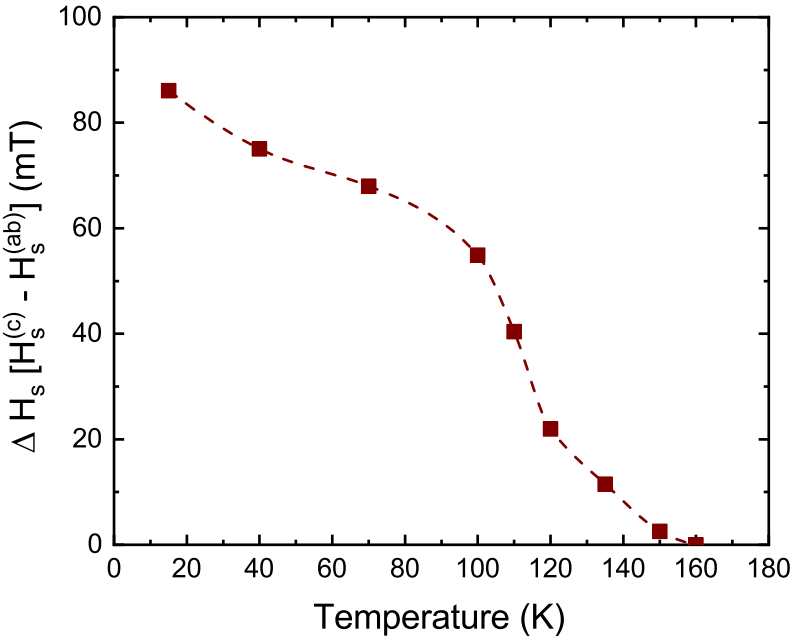

Figure 6.6: Temperature dependence of anisotropy field, ΔH_s.

The anisotropy field, ΔH_s, is defined as the difference of saturation fields along the out-of-plane (H_s^c) to the in-plane H_s^{ab} orientation. The temperature dependence of the anisotropy field is shown in Fig. 6.6. A sizeable magnetic anisotropy in the $Na_{0.3}$-CGT sample (I) persists up to the temperature of 150 K, which is almost twice the value of the Curie temperature of CGT, and in contrast to the CGT system, the anisotropy field seem to have flipped the sign.

In Fig. 6.7, the relative peak amplitude of the MR signal is plotted. A peak

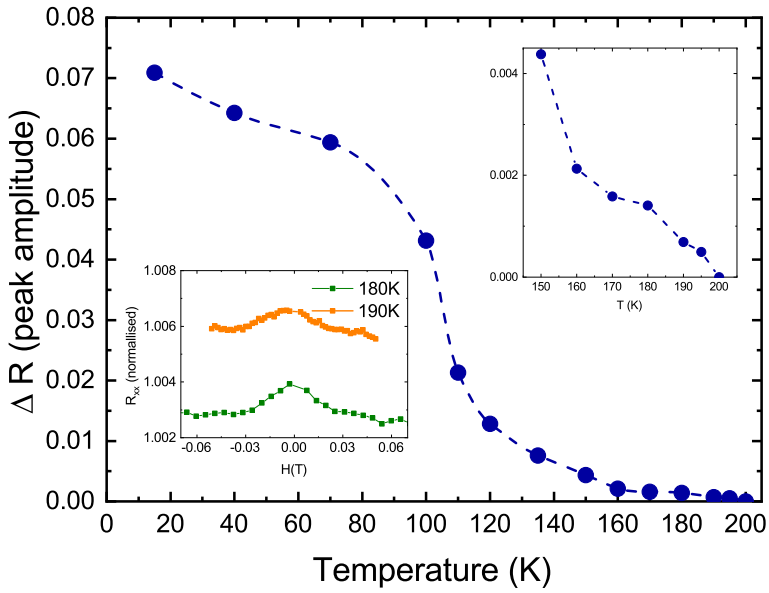

Figure 6.7: The main plot shows the relative peak amplitude of the MR curve as function of temperature. The inset on the bottom-left shows MR curves at 180 K and 190 K, and inset of the top-right shows the peak amplitude in the vicinity of high temperatures.

amplitude of 0.005 is observed at 150 K, and relating this with the anisotropy field disappearance above 150 K, the MR signal at 160 K and above is believed to be a field-driven effect, and as shown in the top-right inset of Fig. 6.7, the signal vanishes at 200 K. Qualitatively, the MR measurements of $Na_{0.3}$-CGT sample (I) shows three strikingly different features when compared with the CGT system: (i) measurable resistance at low-temperatures as the system does not enter the insulating state, (ii) a sizeable magneto-transport response at high-temperatures than the unintercalated CGT, and (iii) a change in the magnetic anisotropy with magnetic easy axis lying in the layer-plane (ab-plane) instead of the c-axis. The loss of an electrical contact in the measuring device prohibited a thorough quantitative analysis, as the Hall resistance (containing the anomalous Hall response) was not measured.

6.3 Ferromagnetic Resonance Spectroscopy

The magnetisation dynamics in the $Na_{0.3}$ intercalated CGT sample (II) was probed by the FMR spectroscopy technique in a similar way to the spin dynamics results

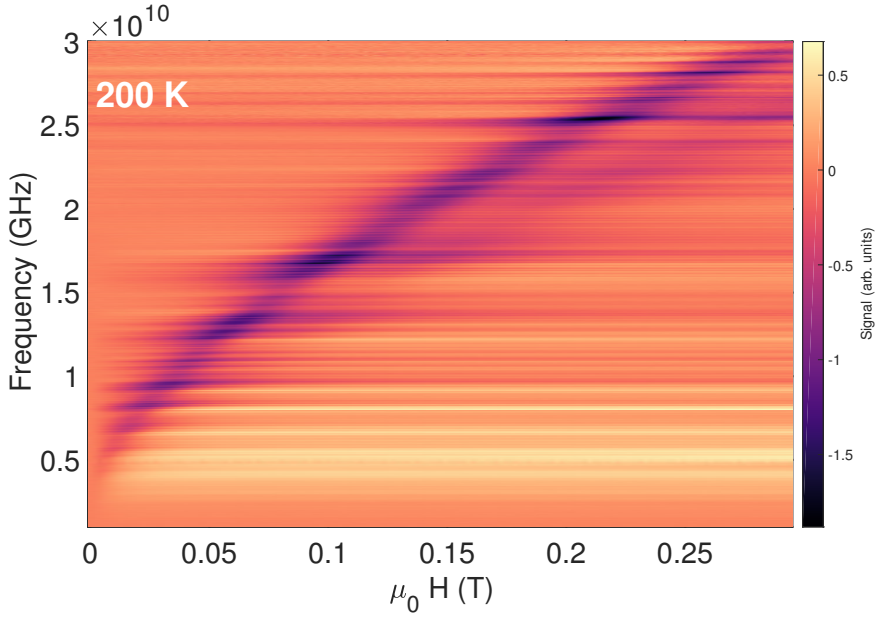

(a)

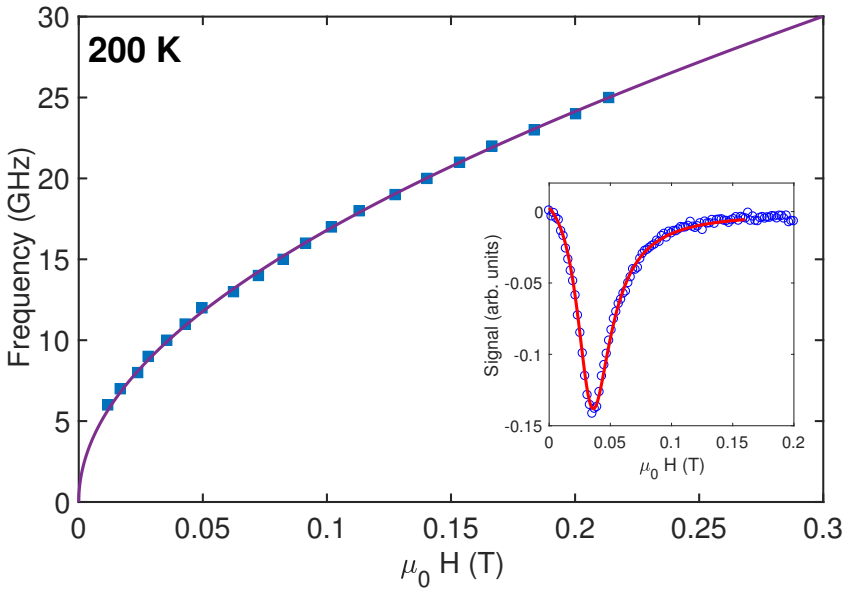

(b)

Figure 6.8: (a) The FMR signal (the magnitude of the transmission signal, S_{21}) observed in $Na_{0.3}$-CGT sample (II) at 200 K, with external magnetic field applied along the in-plane (ab-plane) orientation (b) Inset shows a characteristic FMR spectra fitted with a Lorentzian function (red curve). The main plot shows the frequency dependence of the resonance field, H_r, i.e. peak position, which is well described by the Kittel relation for the in-plane orientation.

presented in the previous chapter for the unintercalated CGT sample. The broad-band FMR spectra, for externally applied magnetic field along the in-plane (ab-plane) orientation, at 200 K is shown in Fig. 6.8 (a). The first important observation is that compared with MR measurements of $Na_{0.3}$-CGT sample (I), the FMR signal representing a prominent signature of the presence of magnetic order is seen at 200 K whereas MR signal vanished at 200 K. The resonance peak was fitted with a linear combination of symmetric and anti-symmetric Lorentzian functions in order to determine the resonance field, H_r (i.e. peak position), as shown in the inset of Fig. 6.8 (b). The main plot of Fig. 6.8 (b) shows the frequency dependence of H_r, which follows the FMR Kittel relation for the in-plane orientation, where the Kittel fitting is discussed in more detail below. Qualitatively, comparing this experimental data to the FMR spectra observed in the unintercalated CGT sample confirms the enhancement of magnetic order in the intercalated sample. Secondly, the in-plane resonance spectra of CGT showed a non-linear frequency dependence with the x-intercept exhibiting the typical magnetisation characteristic of magnetisation dynamics in a ferromagnet with hard magnetic axis whereas this does not seem to be the case for the $Na_{0.3}$-CGT sample as no x-intercept is visible in frequency dependence of resonance indicating a change of magnetic anisotropy in the intercalated sample.

The temperature evolution of the FMR spectra in $Na_{0.3}$-CGT sample (II) with magnetic field along the in-plane direction is shown in Fig. 6.9. The resonance spectra is clearly visible from the low-temperature of 15 K up to the high-temperature value of 240 K, and it vanishes at 250 K. This shows a significant enhancement of the ferromagnetic transition temperature (T_c) from ≈ 65 K in unintercalated CGT up to 240 K in Na-ions intercalated CGT. At all the measured temperatures the enhancement of T_c also seem to accompany the switching of the magnetic anisotropy in the system with magnetic easy axis now lying along the in-plane direction.

The FMR Kittel relation for the magnetic field along the in-plane orientation used to fit the resonance spectra in chapter 5 is utilised here to fit the frequency dependence of resonance field in $Na_{0.3}$-CGT sample, and it is written as

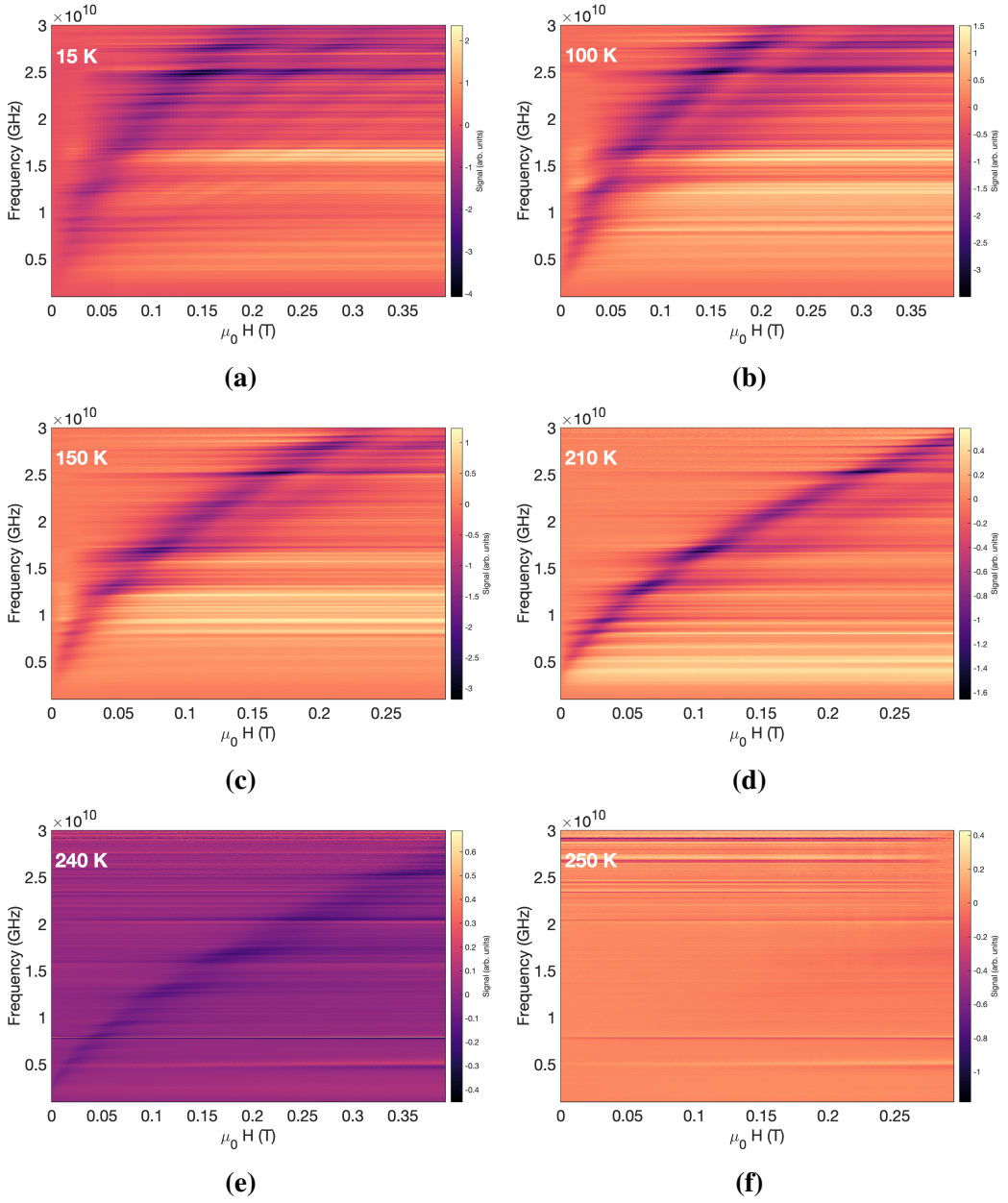

Figure 6.9: (a-f) Shows the temperature evolution of the FMR signal (the magnitude of the transmission signal, S_{21}) as a function of frequency and external magnetic field. The signal disappears at 250 K.

$$\omega_{(\|)} = \gamma\sqrt{H_r(H_r + 4\pi M_{eff})} \quad , \tag{6.1}$$

where $\gamma = g\mu_B/\hbar$ containing information about the spectroscopic g-factor, is the gyromagnetic ratio. H_r is the ferromagnetic resonance field, $4\pi M_{eff} = 4\pi M_s - H_u$ is the effective demagnetisation field and $H_u = 2K_u/\mu_0 M_s$, the perpendicular

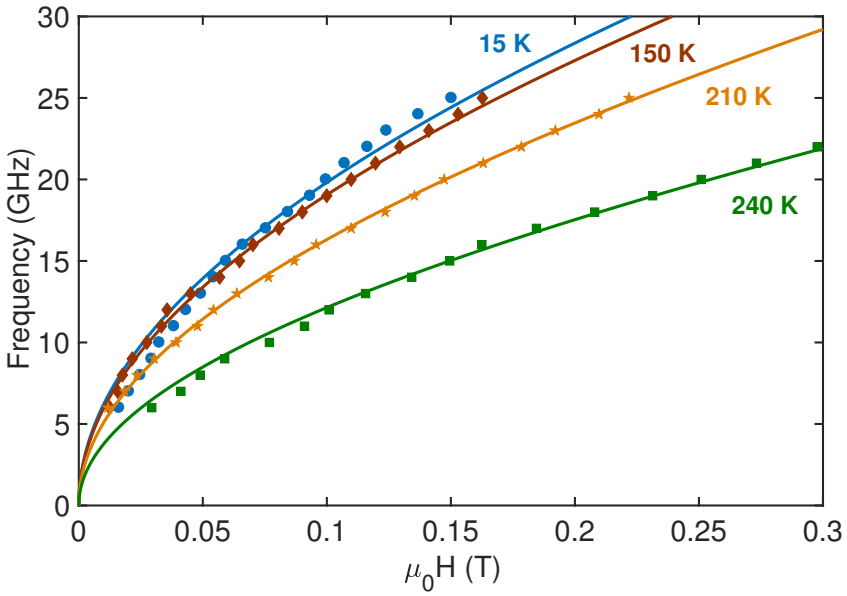

(a)

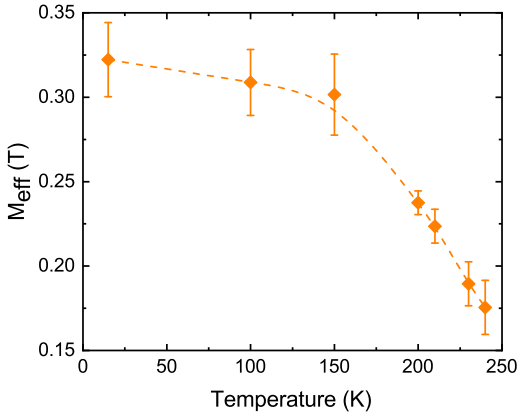

(b)

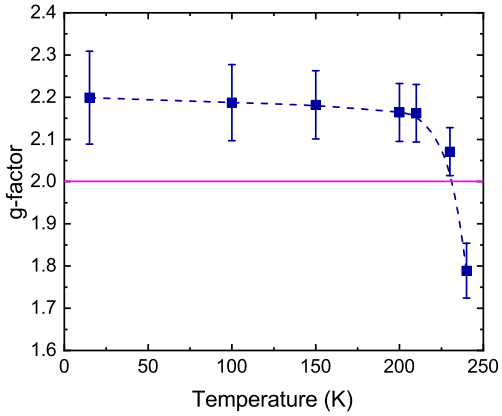

(c)

Figure 6.10: (a) Shows the frequency dependence of resonance field at 15K, 150 K, 210 K and 240 K. The solid lines represent the Kittel fitting. (b) and (c) show the temperature dependence of the extracted effective demagnetisation field (M_{eff}) and g-factor parameters, respectively, from the Kittel fitting in (a).

anisotropy field. As shown earlier in Fig. 6.8 (b), this Kittel relation fits well to the experimental data at 200 K.

Figure 6.10 (a) shows the frequency dependence of resonance field for the in-plane orientation and the relative fitting of the Kittel relation (Eq. 6.1) at different temperatures from 15 K to 240 K. Even at the high temperature of 240 K, the ex-

perimental data follows the Kittel relation with good agreement. As in the case of unintercalated CGT, an important observation is that the slope of the extracted FMR Kittel relation shows a clear temperature dependence suggesting that the spectroscopic g-factor is also not isotropic for the intercalated sample. The temperature dependence of the M_{eff} parameter, determined via the least-square fitting of Eq. 6.1 to the frequency-dependent FMR spectra, is shown in Fig. 6.10 (b). A change in the sign of M_{eff}, compared to the case of unintercalated CGT sample in the previous chapter, indicates the switching of magnetic anisotropy in the intercalated system. The temperature dependence of the spectroscopic g-factor for the in-plane orientation can be seen in Fig. 6.10 (c). The g-factor, as in the case of CGT, in the intercalated sample shows a deviation from the g-value of the free electron ($g = 2$), and hence indicating presence of the orbital moment playing a role in the magnetism of $Na_{0.3}$-CGT.

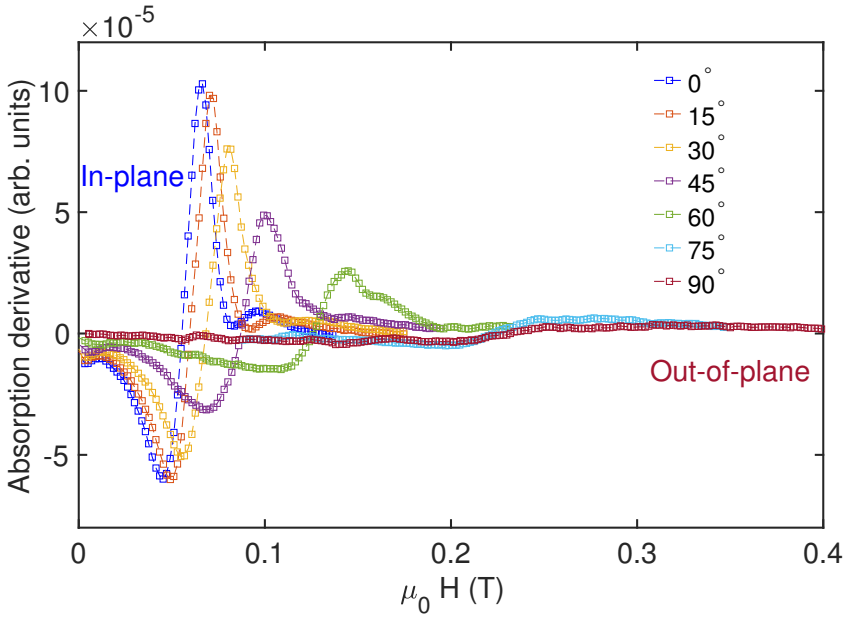

Figure 6.11: FMR spectra obtained from the highly sensitive field-modulation lock-in measurement technique showing the angular dependence of resonance peaks from the in-plane orientation towards to the out-of-plane direction. The measurement was performed with the sample placed on a CPW connected to a microwave source with frequency of 12 GHZ at all angles.

The broadband FMR spectra for external magnetic field along the out-of-plane (c-axis) is not observed for the $Na_{0.3}$-CGT sample (II). In order to probe the rea-

son for not seeing the resonance feature in the c-axis direction, a magnetic field-modulation experiment combined with the lock-in measurement technique was performed [186]. The angular dependence of the FMR field-derivative peaks from the in-plane to the out-of-plane orientation at 200 K is shown in Fig. 6.11. It can be seen that the linewidth of the FMR peaks increases as a function of the angle and the peak amplitude decreases, and after an angle of 60° away from the in-plane orientation it is quite difficult to resolve the FMR peak even with this highly-sensitive measurement method. Therefore, the resonance spectra is not seen along the out-of-plane orientation whereas in chapter 5, the out-of-plane FMR spectra of CGT showed a characteristic magnetic easy axis feature.

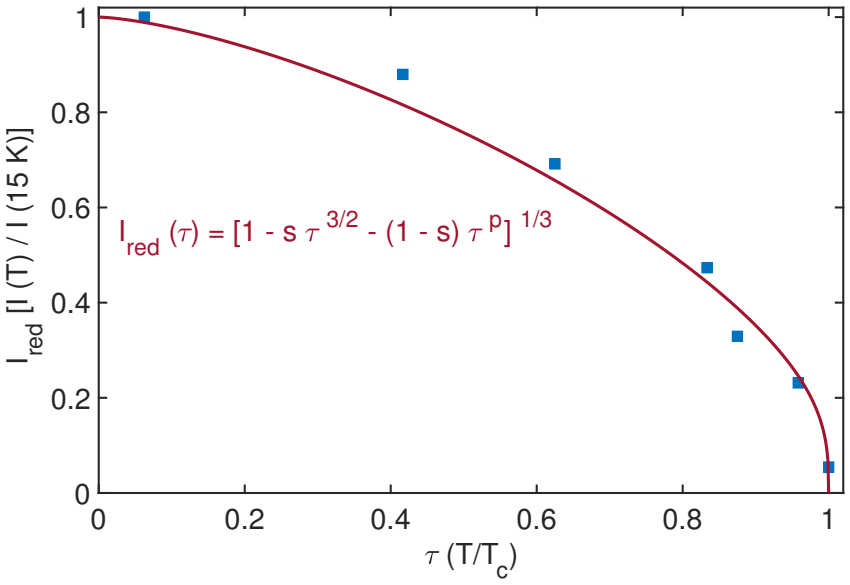

Figure 6.12: The reduced temperature dependence, τ (T/T_c), of the normalised peak amplitude of the magnetic resonance spectra measured at 12 GHz. The peak intensity is a relative measure of the magnetisation in the sample.

Even though the presence of FMR signal provides direct evidence of a significant enhancement of the ferromagnetic T_c in the bulk $Na_{0.3}$-CGT sample (II) of up to $\approx$ 240 K compared to the T_c of $\approx$ 65 K in bulk CGT. A methodology for the analysis of experimental data taking into account the shape of the temperature dependence of spontaneous magnetisation, M_s (T), rather the scale is considered here which is adapted from Ref. [187]. In order to consider the shape of M_s (T), reduced

spontaneous magnetisation and reduced temperature are defined as m = M_s (T)/M_0 and $\tau = T/T_c$, respectively. The empirical expression is given by [187]

$$m(\tau) = [1 - s\tau^{3/2} - (1-s)\tau^p]^{1/3}, \tag{6.2}$$

where s and p are the two scaling factors, constrained with $p > 3/2$ and $0 < s < 5/2$. This equation is established to obey the Bloch's 3/2 power law at low temperatures, $m \approx 1 - \frac{1}{3}s\tau^{3/2}$ as $\tau \to 0$, whereas in the case as $\tau \to 1$, m is proportional to $(1-\tau)^{1/3}$, as prompted by the critical behaviour of Heisenberg model [187]. The intensity of the FMR peaks observed in this experiment provide a relative measure of magnetisation in the sample, as the intensity of the absorption peak is proportional to the magnetisation [45]. The intensity was found by numerically integrating the FMR absorption peak. The dependence of the reduced intensity, $I_{red} = I$ (T)/I (15 K), as a function of reduced temperature, τ, is shown in Fig. 6.12. This dependence was then fitted with Eq. 6.2, with p and s as free parameters, and assuming a value of 240 K for T_c. This empirical expression does in fact yields the experimentally observed shape of the reduced intensity in $Na_{0.3}$-CGT, giving $p = 5/2$ and $s = 2.2$, which are similar to the values obtained in the case of other ferromagnets [187].

A recent study [188], close to the work presented here, on CGT reports on the manipulation of magnetic properties of CGT via eletrochemical intercalation of organic molecules (tetrabutyl ammonium, TBA^+), creating a (TBA)-CGT hybrid superlattice with metallic behaviour. This intercalated molecule is quite large compared with the alkali ions (i.e. Na-ions) and an increase of $\approx 10\,\AA$ in the vdWs gap is reported. In (TBA)-CGT, an enhancement of ferromagnetic T_c of up to 208 K is seen along with the switching of magnetic easy axis from the out-of-plane axis (in CGT) to the ab-plane. The (TBA)-CGT sample is probed by the magnetometry and magneto-transport techniques. The experimental data is supported by the theoretical calculations indicating that the increase of the T_c can be attributed to the change of magnetic exchange interaction from a weak superexchange interaction in CGT to a strong double-exchange interaction in (TBA)-CGT due to the high-level

of electron doping in the system [188]. The Na-ions intercalation process also leads to high-level of electron doping in the CGT system, even though the direct comparison reveals a smaller increase in the vdWs layer spacing in $Na_{0.3}$-CGT than organic intercalated CGT, a higher value of Curie temperature of 240 K is reported. This enhancement of T_c and the switching of the magnetic axis can also be attributed to a change in the exchange interaction mechanism in the intercalated samples.

6.4 Conclusion

In conclusion, the magnetic properties of pristine bulk single crystals of CGT were modified via intercalation of Na-ions into the vdWs gap producing $Na_{0.3}$-CGT samples. The initial XRD data showed a change in layer stacking and an increase in the inter-layer spacing of up to $\approx 0.8\,\AA$ in $Na_{0.3}$-CGT. The electrical two-point transport measurement also confirmed that the intercalation was successful as the system did not enter the insulating state in the low-temperature region.

The magnetic properties were probed by the magneto-transport and FMR spectroscopy techniques in two $Na_{0.3}$-CGT samples (I) and (II), respectively. The sample investigated by the magneto-transport measurement showed a magnetoresistance signal up to 195 K, whereas the sample used for the FMR experiment revealed a resonance signal up to the temperature of 240 K. In both the transport and magnetic resonance measurements, the magnetic anisotropy was found to be changed compared with unintercalated CGT sample, as the magnetic easy-axis was found to lie along the in-plane (ab-plane) orientation whereas it is along the out-of-plane (c-axis) orientation in the case of CGT. As reported elsewhere, the tuning of ferromagnetic transition temperature can be explained by the change in the exchange interaction from superexchange in CGT to double exchange in the intercalated samples.

Chapter 7

Summary and Outlook

This thesis has presented experimental studies of spin dynamics in three different magnetic systems: a chiral magnet (Cu_2OSeO_3), a bulk layered two-dimensional (2D) van der Waals (vdWs) crystal ($Cr_2Ge_2Te_6$), and sodium (Na) intercalated $Cr_2Ge_2Te_6$ sample.

The chiral magnetic system of Cu_2OSeO_3 has been known to host different magnetic spin textures below the Curie temperature due to the presence of anti-symmetric exchange interaction, the Dzyaloshinskii-Moriya interaction (DMI). The appearance of the non-collinear magnetic phases, i.e. helical, conical and skyrmion phases, depends on the temperature and the strength of external magnetic field in the phase diagram. Three different microwave resonators were used to study the interaction of cavity photons with the different magnetic phases in Cu_2OSeO_3. In the field-polarised phase, a strong-coupling regime between the photons and the uniform excitation of spins (magnons) was realised, with the cooperativity reaching 3600 for the hybridised state of the primary cavity mode and the magnon mode. In the non-collinear conical phase, dispersive coupling was observed between the fundamental helimagnon mode and the cavity modes, and this behaviour was used as a magnetic sensing probe for the phase transition in the system to map out the phase diagram. A Purcell-effect regime was detected with a normal-mode splitting feature between the cavity photons and high-order helimagnons in the non-collinear helical phase. The interaction of photons with the excitation modes of skyrmions was also shown. In the case of the counter-clockwise skyrmion mode, the first experimental

observation of an onset of anti-crossing feature was reported, where the coupling strength was found to be ≈ 3 times smaller than the loss-rate of skyrmions, hence the system did not enter the strong-coupling regime. In the parallel excitation configuration, the breathing mode resonance was seen and higher-order modes were distinguished.

In chapter 5, the ferromagnetic resonance (FMR) behaviour of bulk $Cr_2Ge_2Te_6$ (CGT) was investigated. A uniaxial perpendicular magnetic anisotropy was found with magnetic easy axis parallel to the c-axis (out-of-plane). The scaling of the normalised magnetocrystalline anisotropy constant and saturation magnetisation showed a deviation from the theoretically predicted Callen-Callen power law. The presence of spin orbit coupling from d-orbitals of Cr atoms and an off-site spin orbit coupling from p-orbitals of the ligand Te atoms can be a contributing factor to this contradicting behaviour of power law dependence of magnetic anisotropy to magnetisation. The obtained g-factor showed an anisotropic response. The determined g-factor values were greater than 2, again, indicating that the orbital magnetism played an important role in bulk CGT when considering magnetic interactions in this system. A small anisotropy in the orbital magnetic moment relative to the spin moment was found from the FMR experiments. The spin dynamics measurements were supported by the X-ray magnetic circular dichroism (XMCD) study, performed at the Diamond Light Source facility. The XMCD investigation experimentally confirmed that a sizeable orbital moment is present. The orbital moment also showed an anisotropy with external magnetic field along the c-axis and and the ab-plane as a function of temperature, complementing the results obtained through FMR spectroscopy. The presence of multidomain structures was qualitatively confirmed as domain-mode resonance phenomena was observed along the ab-plane (in-plane) orientation.

Finally, the magnetic properties of pristine bulk crystals of CGT are modified via intercalation of Na-ions into the vdWs gap producing $Na_{0.3}$-CGT samples. The initial XRD data showed an increase in the inter-layer spacing of up to $\approx 0.8\,\mathring{A}$ in $Na_{0.3}$-CGT. The electrical two-point transport measurement also confirmed that the

intercalation is successful as the system did not enter the insulating state in the low-temperature region. The magnetic properties were probed by the magneto-transport and FMR spectroscopy techniques in two $Na_{0.3}$-CGT samples (I) and (II), respectively. The sample investigated by the magneto-transport measurement showed a magnetoresistance signal up to 195 K, whereas the sample used for the FMR experiment revealed a resonance signal up to the temperature of 240 K. In both the transport and magnetic resonance measurements, the magnetic anisotropy was found to be changed compared with unintercalated CGT sample, as the magnetic easy-axis was found to lie along the in-plane (ab-plane) orientation whereas it was along the out-of-plane (c-axis) orientation in the case of CGT. As reported elsewhere, the tuning of ferromagnetic transition temperature can be explained by the change in the exchange interaction from superexchange in CGT to double exchange in the intercalated samples.

In response to the experimental work carried out in this thesis, further future efforts are required to realise the full potential of the three magnetic systems, mentioned above, in the field of spintronics. The light-matter interactions, in the context of strong-coupling between cavity photons and magnons, offer a strong avenue of combining the fields spintronics and quantum information. On this front, coherent coupling between photons and excitations of the topologically protected skyrmion particles has not been achieved yet. Improving the quality of the microwave resonators in the low-frequency regime [130] and in parallel reducing the damping of the skyrmion excitations can help with the experimental realisation of coherent coupling in this system, where maybe low-temperature skyrmionic states can be accessed for such an experiment [189].

In terms of the layered 2D magnetic systems, spin dynamics experiments can be designed as a function of the number of layers of CGT in order to probe magnetisation dynamics properties down to the monolayer limit. Specifically related to the work in this thesis, theoretical calculations of the XMCD spectra can give more insight on the experimentally observed orbital moment anisotropy. The intercalated CGT experiments are performed with the amount of intercalation, $x = 0.3$,

of Na atoms in Na_x-CGT samples. New Na_x-CGT samples with varied amount of intercalation, i.e. x, should be prepared and also intercalation of different species of alkali metal (e.g. lithium and potassium) ions should be carried out. This will give a better understanding of manipulation of magnetism in magnetic vdWs materials by means of chemical intercalation, and it can serve as a convenient and efficient approach to explore versatile magnetic and electronic properties in 2D vdWs magnets along with enhancing the Curie temperature towards room-temperature.

Appendix A

Sample Information

More information and images of the samples used in this thesis are shown in this appendix.

Cu_2OSeO_3

As mentioned in Chapter 4, the Cu_2OSeO_3 samples were provided by S. Seki (University of Tokyo). Single crystals of Cu_2OSeO_3 were grown by the chemical vapour transport method. In the growth process of the crystals, mixtures of high-purity SeO_2 (Alfa-Aesar, 99.999 %) and CuO (Alfa-Aesar, 99.995%) powder in molar ratio 1:2 were sealed in a quartz tubes with electronic grade HCl as the transport gas. The ampoules were heated at a rate of 50 °C/h to 600 °C by placing them horizontally into a tubular two-face furnace [190]. After a 6-week period, many

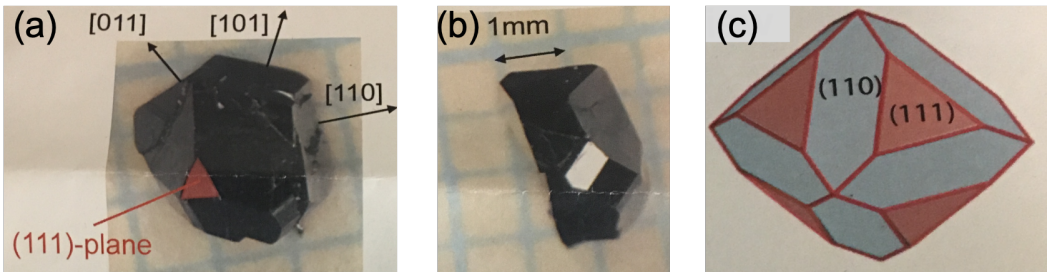

Figure A.1: Images of single crystal of Cu_2OSeO_3 as provided by the collaborator. (a) Top-view of sample highlighting the crystalline orientations and planes, where most of large surfaces are (110) planes, small triangular shaped surface is (111) plane and rounded (i.e. not flat) surface is attached to the quartz tube and does not correspond to natural facets. (b) Side-view of the sample. (c) Schematic highlighting crystal planes.

dark green, indeed almost black single crystals of Cu_2OSeO_3 were obtained, and the single crystal sample used in this thesis in Chapter 4 is shown in Fig. A.1 and A.2.

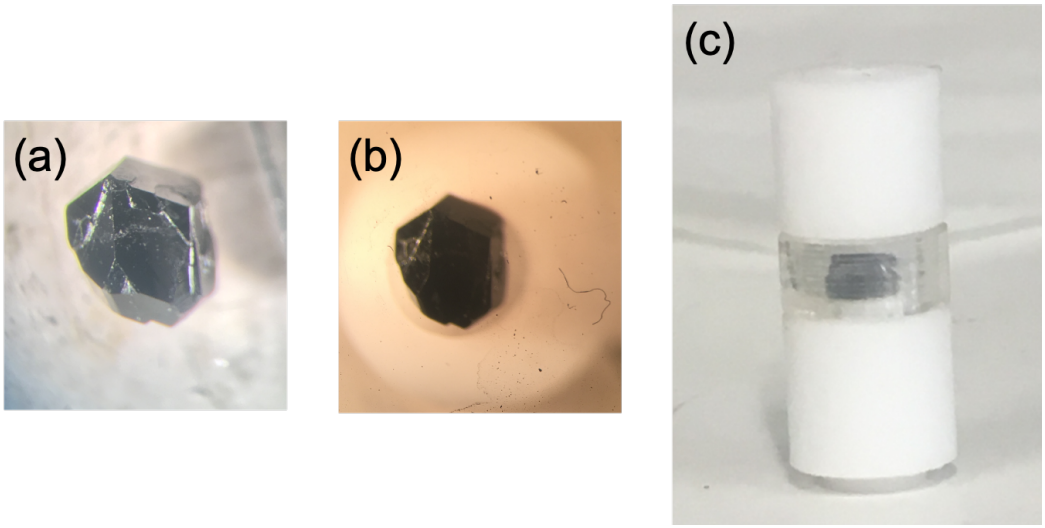

Figure A.2: Pictures of Cu_2OSeO_3 sample taken before the experiment. (a) Top-view of the sample before placing it in the cavity. (a) Top-view of the sample in the cavity. (c) Side-view of the sample placed inside the transparent cavity held by the PTFE spacers at top and bottom.

$Cr_2Ge_2Te_6$

Single crystal of layered van der Waals $Cr_2Ge_2Te_6$ were grown by I. Verzhbitskiy (collaborator at National University of Singapore). Single-crystalline flakes were synthesized by the direct vapour transport (or flux) method. At molar ratio of 20:27:153, high-purity Cr (99.9999% in chips), Ge (99.9999% in crystals) and Te (99.9999% in beads) were pre-mixed and it was sealed in the quartz ampule at high vacuum ($\approx 10^{-5}$ Torr). At a rate of 2 K/min, the ampule was loaded in the furnace and heated up to 1273 K, where it was left for 2 days. The furnace was set to slow cooling to reach 673 K, with a rate of 5 K/hour, for a low-defect crystal growth [147]. Afterwards, the furnace was switched off for natural cooling. The layered single-crystalline flakes of $Cr_2Ge_2Te_6$ were separated from the flux build up and stored in the inert atmosphere of the glovebox. The picture of the $Cr_2Ge_2Te_6$ sample used for magnetisation dynamics experiment is shown in Fig.

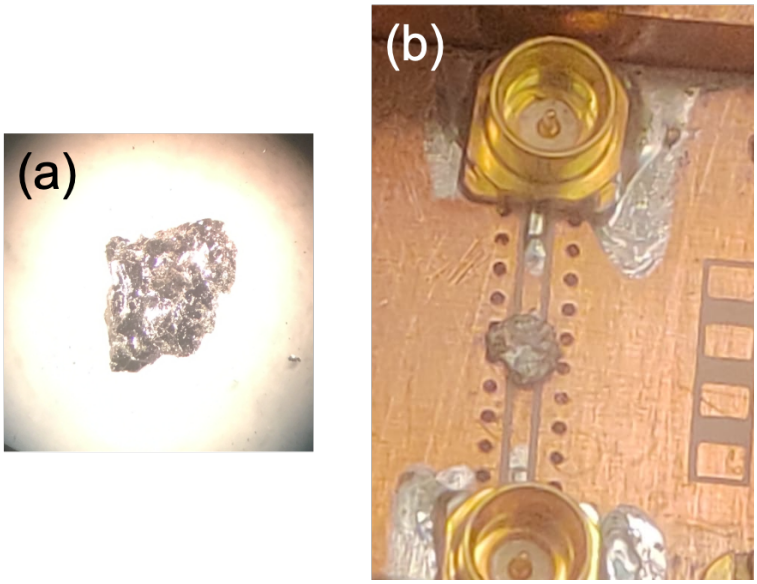

Figure A.3: (a) Picture of $Cr_2Ge_2Te_6$ sample. (b) The sample placed on a CPW for FMR experiments.

A.3. $Cr_2Ge_2Te_6$ samples were intercalated with Na atom as discussed earlier in Chapter 6, and this chemical process was carried out by M. K. Subhan (UCL). The picture of Na-$Cr_2Ge_2Te_6$ sample used for magnetotransport experiment can be seen in Fig. A.4.

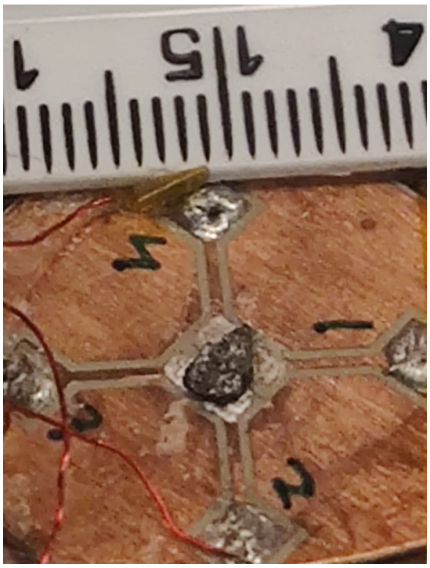

Figure A.4: Picture of Na intercalated $Cr_2Ge_2Te_6$ sample, where the sample is placed on a PCB with 4-contact pads for magnetotransport measurements.

Bibliography

[1] S. Wolf, D. Awschalom, R. Buhrman, J. Daughton, S. Von Molnar, M. Roukes, A. Y. Chtchelkanova, and D. Treger, "Spintronics: a spin-based electronics vision for the future," *Science*, vol. 294, no. 5546, pp. 1488–1495, 2001.

[2] S. Tehrani, J. Slaughter, E. Chen, M. Durlam, J. Shi, and M. DeHerren, "Progress and outlook for MRAM technology," *IEEE Transactions on Magnetics*, vol. 35, no. 5, pp. 2814–2819, 1999.

[3] Y. Huai, "Spin-transfer torque MRAM (STT-MRAM): Challenges and prospects," *AAPPS bulletin*, vol. 18, no. 6, pp. 33–40, 2008.

[4] M. D. Stiles and A. Zangwill, "Anatomy of spin-transfer torque," *Physical Review B*, vol. 66, no. 1, p. 014407, 2002.

[5] T. Kuschel and G. Reiss, "Spin orbitronics: Charges ride the spin wave," *Nature Nanotechnology*, vol. 10, no. 1, pp. 22–24, 2015.

[6] J. Hirsch, "Spin hall effect," *Physical Review Letters*, vol. 83, no. 9, p. 1834, 1999.

[7] K. Uchida, S. Takahashi, K. Harii, J. Ieda, W. Koshibae, K. Ando, S. Maekawa, and E. Saitoh, "Observation of the spin seebeck effect," *Nature*, vol. 455, no. 7214, pp. 778–781, 2008.

[8] K. Chau, M. Johnson, and A. Elezzabi, "Electron-spin-dependent terahertz light transport in spintronic-plasmonic media," *Physical Review Letters*, vol. 98, no. 13, p. 133901, 2007.

[9] G. Kurizki, P. Bertet, Y. Kubo, K. Mølmer, D. Petrosyan, P. Rabl, and J. Schmiedmayer, "Quantum technologies with hybrid systems," *Proceedings of the National Academy of Sciences*, vol. 112, no. 13, pp. 3866–3873, 2015.

[10] D. Lachance-Quirion, Y. Tabuchi, A. Gloppe, K. Usami, and Y. Nakamura, "Hybrid quantum systems based on magnonics," *Applied Physics Express*, vol. 12, no. 7, p. 070101, 2019.

[11] J. Bourhill, N. Kostylev, M. Goryachev, D. Creedon, and M. Tobar, "Ultra-high cooperativity interactions between magnons and resonant photons in a YIG sphere," *Physical Review B*, vol. 93, no. 14, p. 144420, 2016.

[12] A. Manchon, H. C. Koo, J. Nitta, S. Frolov, and R. Duine, "New perspectives for rashba spin-orbit coupling," *Nature Materials*, vol. 14, no. 9, pp. 871–882, 2015.

[13] N. Kanazawa, S. Seki, and Y. Tokura, "Non-centrosymmetric magnets hosting magnetic skyrmions," *Advanced Materials*, vol. 29, no. 25, p. 1603227, 2017.

[14] S. Seki, J.-H. Kim, D. Inosov, R. Georgii, B. Keimer, S. Ishiwata, and Y. Tokura, "Formation and rotation of skyrmion crystal in the chiral-lattice insulator Cu_2OSeO_3," *Physical Review B*, vol. 85, no. 22, p. 220406, 2012.

[15] M. Katsnelson and K. Novoselov, "Graphene: New bridge between condensed matter physics and quantum electrodynamics," *Solid State Communications*, vol. 143, no. 1-2, pp. 3–13, 2007.

[16] M. Gibertini, M. Koperski, A. Morpurgo, and K. Novoselov, "Magnetic 2D materials and heterostructures," *Nature Nanotechnology*, vol. 14, no. 5, pp. 408–419, 2019.

[17] C. Gong and X. Zhang, "Two-dimensional magnetic crystals and emergent heterostructure devices," *Science*, vol. 363, no. 6428, p. eaav4450, 2019.

[18] Y. Deng, Y. Yu, Y. Song, J. Zhang, N. Z. Wang, Z. Sun, Y. Yi, Y. Z. Wu, S. Wu, J. Zhu, *et al.*, "Gate-tunable room-temperature ferromagnetism in two-dimensional Fe_3GeTe_2," *Nature*, vol. 563, no. 7729, pp. 94–99, 2018.

[19] I. Verzhbitskiy, H. Kurebayashi, H. Cheng, J. Zhou, S. Khan, Y. P. Feng, and G. Eda, "Tailoring magnetic anisotropy in $Cr_2Ge_2Te_6$ by electrostatic gating," *arXiv preprint arXiv:2001.10217*, 2020.

[20] A. F. May, D. Ovchinnikov, Q. Zheng, R. Hermann, S. Calder, B. Huang, Z. Fei, Y. Liu, X. Xu, and M. A. McGuire, "Ferromagnetism near room temperature in the cleavable van der waals crystal Fe_5GeTe_2," *ACS Nano*, vol. 13, no. 4, pp. 4436–4442, 2019.

[21] J. Griffiths, "Anomalous high-frequency resistance of ferromagnetic metals," *Nature*, vol. 158, no. 4019, p. 670, 1946.

[22] E. Zavoisky, "Spin magnetic resonance in the decimeter-wave region," *J. Phys. USSR*, vol. 10, pp. 197–198, 1946.

[23] S. Vonsovskii, *Ferromagnetic Resonance*. Israel Program for Scientific Translations, 1964.

[24] S. Blundell, *Magnetism in Condensed Matter*. Oxford Master Series in Condensed Matter Physics, OUP Oxford, 2001.

[25] C. Kittel, P. McEuen, and P. McEuen, *Introduction to Solid State Physics*, vol. 8. Wiley New York, 1996.

[26] A. I. Rae, *Quantum physics: illusion or reality?* Cambridge University Press, 2004.

[27] E. d. T. De Lacheisserie, D. Gignoux, and M. Schlenker, *Magnetism*, vol. 1. Springer Science & Business Media, 2005.

[28] A. Aharoni *et al.*, *Introduction to the Theory of Ferromagnetism*, vol. 109. Clarendon Press, 2000.

[29] N. W. Ashcroft and N. D. Mermin, "Solid State Physics," *Saunders College, Philadelphia*, vol. 120, 1976.

[30] U. Larsen, "The RKKY indirect exchange interaction in metals in arbitrary continuous dimension," *Physics Letters A*, vol. 85, no. 8-9, pp. 471–473, 1981.

[31] M. Gilleo, "Superexchange interaction in ferrimagnetic garnets and spinels which contain randomly incomplete linkages," *Journal of Physics and Chemistry of Solids*, vol. 13, no. 1-2, pp. 33–39, 1960.

[32] K. Yosida and K. Yosida, *Theory of Magnetism: Edition en anglais*, vol. 122. Springer Science & Business Media, 1996.

[33] F. N. Rybakov, A. B. Borisov, S. Blügel, and N. S. Kiselev, "New type of stable particlelike states in chiral magnets," *Physical Review Letters*, vol. 115, no. 11, p. 117201, 2015.

[34] A. D. Kent and D. C. Worledge, "A new spin on magnetic memories," *Nature Nanotechnology*, vol. 10, no. 3, p. 187, 2015.

[35] J. D. Jackson, "Classical electrodynamics," 1999.

[36] J. Osborn, "Demagnetizing factors of the general ellipsoid," *Physical Review*, vol. 67, no. 11-12, p. 351, 1945.

[37] Cohen-Tannoudji, *Quantum Mechanics*. Wiley, 1978.

[38] A. Hubert and R. Schäfer, *Magnetic Domains: the analysis of magnetic microstructures*. Springer Science & Business Media, 2008.

[39] S. Chikazumi and C. D. Graham, *Physics of Ferromagnetism*, vol. 94. Oxford University Press on Demand, 2009.

[40] T. L. Gilbert, "A phenomenological theory of damping in ferromagnetic materials," *IEEE Transactions on Magnetics*, vol. 40, no. 6, pp. 3443–3449, 2004.

[41] L. Landau and E. Lifshitz, "On the theory of the dispersion of magnetic permeability in ferromagnetic bodies," *Phys. Z. Sowjetunion*, vol. 8, no. 153, pp. 101–114, 1935.

[42] H. Suhl, "Theory of the magnetic damping constant," *IEEE Transactions on Magnetics*, vol. 34, no. 4, pp. 1834–1838, 1998.

[43] V. Kamberskỳ, "On the landau–lifshitz relaxation in ferromagnetic metals," *Canadian Journal of Physics*, vol. 48, no. 24, pp. 2906–2911, 1970.

[44] M. Grobis, I. Rau, R. Potok, and D. Goldhaber-Gordon, "Handbook of Magnetism and Advanced Magnetic Materials," *by H. Kronmüller et al., Wiley*, p. 1, 2007.

[45] M. Farle, "Ferromagnetic resonance of ultrathin metallic layers," *Reports on Progress in Physics*, vol. 61, no. 7, p. 755, 1998.

[46] J. Smit and H. Beljers, "Ferromagnetic resonance absorption in $BaFe_{12}O_{19}$, a highly anisotropic crystal," *Philips Res. Rep*, vol. 10, no. 113, p. 31, 1955.

[47] H. Suhl, "Ferromagnetic resonance in nickel ferrite between one and two kilomegacycles," *Physical Review*, vol. 97, no. 2, p. 555, 1955.

[48] T. Gilbert, "A lagrangian formulation of the gyromagnetic equation of the magnetization field," *Physical Review*, vol. 100, p. 1243, 1955.

[49] S. V. Von Sovskii, *Ferromagnetic resonance: the phenomenon of resonant absorption of a high-frequency magnetic field in ferromagnetic substances*. Elsevier, 2016.

[50] I. Neudecker, *Magnetization dynamics of confined ferromagnetic systems*. PhD thesis, 2006.

[51] P. Hyde, "New methods for controlling coupling effects in cavity magnon-polariton systems," 2019.

[52] S. V. Kusminskiy, "Cavity optomagnonics," *arXiv preprint arXiv:1911.11104*, 2019.

[53] M. Harder and C.-M. Hu, "Cavity spintronics: an early review of recent progress in the study of magnon–photon level repulsion," in *Solid State Physics*, vol. 69, pp. 47–121, Elsevier, 2018.

[54] S. Kaur, "Study of on-chip cavity magnon polariton devices," 2016.

[55] L. Abdurakhimov, S. Khan, N. Panjwani, J. Breeze, M. Mochizuki, S. Seki, Y. Tokura, J. Morton, and H. Kurebayashi, "Magnon-photon coupling in the noncollinear magnetic insulator Cu_2OSeO_3," *Physical Review B*, vol. 99, no. 14, p. 140401, 2019.

[56] C. Gardiner, P. Zoller, and P. Zoller, *Quantum Noise: a handbook of Markovian and non-Markovian quantum stochastic methods with applications to quantum optics*. Springer Science & Business Media, 2004.

[57] D. Walls and G. J. Milburn, "Coherence properties of the electromagnetic field," in *Quantum Optics*, pp. 29–55, Springer, 2008.

[58] J. Als-Nielsen and D. McMorrow, *Elements of modern X-ray physics*. John Wiley & Sons, 2011.

[59] P. Fornasini, "Introduction to X-ray absorption spectroscopy," in *Synchrotron Radiation*, pp. 181–211, Springer, 2015.

[60] L. Mino, E. Borfecchia, J. Segura-Ruiz, C. Giannini, G. Martinez-Criado, and C. Lamberti, "Materials characterization by synchrotron X-ray microprobes and nanoprobes," *Reviews of Modern Physics*, vol. 90, no. 2, p. 025007, 2018.

[61] C. Chen, Y. Idzerda, H.-J. Lin, N. Smith, G. Meigs, E. Chaban, G. Ho, E. Pellegrin, and F. Sette, "Experimental confirmation of the X-ray magnetic circular dichroism sum rules for iron and cobalt," *Physical Review Letters*, vol. 75, no. 1, p. 152, 1995.

[62] B. Thole, G. Van der Laan, and G. Sawatzky, "Strong magnetic dichroism predicted in the M4,5 X-ray absorption spectra of magnetic rare-earth materials," *Physical Review Letters*, vol. 55, no. 19, p. 2086, 1985.

[63] J. L. Erskine and E. Stern, "Calculation of the M-23 magneto-optical absorption spectrum of ferromagnetic nickel," *Physical Review B*, vol. 12, no. 11, p. 5016, 1975.

[64] G. van der Laan, B. T. Thole, G. A. Sawatzky, J. B. Goedkoop, J. C. Fuggle, J.-M. Esteva, R. Karnatak, J. Remeika, and H. A. Dabkowska, "Experimental proof of magnetic X-ray dichroism," *Physical Review B*, vol. 34, no. 9, p. 6529, 1986.

[65] B. Thole, P. Carra, F. Sette, and G. van der Laan, "X-ray circular dichroism as a probe of orbital magnetisation," *Physical Review Letters*, vol. 68, no. 12, p. 1943, 1992.

[66] P. Carra, B. Thole, M. Altarelli, and X. Wang, "X-ray circular dichroism and local magnetic fields," *Physical Review Letters*, vol. 70, no. 5, p. 694, 1993.

[67] T. Skinner, *Electrical control of spin dynamics in spin-orbit coupled ferromagnets*. PhD thesis, University of Cambridge, 2015.

[68] W. Thomson, "Xix. on the electro-dynamic qualities of metals:effects of magnetization on the electric conductivity of nickel and of iron," *Proceedings of the Royal Society of London*, no. 8, pp. 546–550, 1857.

[69] T. McGuire and R. Potter, "Anisotropic magnetoresistance in ferromagnetic 3D alloys," *IEEE Transactions on Magnetics*, vol. 11, no. 4, pp. 1018–1038, 1975.

[70] J.-P. Jan, "Galvamomagnetic and thermomagnetic effects in metals," in *Solid State Physics*, vol. 5, pp. 1–96, Elsevier, 1957.

[71] J. Smit, "Magnetoresistance of ferromagnetic metals and alloys at low temperatures," *Physica*, vol. 17, no. 6, pp. 612–627, 1951.

[72] R. K. Mongia and P. Bhartia, "Dielectric resonator antennasa review and general design relations for resonant frequency and bandwidth," *International Journal of Microwave and Millimeter-Wave Computer-Aided Engineering*, vol. 4, no. 3, pp. 230–247, 1994.

[73] J. Breeze, "Modelling dielectric resonators," in *Temperature and Frequency Dependence of Complex Permittivity in Metal Oxide Dielectrics: Theory, Modelling and Measurement*, pp. 13–41, Springer, 2016.

[74] E. Ruff, P. Lunkenheimer, A. Loidl, H. Berger, and S. Krohns, "Magnetoelectric effects in the skyrmion host material Cu_2OSeO_3," *Scientific Reports*, vol. 5, p. 15025, 2015.

[75] K. Srinivasan and O. Painter, "Mode coupling and cavity–quantum-dot interactions in a fiber-coupled microdisk cavity," *Physical Review A*, vol. 75, no. 2, p. 023814, 2007.

[76] H. Kimble, E. Polzik, G. Rempe, and R. Thompson, "Structure and dynamics in cavity quantum electrodynamics," in *Quantum Electronics and Laser Science Conference*, p. QTuA2, Optical Society of America, 1992.

[77] A. Akdagli, *Behaviour of electromagnetic waves in different media and structures*. BoD–Books on Demand, 2011.

[78] D. Alesini, "Power coupling," *arXiv preprint arXiv:1112.3201*, 2011.

[79] N. Batra, S. Panja, S. De, A. Roy, S. Majhi, S. Yadav, and A. S. Gupta, "Design and construction of a helical resonator for delivering radio frequency to an ion trap," *MAPAN*, vol. 32, no. 3, pp. 193–198, 2017.

[80] D. M. Pozar, *Microwave Engineering, johnwiley & sons*. 1998.

[81] D. Pincini, *On the hierarchy of electronic and magnetic energy scales in novel 3d, 4d and 5d transition metal oxides probed by X-ray techniques*. PhD thesis, UCL (University College London), 2019.

[82] D. K. Schroder, *Semiconductor Material and Device Characterization*. John Wiley & Sons, 2015.

[83] J.-H. Lee, S. Park, C. Yang, H. K. Choi, M. R. Cho, S. U. Cho, and Y. D. Park, "Free-standing GaMnAs nanomachined sheets for van der pauw magnetotransport measurements," *Micromachines*, vol. 7, no. 12, p. 223, 2016.

[84] R. Hamdi, A. Tozri, M. Smari, E. Dhahri, and L. Bessais, "Resistivity, i–v characteristics and hall effect in $Dy_{0.5}[Sr_{(1-x)}Ca_x]_{0.5}MnO_3$ manganites," *Materials Research Bulletin*, vol. 95, pp. 525–531, 2017.

[85] H. Huebl, C. W. Zollitsch, J. Lotze, F. Hocke, M. Greifenstein, A. Marx, R. Gross, and S. T. Goennenwein, "High cooperativity in coupled microwave resonator ferrimagnetic insulator hybrids," *Physical Review Letters*, vol. 111, no. 12, p. 127003, 2013.

[86] Y. Tabuchi, S. Ishino, T. Ishikawa, R. Yamazaki, K. Usami, and Y. Nakamura, "Hybridizing ferromagnetic magnons and microwave photons in the quantum limit," *Physical Review Letters*, vol. 113, no. 8, p. 083603, 2014.

[87] X. Zhang, C.-L. Zou, L. Jiang, and H. X. Tang, "Strongly coupled magnons and cavity microwave photons," *Physical Review Letters*, vol. 113, no. 15, p. 156401, 2014.

[88] L. V. Abdurakhimov, Y. M. Bunkov, and D. Konstantinov, "Normal-mode splitting in the coupled system of hybridized nuclear magnons and microwave photons," *Physical Review Letters*, vol. 114, no. 22, p. 226402, 2015.

[89] I. Chiorescu, N. Groll, S. Bertaina, T. Mori, and S. Miyashita, "Magnetic strong coupling in a spin-photon system and transition to classical regime," *Physical Review B*, vol. 82, no. 2, p. 024413, 2010.

[90] D. Schuster, A. Sears, E. Ginossar, L. DiCarlo, L. Frunzio, J. Morton, H. Wu, G. Briggs, B. Buckley, D. Awschalom, *et al.*, "High-cooperativity coupling of

electron-spin ensembles to superconducting cavities," *Physical Review Letters*, vol. 105, no. 14, p. 140501, 2010.

[91] V. Muravev, I. Andreev, I. Kukushkin, S. Schmult, and W. Dietsche, "Observation of hybrid plasmon-photon modes in microwave transmission of coplanar microresonators," *Physical Review B*, vol. 83, no. 7, p. 075309, 2011.

[92] G. Scalari, C. Maissen, D. Turčinková, D. Hagenmüller, S. De Liberato, C. Ciuti, C. Reichl, D. Schuh, W. Wegscheider, M. Beck, *et al.*, "Ultrastrong coupling of the cyclotron transition of a 2D electron gas to a THz metamaterial," *Science*, vol. 335, no. 6074, pp. 1323–1326, 2012.

[93] G. Agarwal, "Vacuum-field rabi splittings in microwave absorption by rydberg atoms in a cavity," *Physical Review Letters*, vol. 53, no. 18, p. 1732, 1984.

[94] A. Imamoğlu, "Cavity QED based on collective magnetic dipole coupling: spin ensembles as hybrid two-level systems," *Physical Review Letters*, vol. 102, no. 8, p. 083602, 2009.

[95] B. M. Garraway, "The dicke model in quantum optics: Dicke model revisited," *Philosophical Transactions of the Royal Society A: Mathematical, Physical and Engineering Sciences*, vol. 369, no. 1939, pp. 1137–1155, 2011.

[96] B. Yao, Y. Gui, Y. Xiao, H. Guo, X. Chen, W. Lu, C. Chien, and C.-M. Hu, "Theory and experiment on cavity magnon-polariton in the one-dimensional configuration," *Physical Review B*, vol. 92, no. 18, p. 184407, 2015.

[97] R. Schoelkopf and S. Girvin, "Wiring up quantum systems," *Nature*, vol. 451, no. 7179, p. 664, 2008.

[98] G. Kurizki, P. Bertet, Y. Kubo, K. Mølmer, D. Petrosyan, P. Rabl, and J. Schmiedmayer, "Quantum technologies with hybrid systems," *Proceedings of the National Academy of Sciences*, vol. 112, no. 13, pp. 3866–3873, 2015.

[99] S. Blum, C. O'Brien, N. Lauk, P. Bushev, M. Fleischhauer, and G. Morigi, "Interfacing microwave qubits and optical photons via spin ensembles," *Physical Review A*, vol. 91, no. 3, p. 033834, 2015.

[100] Y. Tabuchi, S. Ishino, A. Noguchi, T. Ishikawa, R. Yamazaki, K. Usami, and Y. Nakamura, "Coherent coupling between a ferromagnetic magnon and a superconducting qubit," *Science*, vol. 349, no. 6246, pp. 405–408, 2015.

[101] X. Zhang, C.-L. Zou, N. Zhu, F. Marquardt, L. Jiang, and H. X. Tang, "Magnon dark modes and gradient memory," *Nature Communications*, vol. 6, p. 8914, 2015.

[102] N. J. Lambert, J. Haigh, S. Langenfeld, A. Doherty, and A. Ferguson, "Cavity-mediated coherent coupling of magnetic moments," *Physical Review A*, vol. 93, no. 2, p. 021803, 2016.

[103] L. Bai, M. Harder, Y. Chen, X. Fan, J. Xiao, and C.-M. Hu, "Spin pumping in electrodynamically coupled magnon-photon systems," *Physical Review Letters*, vol. 114, no. 22, p. 227201, 2015.

[104] A. Osada, A. Gloppe, R. Hisatomi, A. Noguchi, R. Yamazaki, M. Nomura, Y. Nakamura, and K. Usami, "Brillouin light scattering by magnetic quasivortices in cavity optomagnonics," *Physical Review Letters*, vol. 120, no. 13, p. 133602, 2018.

[105] M. Mergenthaler, J. Liu, J. J. Le Roy, N. Ares, A. L. Thompson, L. Bogani, F. Luis, S. J. Blundell, T. Lancaster, A. Ardavan, *et al.*, "Strong coupling of microwave photons to antiferromagnetic fluctuations in an organic magnet," *Physical Review Letters*, vol. 119, no. 14, p. 147701, 2017.

[106] H. T. Nembach, J. M. Shaw, M. Weiler, E. Jué, and T. J. Silva, "Linear relation between heisenberg exchange and interfacial dzyaloshinskii–moriya interaction in metal films," *Nature Physics*, vol. 11, no. 10, p. 825, 2015.

[107] J.-H. Yang, Z.-L. Li, X. Lu, M.-H. Whangbo, S.-H. Wei, X. Gong, and H. Xiang, "Strong dzyaloshinskii-moriya interaction and origin of ferroelectricity in Cu_2OSeO_3," *Physical Review Letters*, vol. 109, no. 10, p. 107203, 2012.

[108] A. Larrañaga, J. L. Mesa, L. Lezama, J. L. Pizarro, M. I. Arriortua, and T. Rojo, "Supercritical hydrothermal synthesis of Cu_2OSeO_3: Structural characterization, thermal, spectroscopic and magnetic studies," *Materials Research Bulletin*, vol. 44, no. 1, pp. 1–5, 2009.

[109] O. Janson, I. Rousochatzakis, A. A. Tsirlin, M. Belesi, A. A. Leonov, U. K. Rößler, J. Van Den Brink, and H. Rosner, "The quantum nature of skyrmions and half-skyrmions in Cu_2OSeO_3," *Nature Communications*, vol. 5, p. 5376, 2014.

[110] R. Versteeg, J. Zhu, C. Boguschewski, F. Sekiguchi, A. Sahasrabudhe, K. Budzinauskas, P. Padmanabhan, P. Becker, D. Khomskii, and P. van Loosdrecht, "Coupled dynamics of long-range and cluster-internal spin order in the cluster mott insulator Cu_2OSeO_3," *Physical Review B*, vol. 100, no. 6, p. 064401, 2019.

[111] S. Seki, S. Ishiwata, and Y. Tokura, "Magnetoelectric nature of skyrmions in a chiral magnetic insulator Cu_2OSeO_3," *Physical Review B*, vol. 86, no. 6, p. 060403, 2012.

[112] T. Schwarze, J. Waizner, M. Garst, A. Bauer, I. Stasinopoulos, H. Berger, C. Pfleiderer, and D. Grundler, "Universal helimagnon and skyrmion excitations in metallic, semiconducting and insulating chiral magnets," *Nature Materials*, vol. 14, no. 5, p. 478, 2015.

[113] S. Seki, X. Yu, S. Ishiwata, and Y. Tokura, "Observation of skyrmions in a multiferroic material," *Science*, vol. 336, no. 6078, pp. 198–201, 2012.

[114] L. Bai, M. Harder, P. Hyde, Z. Zhang, C.-M. Hu, Y. Chen, and J. Q. Xiao, "Cavity mediated manipulation of distant spin currents using a cavity-

magnon-polariton," *Physical Review Letters*, vol. 118, no. 21, p. 217201, 2017.

[115] P. Lodahl, A. F. Van Driel, I. S. Nikolaev, A. Irman, K. Overgaag, D. Vanmaekelbergh, and W. L. Vos, "Controlling the dynamics of spontaneous emission from quantum dots by photonic crystals," *Nature*, vol. 430, no. 7000, p. 654, 2004.

[116] G. Morigi, J. Eschner, and C. H. Keitel, "Ground state laser cooling using electromagnetically induced transparency," *Physical Review Letters*, vol. 85, no. 21, p. 4458, 2000.

[117] M. Goryachev, W. G. Farr, D. L. Creedon, Y. Fan, M. Kostylev, and M. E. Tobar, "High-cooperativity cavity qed with magnons at microwave frequencies," *Physical Review Applied*, vol. 2, no. 5, p. 054002, 2014.

[118] G. Flower, M. Goryachev, J. Bourhill, and M. E. Tobar, "Experimental implementations of cavity-magnon systems: from ultra strong coupling to applications in precision measurement," *New Journal of Physics*, vol. 21, no. 9, p. 095004, 2019.

[119] I. Boventer, M. Pfirrmann, J. Krause, Y. Schön, M. Kläui, and M. Weides, "Complex temperature dependence of coupling and dissipation of cavity magnon polaritons from millikelvin to room temperature," *Physical Review B*, vol. 97, no. 18, p. 184420, 2018.

[120] H. Maier-Flaig, M. Harder, S. Klingler, Z. Qiu, E. Saitoh, M. Weiler, S. Geprägs, R. Gross, S. Goennenwein, and H. Huebl, "Tunable magnon-photon coupling in a compensating ferrimagnetfrom weak to strong coupling," *Applied Physics Letters*, vol. 110, no. 13, p. 132401, 2017.

[121] F. Qian, L. J. Bannenberg, H. Wilhelm, G. Chaboussant, L. M. Debeer-Schmitt, M. P. Schmidt, A. Aqeel, T. T. Palstra, E. Brück, A. J. Lefering, *et al.*, "New magnetic phase of the chiral skyrmion material Cu_2OSeO_3," *Science Advances*, vol. 4, no. 9, p. eaat7323, 2018.

[122] M. Weiler, A. Aqeel, M. Mostovoy, A. Leonov, S. Geprägs, R. Gross, H. Huebl, T. T. Palstra, and S. T. Goennenwein, "Helimagnon resonances in an intrinsic chiral magnonic crystal," *Physical Review Letters*, vol. 119, no. 23, p. 237204, 2017.

[123] T. Skyrme, "A nonlinear field theory," *Proc. Roy. Soc. Lond.*, vol. 260, pp. 127–138, 1961.

[124] T. H. R. Skyrme, "A unified field theory of mesons and baryons," *Nuclear Physics*, vol. 31, pp. 556–569, 1962.

[125] A. Bogdanov and A. Hubert, "Thermodynamically stable magnetic vortex states in magnetic crystals," *Journal of Magnetism and Magnetic Materials*, vol. 138, no. 3, pp. 255–269, 1994.

[126] X. Yu, Y. Onose, N. Kanazawa, J. Park, J. Han, Y. Matsui, N. Nagaosa, and Y. Tokura, "Real-space observation of a two-dimensional skyrmion crystal," *Nature*, vol. 465, no. 7300, pp. 901–904, 2010.

[127] Y. Okamura, F. Kagawa, M. Mochizuki, M. Kubota, S. Seki, S. Ishiwata, M. Kawasaki, Y. Onose, and Y. Tokura, "Microwave magnetoelectric effect via skyrmion resonance modes in a helimagnetic multiferroic," *Nature Communications*, vol. 4, p. 2391, 2013.

[128] M. Mochizuki, "Spin-wave modes and their intense excitation effects in skyrmion crystals," *Physical Review Letters*, vol. 108, no. 1, p. 017601, 2012.

[129] Y. Onose, Y. Okamura, S. Seki, S. Ishiwata, and Y. Tokura, "Observation of magnetic excitations of skyrmion crystal in a helimagnetic insulator Cu_2OSeO_3," *Physical Review Letters*, vol. 109, no. 3, p. 037603, 2012.

[130] M. J. Martínez-Pérez and D. Zueco, "Quantum electrodynamics with magnetic textures," *New Journal of Physics*, vol. 21, no. 11, p. 115002, 2019.

[131] B. Liu, Y. Zou, L. Zhang, S. Zhou, Z. Wang, W. Wang, Z. Qu, and Y. Zhang, "Critical behavior of the quasi-two-dimensional semiconducting ferromagnet $CrSiTe_3$," *Scientific Reports*, vol. 6, no. 1, pp. 1–8, 2016.

[132] Z. Wang, I. Gutiérrez-Lezama, N. Ubrig, M. Kroner, M. Gibertini, T. Taniguchi, K. Watanabe, A. Imamoğlu, E. Giannini, and A. F. Morpurgo, "Very large tunneling magnetoresistance in layered magnetic semiconductor CrI_3," *Nature Communications*, vol. 9, no. 1, pp. 1–8, 2018.

[133] N. Richter, D. Weber, F. Martin, N. Singh, U. Schwingenschlögl, B. V. Lotsch, and M. Kläui, "Temperature-dependent magnetic anisotropy in the layered magnetic semiconductors CrI_3 and $CrBr_3$," *Physical Review Materials*, vol. 2, no. 2, p. 024004, 2018.

[134] C. Gong, L. Li, Z. Li, H. Ji, A. Stern, Y. Xia, T. Cao, W. Bao, C. Wang, Y. Wang, *et al.*, "Discovery of intrinsic ferromagnetism in two-dimensional van der waals crystals," *Nature*, vol. 546, no. 7657, pp. 265–269, 2017.

[135] C. Cardoso, D. Soriano, N. García-Martínez, and J. Fernández-Rossier, "Van der waals spin valves," *Physical Review Letters*, vol. 121, no. 6, p. 067701, 2018.

[136] Y. Fang, S. Wu, Z.-Z. Zhu, and G.-Y. Guo, "Large magneto-optical effects and magnetic anisotropy energy in two-dimensional $Cr_2Ge_2Te_6$," *Physical Review B*, vol. 98, no. 12, p. 125416, 2018.

[137] N. D. Mermin and H. Wagner, "Absence of ferromagnetism or antiferromagnetism in one-or two-dimensional isotropic heisenberg models," *Physical Review Letters*, vol. 17, no. 22, p. 1133, 1966.

[138] Z. Wang, T. Zhang, M. Ding, B. Dong, Y. Li, M. Chen, X. Li, J. Huang, H. Wang, X. Zhao, *et al.*, "Electric-field control of magnetism in a few-layered van der waals ferromagnetic semiconductor," *Nature Nanotechnology*, vol. 13, no. 7, pp. 554–559, 2018.

[139] Y. Liu, C. Petrovic, *et al.*, "Anisotropic magnetic entropy change in $Cr_2X_2Te_6$ (X= Si and Ge)," *Physical Review Materials*, vol. 3, no. 1, p. 014001, 2019.

[140] Y. Liu, C. Petrovic, *et al.*, "Critical behavior of quasi-two-dimensional semiconducting ferromagnet $Cr_2Ge_2Te_6$," *Physical Review B*, vol. 96, no. 5, p. 054406, 2017.

[141] W. Liu, Y. Dai, Y.-E. Yang, J. Fan, L. Pi, L. Zhang, and Y. Zhang, "Critical behavior of the single-crystalline van der waals bonded ferromagnet $Cr_2Ge_2Te_6$," *Physical Review B*, vol. 98, no. 21, p. 214420, 2018.

[142] L. Alegria, H. Ji, N. Yao, J. Clarke, R. J. Cava, and J. R. Petta, "Large anomalous hall effect in ferromagnetic insulator-topological insulator heterostructures," *Applied Physics Letters*, vol. 105, no. 5, p. 053512, 2014.

[143] X. Zhang, Y. Zhao, Q. Song, S. Jia, J. Shi, and W. Han, "Magnetic anisotropy of the single-crystalline ferromagnetic insulator $Cr_2Ge_2Te_6$," *Japanese Journal of Applied Physics*, vol. 55, no. 3, p. 033001, 2016.

[144] A. Anisimov, M. Farle, P. Poulopoulos, W. Platow, K. Baberschke, P. Isberg, R. Wäppling, A. Niklasson, and O. Eriksson, "Orbital magnetism and magnetic anisotropy probed with ferromagnetic resonance," *Physical Review Letters*, vol. 82, no. 11, p. 2390, 1999.

[145] M. Farle, "Ferromagnetic resonance of ultrathin metallic layers," *Reports on progress in physics*, vol. 61, no. 7, p. 755, 1998.

[146] Z. Lin, M. Lohmann, Z. A. Ali, C. Tang, J. Li, W. Xing, J. Zhong, S. Jia, W. Han, S. Coh, *et al.*, "Pressure-induced spin reorientation transition in layered ferromagnetic insulator $Cr_2Ge_2Te_6$," *Physical Review Materials*, vol. 2, no. 5, p. 051004, 2018.

[147] S. Khan, C. Zollitsch, D. Arroo, H. Cheng, I. Verzhbitskiy, A. Sud, Y. Feng, G. Eda, and H. Kurebayashi, "Spin dynamics study in layered van der waals

single-crystal $Cr_2Ge_2Te_6$," *Physical Review B*, vol. 100, no. 13, p. 134437, 2019.

[148] Z. Celinski, K. Urquhart, and B. Heinrich, "Using ferromagnetic resonance to measure the magnetic moments of ultrathin films," *Journal of Magnetism and Magnetic Materials*, vol. 166, no. 1-2, pp. 6–26, 1997.

[149] F. Yang, C. Chien, E. Ferrari, X. Li, G. Xiao, and A. Gupta, "Uniaxial anisotropy and switching behavior in epitaxial CrO_2 films," *Applied Physics Letters*, vol. 77, no. 2, pp. 286–288, 2000.

[150] N. León-Brito, E. D. Bauer, F. Ronning, J. D. Thompson, and R. Movshovich, "Magnetic microstructure and magnetic properties of uniaxial itinerant ferromagnet Fe_3GeTe_2," *Journal of Applied Physics*, vol. 120, no. 8, p. 083903, 2016.

[151] J. Dillon Jr and C. Olson, "Magnetization, resonance, and optical properties of the ferromagnet CrI_3," *Journal of Applied Physics*, vol. 36, no. 3, pp. 1259–1260, 1965.

[152] J. H. van Vleck, "On the anisotropy of cubic ferromagnetic crystals," *Physical Review*, vol. 52, no. 11, p. 1178, 1937.

[153] C. Zener, "Classical theory of the temperature dependence of magnetic anisotropy energy," *Physical Review*, vol. 96, no. 5, p. 1335, 1954.

[154] H. B. Callen and E. Callen, "The present status of the temperature dependence of magnetocrystalline anisotropy, and the l(l+ 1)/2 power law," *Journal of Physics and Chemistry of Solids*, vol. 27, no. 8, pp. 1271–1285, 1966.

[155] K. Zakeri, T. Kebe, J. Lindner, and M. Farle, "Power-law behavior of the temperature dependence of magnetic anisotropy of uncapped ultrathin Fe films on GaAs (001)," *Physical Review B*, vol. 73, no. 5, p. 052405, 2006.

[156] R. Skomski, A. Kashyap, and D. J. Sellmyer, "Finite-temperature anisotropy of PtCo magnets," *IEEE Transactions on Magnetics*, vol. 39, no. 5, pp. 2917–2919, 2003.

[157] O. N. Mryasov, U. Nowak, K. Y. Guslienko, and R. W. Chantrell, "Temperature-dependent magnetic properties of FePt: Effective spin hamiltonian model," *EPL (Europhysics Letters)*, vol. 69, no. 5, p. 805, 2005.

[158] A. Truong, A. Watanabe, T. Sekiguchi, P. Mortemousque, T. Sato, K. Ando, and K. M. Itoh, "Evidence of a perpendicular magnetocrystalline anisotropy in a Mn_5Ge_3 epitaxial thin film revealed by ferromagnetic resonance," *Physical Review B*, vol. 90, no. 22, p. 224415, 2014.

[159] J. Wang, F. Zhao, W. Wu, and G.-M. Zhao, "Unusual temperature dependence of the magnetic anisotropy constant in barium ferrite $BaFe_{12}O_{19}$," *Journal of Applied Physics*, vol. 110, no. 9, p. 096107, 2011.

[160] B. K. Chatterjee, C. Ghosh, and K. Chattopadhyay, "Temperature dependence of magnetization and anisotropy in uniaxial $NiFe_2O_4$ nanomagnets: Deviation from the callen-callen power law," *Journal of Applied Physics*, vol. 116, no. 15, p. 153904, 2014.

[161] C. Xu, J. Feng, H. Xiang, and L. Bellaiche, "Interplay between kitaev interaction and single ion anisotropy in ferromagnetic CrI_3 and $CrGeTe_3$ monolayers," *npj Computational Materials*, vol. 4, no. 1, pp. 1–6, 2018.

[162] D.-H. Kim, K. Kim, K.-T. Ko, J. Seo, J. S. Kim, T.-H. Jang, Y. Kim, J.-Y. Kim, S.-W. Cheong, and J.-H. Park, "Giant magnetic anisotropy induced by ligand L-S coupling in layered Cr compounds," *Physical Review Letters*, vol. 122, no. 20, p. 207201, 2019.

[163] C. Kittel, "On the gyromagnetic ratio and spectroscopic splitting factor of ferromagnetic substances," *Physical Review*, vol. 76, no. 6, p. 743, 1949.

[164] J. M. Shaw, H. T. Nembach, T. J. Silva, and C. T. Boone, "Precise determination of the spectroscopic g-factor by use of broadband ferromagnetic resonance spectroscopy," *Journal of Applied Physics*, vol. 114, no. 24, p. 243906, 2013.

[165] K. Baberschke, "Anisotropy in magnetism," in *Band-Ferromagnetism*, pp. 27–45, Springer, 2001.

[166] M. Altarelli, "Orbital-magnetization sum rule for X-ray circular dichroism: A simple proof," *Physical Review B*, vol. 47, no. 2, p. 597, 1993.

[167] A. Frisk, L. B. Duffy, S. Zhang, G. van der Laan, and T. Hesjedal, "Magnetic x-ray spectroscopy of two-dimensional CrI_3 layers," *Materials Letters*, vol. 232, pp. 5–7, 2018.

[168] B. Lührmann, H. Dötsch, and S. Sure, "High-frequency excitations of stripe-domain lattices in magnetic garnet films," *Applied Physics A*, vol. 57, no. 6, pp. 553–559, 1993.

[169] M. Sigal, "Ferromagnetic resonance in $BaFe_{12}O_{19}$ with cylindrical domain structure at arbitrary magnetization," *physica status solidi (a)*, vol. 42, no. 2, pp. 775–784, 1977.

[170] K. Zakeri, T. Kebe, J. Lindner, and M. Farle, "Magnetic anisotropy of Fe/GaAs (001) ultrathin films investigated by in-situ ferromagnetic resonance," *Journal of Magnetism and Magnetic Materials*, vol. 299, no. 1, pp. L1–L10, 2006.

[171] M. A. McGuire, G. Clark, K. Santosh, W. M. Chance, G. E. Jellison Jr, V. R. Cooper, X. Xu, and B. C. Sales, "Magnetic behavior and spin-lattice coupling in cleavable van der waals layered $CrCl_3$ crystals," *Physical Review Materials*, vol. 1, no. 1, p. 014001, 2017.

[172] M. A. McGuire, H. Dixit, V. R. Cooper, and B. C. Sales, "Coupling of crystal structure and magnetism in the layered, ferromagnetic insulator CrI_3," *Chemistry of Materials*, vol. 27, no. 2, pp. 612–620, 2015.

[173] T. Guo, Z. Ma, G. Lin, X. Luo, Y. Hou, Y. Sun, Z. Sheng, and Q. Lu, "Multiple structure and symmetry types in narrow temperature and magnetic field ranges in two-dimensional $Cr_2Ge_2Te_6$ crystal," *arXiv preprint arXiv:1803.06113*, 2018.

[174] H. Terashita, J. Cezar, F. Ardito, L. Bufaical, and E. Granado, "Investigation of element-specific and bulk magnetism, electronic and crystal structures of $La_{0.70}Ca_{0.30}Mn_{1-x}Cr_xO_3$," *arXiv preprint arXiv:1105.1392*, 2011.

[175] M. D. Watson, I. Marković, F. Mazzola, A. Rajan, E. A. Morales, D. M. Burn, T. Hesjedal, G. van der Laan, S. Mukherjee, T. K. Kim, *et al.*, "Direct observation of the energy gain underpinning ferromagnetic superexchange in the electronic structure of $CrGeTe_3$," *arXiv preprint arXiv:1912.11314*, 2019.

[176] M. Ye, W. Li, S. Zhu, Y. Takeda, Y. Saitoh, J. Wang, H. Pan, M. Nurmamat, K. Sumida, F. Ji, *et al.*, "Carrier-mediated ferromagnetism in the magnetic topological insulator Cr-doped$(Sb, Bi)_2Te_3$," *Nature Communications*, vol. 6, no. 1, pp. 1–7, 2015.

[177] P. Poulopoulos, A. Scherz, F. Wilhelm, H. Wende, and K. Baberschke, "Direct probe of induced magnetic moments at interfaces via X-ray magnetic circular dichroism," *Physica Status Solidi (a)*, vol. 189, no. 2, pp. 293–300, 2002.

[178] C. Piamonteze, P. Miedema, and F. M. De Groot, "Accuracy of the spin sum rule in XMCD for the transition-metal l edges from manganese to copper," *Physical Review B*, vol. 80, no. 18, p. 184410, 2009.

[179] P. L. Cullen, K. M. Cox, M. K. B. Subhan, L. Picco, O. D. Payton, D. J. Buckley, T. S. Miller, S. A. Hodge, N. T. Skipper, V. Tileli, *et al.*, "Ionic solutions of two-dimensional materials," *Nature Chemistry*, vol. 9, no. 3, p. 244, 2017.

[180] T. Eknapakul, P. King, M. Asakawa, P. Buaphet, R.-H. He, S.-K. Mo, H. Takagi, K. Shen, F. Baumberger, T. Sasagawa, *et al.*, "Electronic structure of a quasi-freestanding MoS_2 monolayer," *Nano Letters*, vol. 14, no. 3, pp. 1312–1316, 2014.

[181] H. Ji, R. Stokes, L. Alegria, E. Blomberg, M. Tanatar, A. Reijnders, L. M. Schoop, T. Liang, R. Prozorov, K. Burch, *et al.*, "A ferromagnetic insulating substrate for the epitaxial growth of topological insulators," *Journal of Applied Physics*, vol. 114, no. 11, p. 114907, 2013.

[182] Y. S. Hor, A. J. Williams, J. G. Checkelsky, P. Roushan, J. Seo, Q. Xu, H. W. Zandbergen, A. Yazdani, N. P. Ong, and R. J. Cava, "Superconductivity in $Cu_xBi_2Se_3$ and its implications for pairing in the undoped topological insulator," *Physical Review Letters*, vol. 104, no. 5, p. 057001, 2010.

[183] W. Liu, Y. Wang, Y. Han, W. Tong, J. Fan, L. Pi, N. Hao, L. Zhang, and Y. Zhang, "Anisotropic magnetoresistance behaviors in the layered ferromagnetic $Cr_2Ge_2Te_6$," *Journal of Physics D: Applied Physics*, vol. 53, no. 2, p. 025101, 2019.

[184] C. Song, W. Xiao, L. Li, Y. Lu, P. Jiang, C. Li, A. Chen, and Z. Zhong, "Tunable band gap and enhanced ferromagnetism by surface adsorption in monolayer $Cr_2Ge_2Te_6$," *Physical Review B*, vol. 99, no. 21, p. 214435, 2019.

[185] Z. Wang, T. Ye, and R. Mani, "Superconducting-contact-induced resistance-anomalies in the 3D topological insulator Bi_2Te_3," *Applied Physics Letters*, vol. 107, no. 17, p. 172103, 2015.

[186] S. S. Kalarickal, P. Krivosik, M. Wu, C. E. Patton, M. L. Schneider, P. Kabos, T. J. Silva, and J. P. Nibarger, "Ferromagnetic resonance linewidth in metallic thin films: Comparison of measurement methods," *Journal of Applied Physics*, vol. 99, no. 9, p. 093909, 2006.

[187] M. Kuzmin, "Shape of temperature dependence of spontaneous magnetization of ferromagnets: quantitative analysis," *Physical Review Letters*, vol. 94, no. 10, p. 107204, 2005.

[188] N. Wang, H. Tang, M. Shi, H. Zhang, W. Zhuo, D. Liu, F. Meng, L. Ma, J. Ying, L. Zou, *et al.*, "Transition from ferromagnetic semiconductor to ferromagnetic metal with enhanced curie temperature in $Cr_2Ge_2Te_6$ via organic ion intercalation," *Journal of the American Chemical Society*, vol. 141, no. 43, pp. 17166–17173, 2019.

[189] L. J. Bannenberg, H. Wilhelm, R. Cubitt, A. Labh, M. P. Schmidt, E. Lelièvre-Berna, C. Pappas, M. Mostovoy, and A. O. Leonov, "Multiple low-temperature skyrmionic states in a bulk chiral magnet," *npj Quantum Materials*, vol. 4, no. 1, pp. 1–8, 2019.

[190] K. Miller, X. Xu, H. Berger, E. Knowles, D. Arenas, M. W. Meisel, and D. Tanner, "Magnetodielectric coupling of infrared phonons in single-crystal Cu_2OSeO_3," *Physical Review B*, vol. 82, no. 14, p. 144107, 2010.